5-2018

Advanced Manufacturing of Lightweight Porous Carbide Shapes Using Renewable Resources

Monsur Islam
Clemson University, monsurislam79@gmail.com

Recommended Citation

Islam, Monsur, "Advanced Manufacturing of Lightweight Porous Carbide Shapes Using Renewable Resources" (2018). *All Dissertations*. 2138.
https://tigerprints.clemson.edu/all_dissertations/2138

ADVANCED MANUFACTURING OF LIGHTWEIGHT POROUS CARBIDE SHAPES USING RENEWABLE RESOURCES

A Dissertation
Presented to
the Graduate School of
Clemson University

In Partial Fulfilment
of the Requirements for the Degree
Doctor of Philosophy
Mechanical Engineering

---

by
Monsur Islam
May 2018

Accepted by:
Dr. Rodrigo Martinez-Duarte, Committee Chair
Dr. Suyi Li
Dr. Xiangchun Xuan
Dr. Garrett Pataky

ABSTRACT OF THE DISSERTATION

This dissertation presents an origami-inspired manufacturing and an additive manufacturing platform for the fabrication of 3D shapes of porous carbide material using renewable biopolymers as the carbon source. Porous carbide materials possess interesting properties including low density, high surface area, high chemical inertness, high oxidation resistance, adjustable electrical conductivity, and high mechanical properties. Due to such properties, they are used in different applications such as high temperature filters, catalytic support, thermal insulators and structural materials. The state-of-the-art to manufacture porous carbide materials includes direct foaming and templating methods. However, shaping of porous materials with these techniques relies on the use of molds, which restricts the shape complexity of the fabricated parts. Furthermore, most of the carbon precursors used in the current fabrication methods are polymers synthesized from non-renewable petroleum, which leads to a non-environment-friendly synthesis process of carbide materials. Different biopolymers including gelatin, chitosan and glucose have been demonstrated for a sustainable approach for the synthesis of carbide materials by previous authors. However, these synthesis approaches were limited only to the production of carbide nanoparticles. No method was reported so far for the fabrication of 3D shapes of porous carbide materials using the biopolymeric approaches. Hence, in this dissertation, I intend to develop manufacturing platforms which allow for the fabrication of 3D complex shapes of carbide materials using renewable biopolymers to achieve an environment-friendly process.

The scientific contributions of this dissertation are (i) use of the biopolymers for fabrication of 3D parts of porous carbide materials, (ii) development of an origami-inspired manufacturing platform to fabricate lightweight 3D complex shapes of carbonaceous materials which includes carbon and carbide, (iii) additive manufacturing of porous carbide material using extrusion-based 3D printing of a gel composite. Both the manufacturing processes are based on the basic process of mixing the biopolymers with a metal precursor, shape such composite using the mentioned techniques and heat treat such shapes to synthesize a metal carbide. During heat treatment, the biopolymers carbonize, reduce a metal from the precursor and finally carbon and metal react to originate a carbide. The renewable biopolymers that are used here as carbon precursors are carrageenan from seaweed, chitin from shrimp shells and cellulose from plants. The dissertation is organized in 3 parts: a) characterization of carbide synthesis from different renewable precursors, b) folding of a functionalized cellulose paper using origami techniques, and c) additive manufacturing of porous carbide using a biopolymer gel composite. Here, I focus on the development of tungsten carbide. In the first part I explored different biopolymers for the synthesis of WC. The parameters of interest were the proportion of the biopolymer to the tungsten precursor, the synthesis temperature, dwell time and heating rate. Synthesis temperature was proved to be the most influential parameter on the synthesis of WC followed by the ratio of the precursors. The biopolymers yield a porous WC with a purity >96% at a synthesis temperature of 1300 °C, when compared to a temperature >1400 °C used in the industrial synthesis methods. Furthermore, the grain size of the WC obtained from these biopolymers ranges from 20 nm – 60 nm, which is advantageous when compared to a grain size >100 nm obtained in the industrial synthesis processes.

In the second part I present origami-inspired manufacturing by using the cellulosic precursor utilizing its ability to fold into different origami structures. Along with the origami inspired manufacturing of porous WC, I explored the fabrication of carbonized paper as well to understand the effect of carbonization on the folded carbon precursor itself. Significant shrinkage occurred during the heat treatment process, which was attributed to the material release during the heat treatment and the structural mechanics of the origami structure. The carbonaceous origami structures featured low density and considerable mechanical properties, which compares advantageously to most of the lightweight cellular materials. In the third part, additive manufacturing of a gel composite featuring iota-carrageenan, chitin and tungsten oxide nanoparticles is presented. Heat treatment of such 3D printed gel composites yielded to 3D complex shapes of porous WC. Shrinkage of the 3D printed parts was characterized at each step of the fabrication. The 3D printed WC parts featured a density less than 3% of the bulk WC material. The parameter explored in this study was the layer thickness, as it is shown to be the most influential parameter in mechanical properties of 3D printed parts. The elastic modulus and compressive strength exhibited an increasing trend with the increase in the layer thickness. However, use of water as the solvent resulted in limitations in the 3D printing process, which includes inability to fabricate overhang or suspended structures. Future work includes finding a solvent that can replace the water to form the gel composite to facilitate fabrication of cellular lattice strictures, which is expected to show high mechanical properties at a very

low density. The 3D shapes of porous WC fabricated in these manufacturing techniques have immense potential in different applications such as structural batteries, structural filters in harsh environments and lightweight structural material.

DEDICATION

This dissertation is dedicated to my parents Nasirul Islam and Hanufa Khatun. I would like to thank them from the core of my heart for their constant support and love and being the strength and the source of motivation throughout my whole journey. Thank you and love you Abba & Maa.

A big thank you to my sisters Ferdausi Rahaman and Firoja Khatun, my brother-in-law Majibur Rahaman, and my little niece Eshika Rahaman for standing by me and believing in me throughout all these years.

Last but not the least, I thank my Grandpa, late Sk. Badiuzzaman for being a constant source of inspiration in my life. Even if he is not here with us anymore, I can still feel his blessings with me. Love you and Miss you Nana.

ACKNOWLEDGEMENTS

I would like to thank my academic advisor and a better friend, Prof. Rodrigo Martinez-Duarte, for giving me the opportunity to work on exciting research projects and providing me with many more other opportunities for development my career in research. Along with the academic progress, his mentorship has helped me to grow up as a human being as well.

Thanks to my previous advisors, Prof. Amitabha Ghosh, Prof. Ashutosh Sharma, and Prof. Marc Madou, and my high school teacher Mr. Satyen Chaterjee for all their supports and encouragements, which made me to choose and build my career in scientific research.

Thanks to my committee members, Prof. Suyi Li, Prof. Xiangchun Xian, and Prof Garrett Pataky for their kind guidance in moving forward with my research and completion of my dissertation.

Most importantly, I would like to thank my colleagues and friends in Clemson for helping me in my research projects and making my life in Clemson an exciting one. I would specially like to mention Judhajit Roy, Arghya Chakraborty, Rucha Natu, and Devin Keck for their constant support in the ups and downs of the challenging journey of grad school.

Por último, pero no menos importante, un gran agradecimiento al amor de mi vida, Diana Laura Garza Amaya, cuya presencia irremplazable en mi vida hace que mis días brillantes y oscuros se llenen de mucha energía positiva. Gracias por su amor incondicional y mantenerse fuerte todos los días y facilitar mi camino.

TABLE OF CONTENTS

Page

CHAPTER 1: Background

LIST OF PUBLICATIONS

Publications related to the dissertation

1. **M. Islam,** S. Li and R. Martinez-Duarte, "Paper Origami as a scaffold for Advanced Materials", *Advanced Materials,* in preparation.
2. **M. Islam** and R. Martinez-Duarte, "Origami: A novel method to fabricate 3D complex shapes of cellular tungsten carbide", *Advanced Engineering Materials*, in preparation.
3. **M. Islam**, J. Flach, and R. Martinez-Duarte, "Carbon Origami: A novel method to fabricate lightweight carbon cellular material", *Carbon,* 2018, 133, 140-149.
4. **M. Islam**, and R. Martinez-Duarte, "A sustainable approach for tungsten carbide synthesis using renewable biopolymers", *Ceramics International*, 2017, 43 (13), 10546 – 10553.
5. **M. Islam** and R. Martinez-Duarte, "Towards Additive Manufacturing of Tungsten Carbide Using Renewable Resources", *ECS Transactions*, 2016, 72(1), 3-9.
6. **M. Islam** and R. Martinez-Duarte, "Additive Manufacturing of Carbides using Renewable Resources" ASME International Mechanical Engineering Congress & Exposition IMECE: Houston, 2015.

Other publications:

1. R. Natu, **M. Islam**, and R. Martinez-Duarte, "Determination of streaming dielectrophoresis number for rapid and continuous cell separation", *Analytical chemistry*, in preparation.
2. D. Keck, **M. Islam**, J. Gilmore, R. Natu, S. Muhamed and R. Martinez-Duarte, "Dielectrophoretic characterization of *Candida* cells using 3D carbon electrodes", *Electrophoresis*, in preparation.
3. R. Natu, **M. Islam**, J. Gilmore, and R. Martinez-Duarte, "Shrinkage of SU-8 microstructures during carbonization", *Journal of Analytical and Applied Pyrolysis*, 2108, 138, 17-27.
4. Y. Yıldızhan, N. Erdem, **M. Islam**, R. Martinez-Duarte, and M. Elitas, "Dielectrophoretic Characterization of Live and Dead Monocytes Using 3D Carbon-Electrodes", *Sensors*, 2017, 17(11), 2691.
5. J. Gilmore, **M. Islam,** J. Duncan, R. Natu, and R. Martinez-Duarte, "Assessing the importance of the root mean square (RMS) value of different waveforms to determine

the strength of a Dielectrophoresis trapping force", *Electrophoresis*, 2017, 38 (20), 2561-2564.

6. **M. Islam**, R. Natu, M. F. Larraga-Martinez, and R. Martinez-Duarte, "Enrichment of diluted cell populations from large sample volumes using 3D carbon-electrode dielectrophoresis", *Biomicrofluidics*, 2016, 10(3), 033107.
7. J. Gilmore, **M. Islam**, and R. Martinez-Duarte, "Challenges in the Use of Compact Disc-Based Centrifugal Microfluidics for Healthcare Diagnostics at the Extreme Point of Care", *Micromachines*, 2016, 7(4), p. 52.
8. **M. Islam,** R. Natu, and R. Martinez-Duarte, "A study on the limits and advantages of using desktop cutter plotter to fabricate microfluidic networks", *Microfluidics and Nanofluidics*, 2015, 19, p. 973-985.

LIST OF FIGURES

LIST OF TABLES

INTRODUCTION

3D architectures of ceramic materials are emerging class of materials in modern engineering applications due to their structural rigidity, lightweight, and capability to function in harsh working environments [1–3]. The 3D structures of these materials integrate the structural properties with the properties of the constituent solids, which exhibits advantageous performance/weight ratio when compared to the typical monolithic bulk materials. Porous metal carbides are one of the preferable choices to manufacture such 3D architectures due to their interesting material properties. These material properties include high melting point, high mechanical properties, high electrical conductivity, excellent chemical stability, low thermal expansion co-efficient [4]. Properties of different bulk metal carbides are summarized in Table 1.1. Porous structure of carbide adds several other interesting features along with these material properties such as low density, high surface to volume ratio, and high specific strength. These properties have enabled the use of porous metal carbides in applications such as filters [5], catalysts [6,7], fuel cells [8], batteries [9,10] and erosion resistant materials for aerospace components [11].

Table 1.1: Properties of bulk metal carbides. The values are for room temperature condition [4].

Metal carbide	**Density (g/cm^3)**	**Microhardness (GPa)**	**Melting point (°C)**	**Young's modulus (GPa)**	**Heat conductivity ($Wm^{-1}K^{-1}$)**	**Thermal expansion co-efficient (10^{-6} K^{-1})**	**Electrical resistivity (μΩ cm)**
SiC	3.21	20	2830	700	120.0	4.0	0.1
TiC	4.93	28	3067	450	28.9	8.5	100
WC	15.72	23	2776	707	19.0	3.9	17
ZrC	6.46	25	3420	350	24.6	7.5	75
HfC	12.3	20	3930	420	25.1	6.1	67
$VC_{0.88}$	5.36	26	2650	430	26.8	7.2	69
NbC	7.78	18	3610	340	27.0	6.6	20
TaC	14.48	16	3985	290	22.1	6.3	15
Cr_3C_2	6.68	27	1810	380	14.0	10.3	75
Mo_2C	9.18	17	2520	530	15.0	7.8	57

The current state-of-the-art to manufacture porous carbides includes the direct foaming method [12] and the template method [13]. Shaping of the porous carbide materials into 3D shapes in such methods mostly relies on the use of a mold [14]. The disadvantage of using a mold is the fact that the shape of the final product is limited by the mold. Any change in the dimension or geometry of a part requires a manufacturing of a new mold, which is already an expensive process. Furthermore, 3D complex shapes are extremely challenging to fabricate in this current state-of-the art, because fabrication of a 3D complex mold is already a challenge. Hence, there is need for an inexpensive manufacturing technique which can eliminate the use of molding and enable manufacturing of 3D complex shapes.

The industrial production of the metal carbide parts mostly relies on the carbothermal reduction reaction (CRR). This reaction uses an excess of carbon and an inert atmosphere to reduce metal oxides to metals and then react them with carbon to generate their carbide [15,16]. The current sources of carbon in the CRR method include petroleum based carbon (carbon black, petroleum coke, asphalt), coal products, graphite mining and other mineral resources [17–20]. These carbon precursors are produced from incomplete combustion of petroleum which belong to the family of non-renewable resources. For example, in the United States alone, the usage of carbon black for the production of carbide materials is around 2 million metric tons, which needs the consumption of around 450 million of gallons of petroleum oil [21–23]. Such high demand comes from different industries such as carbide manufacturing and tire production. The use of the petroleum products is one of the main reasons for the greenhouse gas emission which has many negative effects on the environment including climate change, melt down of glaciers, and loss of biodiversity [24–26]. Therefore, there is a global push for alternative carbon sources, which should be renewable and sustainable for the planet.

This dissertation presents an origami-inspired manufacturing and an additive manufacturing platform for the fabrication of 3D complex shapes of porous carbide by using renewable biopolymers as the carbon source. We focus on synthesizing tungsten carbide (WC) in this work. The origami-inspired manufacturing uses a cellulosic precursor due to its ability to fold into 3D origami shapes. The additive manufacturing is demonstrated using a water-based biopolymer gel composite utilizing its ability of layer-by-layer deposition. To enable these manufacturing platforms to fabricate 3D complex shapes of porous WC from renewable biopolymers, we first optimize the conditions for synthesis of porous WC from the renewable biopolymers in carbothermal reduction reaction. We present detailed microstructural characterization of the synthesized WC from the biopolymers. Using the synthesis conditions for the porous WC, we develop the origami-inspired manufacturing and the additive manufacturing platform to fabricate 3D complex shapes of porous WC.

Origami is an ancient art of paper folding, where 3D complex architecture can be fabricated from a flat piece of paper by folding the paper along prescribed creases [27–29]. Traditionally, the original purpose of origami is for recreational and artistic purpose [30]. However, in the last four decades, origami has gained significant scientific and technological interest among the scientific community given its simplicity and versatility in terms of both design and fabrication [31–35]. The advantage of the origami-inspired manufacturing is the fact that origami structures are programmable and capable to feature excellent mechanical properties for lightweight applications [36–38]. Here I present a manufacturing technique to enable versatile origami shaping of carbonaceous materials that can withstand the rigors of harsh environments. This origami-inspired manufacturing of the carbonaceous materials will provide new opportunities for developing origami-based lightweight materials with properties programmed specifically to address performance applications.

Another popular method to manufacture 3D architectures is additive manufacturing or popularly known as 3D printing, in which a shape is fabricated using layer-by-layer deposition of a material, in a bottom up manufacturing operation. Additive manufacturing allows for the fabrication of 3D parts with complex geometrical features that are difficult to manufacture using traditional machining techniques [39]. Examples of such geometrical features include porous honeycomb structures for particulate filters in the exhaust of automobile engines [40]. A wide range of materials ranging from polymers to ceramics can be used to fabricate 3D parts in additive manufacturing [41]. However, the fabrication of 3D parts of carbide materials mostly relies on laser-sintering based additive manufacturing [42], which is a complex and expensive process when compared to traditional material extrusion based additive manufacturing. Here, I present the fabrication of 3D parts of porous WC using extrusion based additive manufacturing of a biopolymer gel composite followed by a heat-treatment process.

The carbon precursor material I use here for the fabrication of 3D parts of porous carbide material are biopolymers. Biopolymers are renewable and abundant in nature. They have been used in different applications for sustainable consumptions. As biopolymers are mainly hydrocarbons, biopolymers have been used as a carbon source in various applications [43,44]. The biopolymers can be easily pyrolyzed and converted to carbon. Such carbon can replace the use of petroleum-based carbon in different applications. For an example, in the United States, it is estimated that if the biopolymers are used as a source of carbon at its full potential, it can save up to a third of current petroleum consumption in energy applications by 2030 [45]. However, large quantities of the biopolymers are either burned in open air or left as environmental waste. For the sustainability of the world, it is important to utilize such environmental waste. Along with the environmental impact, the use of biopolymers as a carbon source has socio-economic impact. The sources of specific biopolymers are cultivated for commercial production of the biopolymers which are used mainly in the food industry. An example is the sea-weed industry in Indonesia and the Philippines for production of carrageenan [46]. Hence, the use of the biopolymers as a carbon source will have a further positive impact on the socio-economic conditions of these countries. Different biopolymers including gelatin, chitosan and sucrose have been demonstrated for synthesis of metal carbides [47–49]. However, the carbide synthesis from these biopolymers is only limited to the formation of carbide nanoparticles.

Therefore, the contributions of this dissertation are: (1) *the use of biopolymers for the fabrication of 3D complex shapes of porous carbide materials;* (2) *development of an origami-inspired manufacturing platform for the fabrication of lightweight 3D complex shapes of porous carbonaceous materials;* (3) *additive manufacturing of porous WC using extrusion- based 3D printing of a biopolymer gel.*

The work presented here is organized as follows. Chapter 1 presents a general background on the two main topics of this dissertation: synthesis of carbide and 3D shaping of porous carbide. Chapter 2 provides the details of the synthesis and characterization of tungsten carbide using different fibrous biopolymers as the bio-template as well as the carbon source. Chapter 3 details the characterization of the WC synthesized while using a biopolymer gel composite as the precursor material. Chapter 4 presents the details of the origami-inspired manufacturing of the carbonaceous materials including carbon and WC using cellulosic paper as the precursor material. Chapter 5 one details the fabrication of 3D shapes of porous WC using an additive manufacturing platform. Lastly, a conclusion and future work of this dissertation is presented at the last section of this dissertation.

Chapter 1: Background

The focus of this dissertation is to establish advanced manufacturing platforms for fabrication of 3D shapes of porous carbide materials. The important features of this dissertation are: (1) the carbon sources used in the carbide synthesis are renewable biopolymers, (2) the carbides are of porous nature, (3) the parts I tend to fabricate here feature 3D complex architecture. The synthesis of the metal carbide from these biopolymers relies on the carbothermal reduction reaction mechanism.

To assess the importance of this dissertation, I present a detailed background of the points mentioned above in this chapter. I first provide a general overview of the synthesis mechanism for metal carbide in carbothermal reduction reaction. A brief overview of the traditional methods is presented next for synthesis of porous carbide using the carbothermal reduction reaction. Next, I review the biopolymers which have been used so far for synthesis of porous carbide material. In the last section, I present the techniques so far used to fabricate 3D parts of porous carbides.

1.1. Synthesis mechanism of metal carbide in carbothermal reduction reaction

In carbothermal reduction reaction (CRR), a metal oxide (M_xO_y) is generally used as the metal precursor and heat treated in high temperature in presence of carbon [50]. Different other metal precursors have been also used for the synthesis of a metal carbide (MC) in

CRR method. However, these metal precursors reduce to the metal oxide during the heat treatment. Carbon black is the most popular carbon source in the industrial process to produce metal carbides via CRR method. However, different polymeric carbon precursors have been also investigated in the CRR method to produce metal carbides. During heat treatment, these polymeric carbon precursors decomposes to a carbon rich material by a temperature when the metal precursor also reduces to the metal oxide. This temperature is typically in the range 400 °C – 500 °C [51–53]. Hence, the CRR starts with the metal oxide and the carbon material.

The CRR involves two steps: reduction step and carburization step. In the reduction step, the metal oxide gets reduced to the metal nanoparticle in the presence of carbon. Once, the metal oxide is completely reduced, it is expected to be surrounded by carbon material. At higher temperature, the surrounding carbon diffuses into the metal particle and carburizes the metal particle to from metal carbide. The chemical reactions that occur during the reduction and carburization steps can be summarized by Equations 1.1 and 1.2 respectively.

$$M_xO_y + yC \rightarrow xM + yCO \qquad \text{Equation 1.1}$$

$$M + C \rightarrow MC \qquad \text{Equation 1.2}$$

In this dissertation, I focus on synthesizing tungsten carbide (WC). Therefore, I further elaborate the discussion of the synthesis mechanism of WC in detail. The synthesis mechanism of WC from solid state reaction of tungsten trioxide (WO_3) and carbon in CRR is extensively studied by Venables and Brown [54,55]. The CRR begins in a temperature range 600 – 780 °C [56]. However, this starting temperature depends on the grain size of the reacting materials, impurity contents and the reaction environment. The reduction process of the WO_3 is illustrated in the Figure 1.1. At the starting state of the reduction process, the WO_3 particles are surrounded by carbon. Because of that, direct reduction of WO_3 occurs by the solid carbon which is in direct contact of the oxide particle. During this direct reduction process, the solid carbon reacts with the oxygen atom of WO_3 and forms gaseous CO. Due to the formation of gaseous CO, a shell of porous WO_2 is formed around the remaining of the WO_3 particle. During the formation of WO_2, several other intermediate oxide phases such as $W_{20}O_{58}$ and $W_{18}O_{49}$ can be formed as well [57]. At such condition, the solid carbon cannot get direct contact with the WO_3. Hence, further reduction occurs due to the diffusion of the gaseous CO. The CO diffuses through the porous shell of WO_2 and reacts with the non-porous WO_3 to form WO_2 and gaseous CO_2. With increasing temperature, the diffusion rate increases and the unreacted WO_3 core shrinks and produces more porous WO_2. Eventually the whole WO_3 get reduced and forms porous WO_2. Next the porous WO_2 starts reducing to metallic W by both solid carbon and gaseous CO. The reduction rate of WO_2 to W is faster than WO_3 to WO_2 because of higher diffusion rate of CO thanks to the porous nature of WO_2. Finally at a temperature around 900 °C, the reduction to metallic W is completed [55]. The reactions that occurs during this reduction process can be summarized by Equations 1.3-1.6 [55,57].

$WO_3 + C \rightarrow WO_2 + CO\ (g)$ Equation 1.3

$WO_3 + CO\ (g) \rightarrow WO_2 + CO_2(g)$ Equation 1.4

$WO_2 + 2CO\ (g) \rightarrow W + 2CO_2\ (g)$ Equation 1.5

$CO_2(g) + C \rightarrow 2CO(g)$ Equation 1.6

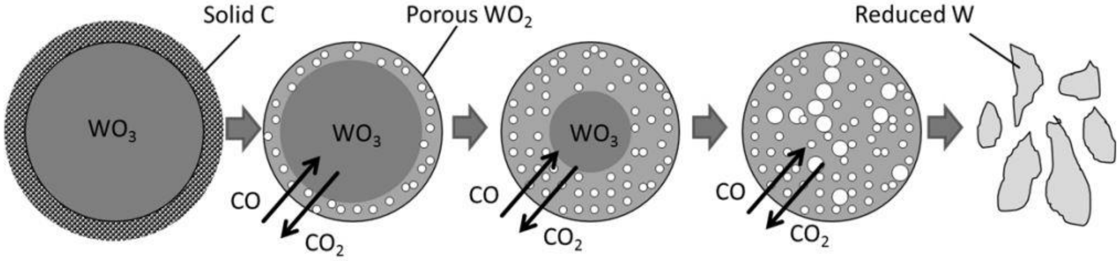

Figure 1.1: Schematic of the reduction process of WO_3 in presence of carbon during the carbothermal reduction reaction for WC synthesis [56].

Once all the WO_3 get reduced to metallic W, the carburization of the metallic W starts. Figure 1.2 illustrates the carburization process of the metallic W. At the end of the reduction process, the tungsten particles are expected to be surrounded by the carbon. The reaction starts with the formation of activated carbon at the surface of the W particle. The activated carbon starts diffusing into the W particle to form a shell of WC. Once the shell of WC is formed, the diffusion rate of activated carbon slows [56]. Because of the slow diffusion, the inner metallic W forms a metastable hemicarbide phase W_2C. Now the activated carbon diffuses through WC and W_2C shell to reach the core W. With increasing temperature, the diffusion rate increases and the shell for WC and W_2C also increases. Eventually the inner W core carburizes to W_2C. Higher temperature facilitates further diffusion of the activated carbon through the WC shell and causes complete carburization of the interior W_2C to form a complete WC particle. The reaction involved in the carburization steps are expressed by the Equations 1.7-1.9 [58].

$$W + C \rightarrow WC \qquad \text{Equation 1.7}$$

$$2W + C \rightarrow W_2C \qquad \text{Equation 1.8}$$

$$W_2C + C \rightarrow 2WC \qquad \text{Equation 1.9}$$

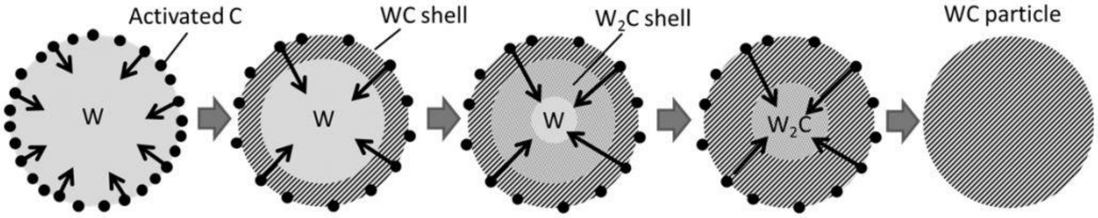

Figure 1.2: Schematic of the carburization process of metallic tungsten particle during WC synthesis via carbothermal reduction reaction [56].

1.2. Methods for synthesis of porous carbide material

The synthesis methods for porous carbide material is extensively reviewed by Borchardt et al [14]. The strategies used to synthesize porous carbide materials in industries can be categorized in three main strategies: (i) polymeric template method, (ii) direct foaming method, and (iii) sacrificial template method. All the three strategies are illustrated in the Figure 1.3 and described briefly in following sections.

1.2.1. Polymeric template method

In the polymeric template method, a flexible polymeric cellular pre-form is used as a template. The cellular pre-form is generally made of polyurethane, polystyrene, cellulose or latex [14]. The cellular pre-form is then infiltrated with a carbide slurry. The slurry is prepared by mixing carbide particles with a binder. The choice of binder is important here, as it ensures the attractive interaction of the slurry with the template material. The amount of binder is also important, as it determines the rheology of the slurry necessary to infiltrate the template. In some cases, a precursor solution is preferred instead of the carbide slurry. In such cases, the choice of the solvent is important for impregnation to the polymeric pre-form. Once proper infiltration of the slurry or the precursor solution is achieved into the cellular pre-form, the green body is dried, and heat treated in high temperature. The high temperature process burns out the template material. In case of the slurry-based infiltration, the heat treatment process sinters the carbide particles. For precursor solution, the heat treatment facilitates the reaction between the precursors to synthesize carbide followed by sintering of the synthesized carbides. The cellular carbide obtained in such process is called reticulated carbide. The polymeric template method allows for produce carbide parts featuring high porosity and open cell structures. Carbides featuring a porosity >90% can be produced in this method. Such carbides are preferable for applications such as filters and lightweight structural materials [59]. However, the heat treatment process should be controlled precisely in this method. High heating ramp during the heat treatment may induce excessive thermal stress to the cellular structure, which causes defects in the final carbide structures.

1.2.2 Direct foaming method

Direct foaming is achieved by generating bubbles in a liquid precursor slurry. Most common method to generate bubbles in the liquid precursor is gas injection during mechanical stirring of the liquid precursors. Another method is to add blowing agents such as volatile liquids or decomposable solids in the liquid precursor [12]. Bubble generation can be further achieved by chemical reaction resulting in gaseous substances such as hydrogen or water vapor [60]. Once bubbles are generated in the liquid precursor, the precursor material is stabilized to maintain the porous morphology. The stabilization of the green body can be achieved by different methods such as cross-linking, polymerization, and freezing [14]. The stabilized green body is further heat treated at high temperature to obtain a porous network of carbide material. A carbide material with a wide range of pore sizes and a porosity up to 95% can be achieved in this method. The advantage of this process is capability to produce dense and defect free carbide struts, which makes the foam structure stronger compared to the porous structure obtained in polymeric replica method [59]. However, the growth of the bubbles needs to be controlled in the direct foaming method. Faster growth rate induces stress to the struts resulting in fracturing the struts.

1.2.3. Sacrificial template method

In the sacrificial template method, a sacrificial template material such as mesoporous silica is dissolved within a liquid precursor solution. After drying, the precursor solution is heat-treated at high temperature to produce carbide material. During the heat treatment, the template material remains unreacted. Upon synthesis of the carbide material, the template material is removed by dissolving by highly corrosive acids such as hydrofluoric acid [61]. Removal of the sacrificial template material generates porous structure in the carbide material. The main advantage of this method is precise control over the total porosity, shape of the pores and the amount of open and closed pores in the material [14]. The pore size obtained in this method ranges from 1 μm to 700 μm and a porosity ranging from 15% to 95% can be achieved in this method. However, the choice of the template material is important, because the sacrificial material should remain unreacted with the other precursor materials at high temperature. This criterion limits the choices for the template material. Furthermore, use of acidic environment to dissolve the sacrificial material demands high precautions for safety purpose of the user.

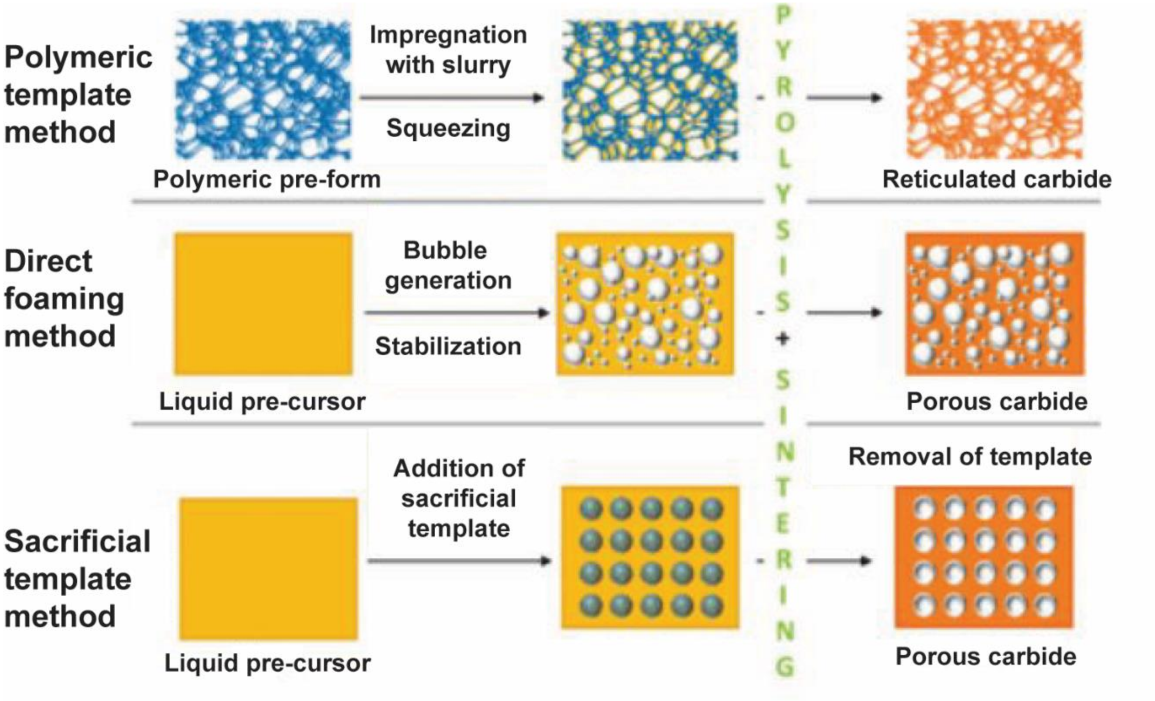

Figure 1.3: Different strategies for the fabrication of porous carbide material [14].

1.3. Biopolymers used for synthesis of porous metal carbide

1.3.1. Biomorphic route

Biomorphic route is basically a polymeric template method, where a biological preform is used as the template material. However, here the biological template also serves as the source of carbon required for carbide synthesis. Furthermore, instead of a carbide slurry, a metal precursor is infiltrated into the biological template, which provides the metal for the carbothermal reduction reaction. Several researchers used this biomorphic synthesis method to introduce natural porosity to the ceramic matrix. The biomorphic synthesis has been studied in the last two decades, especially for the synthesis of biomorphic SiC from wood preform. Wood is a composite of three major biopolymeric constituents, which are cellulose, lignin and hemicellulose [62,63]. Other minor constituents include fat, oil, wax, sugar and alcaloids. The synthesis of biomorphic SiC includes carbonization of the wood preform in an inert atmosphere at a temperature more than 700 °C. During this carbonization step, the constituent biopolymers decompose to carbon and form a bio-carbon template. The bio-carbon template is further impregnated with silica sol by vacuum or pressure infiltration process. The silica impregnated bio-carbon is heat treated in inert atmosphere at a temperature in a range 1400 °C – 1600 °C to produce SiC through carbothermal reduction reaction. This process was first demonstrated by Ota et al. [64] using oak wood. Later on, several researchers adapted this method to synthesize biomorphic SiC from different other woods such as oak, maple, beech, ebony, balsa, pine, and bamboo to achieve different degree of porosity naturally [65–69]. The biomorphic synthesis process was further demonstrated for synthesis of other metal carbides. Sieber et al. converted pine wood into titanium carbide by chemical vapor infiltration reaction process [70]. Rambo et al. reported the synthesis of TiC and ZrC ceramics from pine wood preform by infiltration of Ti- and Zr- alkoxides [71].

1.3.2. Biopolymer gel route

A recent approach that has been gaining attention for synthesis of metal carbides, is use of organic gelators. A biopolymer gel is used in this process to disperse the suitable metal precursor within a homogeneous gel precursor. Biopolymer gel helps to control the nucleation and growth of the metal carbide [47]. Upon heat treatment, the metal precursor reduces to metal and the gel decomposes to carbon simultaneously surrounding the metal nanoparticle. The surrounding carbon prevents the metal nanoparticle from sintering to the neighbor metal nanoparticles. On further heating, the surrounding carbon can diffuse into the metal nanoparticle to start forming metal carbide. Figure 1.4 illustrates the reaction mechanism to from metal carbide from the biopolymer gel route. Different gel forming biopolymers have been used so far for the carbide synthesis. Markus Antonietti and his group demonstrated a generalized synthesis process for different metal carbide using an urea-based gel [72,73]. In brief, they dissolved a metal salt in an alcohol solvent to obtain a clear solution. Urea was added to the alcoholic solution to achieve a specific molar ratio of the precursor material necessary for the synthesis of carbide material. The solution was stirred continuously to achieve a clear gel. The gel was heat treated in a nitrogen atmosphere at high temperature higher or equal to 800 °C. Upon heat treatment, nanomaterials of metal carbides were obtained. Using this method, they demonstrated synthesis of tungsten carbide (WC), molybdenum carbide (Mo_2C), chromium carbide (Cr_3C_2) and niobium carbide (NbC).

Schnepp et al. reported synthesis of highly magnetic iron carbide nanoparticles from a gelatin and chitosan-based gel [47]. They added an aqueous solution of iron acetate to aqueous solutions of the biopolymer with fast stirring to form the gel. The gel was calcined at 650 °C with a heating rate of 2 °C/min in a nitrogen atmosphere. The iron carbide nanoparticles obtained after the heat treatment featured a mean particle diameter of 20 nm.

Holgate et al. demonstrated use of chitosan gel for synthesis of WC-Co nanoparticles [74]. They mixed ammonium tungstate and cobalt nitrate to a solution of chitosan and cast it on a petri-dish to form gel. The gel was heat treated at 900 °C in nitrogen atmosphere to obtain WC-Co nanoparticles featuring an average diameter of 80 ± 20 nm. However, presence of metallic tungsten (W) and tungsten hemicarbide (W_2C) could be observed in the XRD pattern of the synthesized material.

Patra et al. used Gum Karaya (GK) as the gel forming biopolymer for the synthesis of zirconium carbide (ZrC) [75]. They dissolved GK in distilled water and added zirconyl oxychloride octahydrate to the solution. The solution was stirred for 3 hours at 60 °C with the presence of sodium hydroxide to form a gel. The gel was dried, and heat treated at 1500 °C in argon atmosphere to synthesize ZrC. The ZrC featured average crystallite size of ~40 nm.

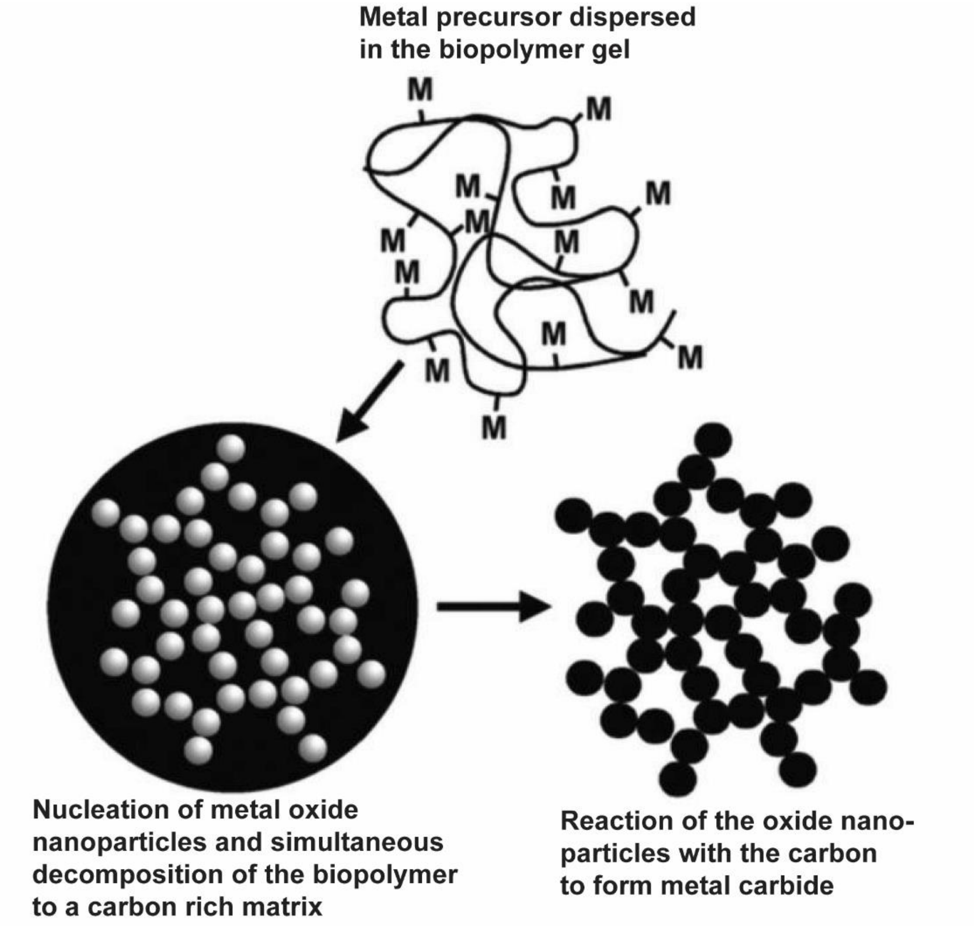

Figure 1.4: The schematic to illustrate the reaction mechanism for the synthesis of metal carbide via biopolymer gel route [47].

1.4. Fabrication of 3D shapes of porous carbide material

Use of biopolymers to obtain a shaped 3D structure of porous carbide is still not explored. The biopolymer gel route is limited to synthesis of carbide nanoparticles only. The biomorphic carbide synthesis can be considered as an existing method to obtain 3D shape of porous carbon from biopolymers. This is because the carbide material obtained in the biomorphic synthesis retains the structure of the precursor wood material [76]. However, no report is available on manufacturing of different shapes of porous carbide using the biomorphic route. Hence, here we review the methods to fabricate 3D shapes of the porous carbide with traditional carbon precursors.

The traditional method to fabricate 3D shapes of porous carbide is incomplete sintering method [77]. In this method, a slurry is prepared using coarse carbide grains with a carbonaceous binder. The slurry is molded into 3D shapes using an external mold. The molded green body is sintered at a temperature as high as 2000 °C. Partial sintering is performed by controlling the sinter pressure to achieve a porous network of carbide.

An alternating method that is adopted by different industries for the manufacturing of 3D shapes of porous carbide is converting a porous shaped carbon material into porous shaped carbide material via gas-solid phase reaction [78]. Mainly SiC is being produced in this method so far. In this method, an inert gas carries a gas phase silicon precursor through a porous carbon at high temperature. The silicon precursor infiltrates the porous network of carbon and reacts with the carbon to form SiC [79]. The synthesis temperature is kept below 1400 °C to prevent excessive sintering of the SiC grains.

Nguyen and Pham developed self-bonded SiC synthesis method to fabricate 3D shapes of porous SiC [80]. In this method, a green body is prepared by mechanically mixing a metallic silicon, carbon (carbon black, Cabot, and a high carbon yield carbon binder as carbon precursors) and temporary binders such as methyl cellulose, polyvinyl alcohol, sodium silicate, and SiO_2 sol followed by shaping using standard technologies such as extrusion, spheronisation, granulation and pelletizing. To fabricated open cell 3D structures, a replica method is used here. A slurry is prepared using the raw materials with an increased amount of binder to achieve the required rheology. A polyurethane foam is then coated by this slurry. The green body is dried overnight followed by a heat treatment at 1360 °C. During the heat treatment, the high carbon yield binder is carbonized to form amorphous carbon which binds the carbon black and metallic silicon. At temperature >1000 °C, the silicon reacts with the carbon to form SiC. After the formation of SiC, the SiC is subjected to a heat treatment in oxygen at 800 °C to burn out excess carbon present in the material. Examples of the 3D shapes of carbide produced in this method are shown in Figure 1.5a.

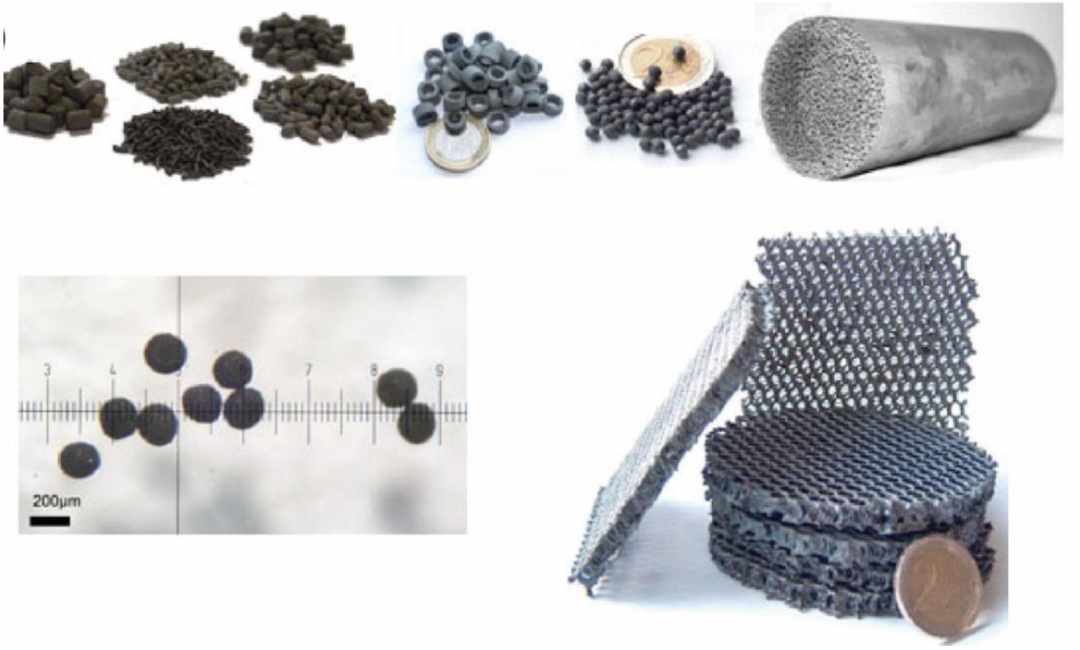

Figure 1.5: Self-bonded SiC in various 3D shapes [80].

CHAPTER 2: Synthesis of carbide from fibrous biopolymers

The focus of this is dissertation is fabrication of 3D shapes of porous carbide material. To fabricate the 3D shapes, I employ commercially available biopolymers as the carbon precursor in the synthesis of the porous carbide. Use of biopolymers offers a sustainable approach in various applications. As mentioned in the Introduction of this dissertation, biopolymers have a strong impact on the energy applications as a sustainable and renewable precursor of carbon. The use of biopolymers for production of carbide materials is detailed in Chapter 1.

One of the manufacturing techniques, I am focusing in this dissertation, is the origami-inspired manufacturing. As origami is a paper-folding technique, it is important to choose a biopolymeric pre-form which can be easily creased and folded into different origami shapes. A paper pre-form containing fibrous network of biopolymer is suitable for such origami-inspired manufacturing. Here I use three different types of biopolymeric paper which can be used to fabricate 3D complex shapes of carbide. The biopolymeric papers include pure cellulosic chromatography (CG) paper, bacterial cellulose sheet and rice paper.

The constituent biopolymer for both cellulosic paper and bacterial cellulose sheet is cellulose. Cellulose is the most abundant biopolymer on the earth. Cellulose is synthesized by plants, algae, tunicated sea animals and some bacteria [81,82]. Hence, cellulose is considered as one of the important renewable biopolymers for replacement of petroleum based non-renewable resources [83,84].

The main constituent of rice paper is starch [85]. Starch is the second most abundant biopolymer available in nature. It is mainly produced by the plants as their source of stored energy. Starch can be found in plant roots, stalks, crops such as rice, wheat, tapioca, corn and potato [86]. Starch is extracted from the plants by wet grinding, sieving and drying or by one or more chemical processes to achieve specific properties [87]. The annual production of starch in the year 2000 was estimated to be 48.5 million tons [88]. Hence, based on the huge demand and well-established manufacturing industry, starch can be considered as another important renewable biopolymer as an alternative to petroleum based non-renewable precursors.

Before going into the detail for the fabrication of the 3D parts using origami-inspired manufacturing process, it is important to optimize the conditions to synthesize carbide material using these fibrous biopolymers. Hence, in this chapter, I study the impact of the synthesis conditions on the synthesis of the porous carbide from the fibrous biopolymers. The general methodology I use here to optimize the synthesis conditions is illustrated in Figure 2.1. The fibrous biopolymers are infiltrated with suitable metal precursor and heat treated at high temperature in inert atmosphere. The basic principle is to first carbonize the biopolymer, then reduce the metal precursor to metal and finally react the excess carbon with the metal to obtain its carbide. As mentioned earlier, I focus on the synthesis of tungsten carbide (WC) in this dissertation. The synthesis conditions I seek to optimize here are: (1) amount of metal precursor needed to obtain pure carbide material, (2) synthesis temperature, and (3) heating rate. The optimized synthesis conditions will be further used during the fabrication of the 3D shapes of porous carbides from these biopolymers.

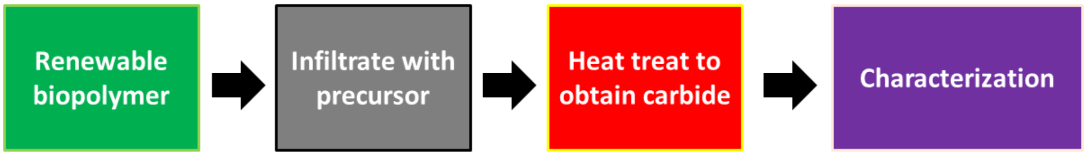

Figure 2.1: The general methodology used in this work for synthesis of carbide from biopolymers.

In this chapter, I first study the carbonization of the biopolymers in terms of the material composition and microstructural properties of the carbonized samples. Further I investigate the synthesis of WC from these biopolymers using an aqueous solution of tungsten precursor. Finally, I continue in-detail optimization of the synthesis conditions and study the effect of the synthesis conditions on the microstructural properties of the synthesized WC materials.

2.1. Experimental section

2.1.1. Materials

Pure cellulose chromatography (CG) paper (Fisherbrand Chromatography Paper, Cat. No. 05-714-1) with thickness of 0.19 mm was used for this work. The CG paper is composed of randomly oriented cellulose fibers featuring average fiber diameter of 17.48 ± 3.06 µm. The cellulose fibers are originally derived from wood pulp. The cellulose fibers derived from the wood pulp originally feature a hollow structure having a lumen diameter ranging from 8 µm to 12 µm [89]. During paper manufacturing, the lumen of fibers is likely to be collapsed by different amounts [90]. The BC pellicle was prepared following the synthesis procedure in previous reports [91,92]. The BC pellicle is a dense mesh of cellulose nanofibers having an average fiber diameter of 80.09 ± 16.85 nm. BC possesses higher purity and high degree of crystallinity while compared to plant cellulose [93]. The rice paper used here is a commercial grade edible rice paper. The commercial name of the rice paper used here is Banh Trang. The edible rice paper is prepared from rice flour, the primary component of which is starch [85].

An aqueous solution of ammonium metatungstate (AMT) was used as the tungsten precursor in this work. Solution based precursors have been shown to be a preferable choice for infiltration into cellular template materials [13,51,94]. Nanoparticle based suspensions are not preferred in the case of fibrous template-based synthesis. This is because the high uncertainly of homogenous infiltration and high chances of clogging small pores between the fibers. AMT has been shown to be a preferable choice for solution based tungsten precursor in different WC synthesis articles because of its easy solubility in water [95–97]. The AMT used in our work was purchased from Sigma Aldrich (Cat. No. 463922).

2.1.2. Experimental process

AMT was added to ultra-pure water to obtain an aqueous solution of AMT with concentration of 20% (wt%). The different precursors were immersed in the 20% AMT solution for 15 minutes for infiltration and introduced in a tube furnace (TF1700, Across International, USA) for heat treatment in wet condition.

The biopolymers infiltrated with AMT were heat treated in a vacuum environment (vacuum pressure = -762 Torr). The heating protocol was: (i) heating from room temperature to 300 °C with a heating ramp of 5 °C/min; (ii) dwell at 300 °C for 30 minutes to eliminate any oxygen in the heating tube; (iii) heating from 300 °C to 1300 °C with a heating ramp of 5 °C/min; (iv) dwell at 1300 °C for 3 hours; and (v) cooling down to room temperature with a cooling rate of 5 °C/min. Based on the results obtained from the heat treatment at 1300 °C, a design of experiment (DOE) and Taguchi method were further implemented to study the effect of the synthesis parameters and optimize the parameters for WC synthesis from these biopolymers.

2.1.3. Characterization

Thermogravimetric analysis (TGA) was performed for the biopolymers in nitrogen environment up to 900 °C with a heating rate of 5 °C/min to determine the carbon yield of the biopolymers. The crystallinity and the composition of the heat-treated samples were characterized by X-ray diffraction (XRD) spectroscopy using Cu-Kα radiation (Rigaku Ultima IV, Japan). The XRD patterns were matched with the material database of International Centre for Diffraction Database (ICDD) for determination of the material composition. We characterized the microstructure of the heat-treated samples using field emission scanning electron microscopy (FESEM, S4800, Hitachi, Japan). The grain size of the heat-treated samples was estimated from the XRD patterns using the Scherrer equation. This equation is only valid for grain sizes smaller than 100 nm [98]. The average grain size D is calculated in Scherrer equation (Equation 2.1) from the wavelength of X-ray λ, the Bragg angle θ, the half width of the diffraction peak B and a constant k, which is generally taken as 1.

$$D = \frac{k\alpha}{B cos\theta} \qquad \text{Equation 2.1}$$

2.1.4. Design of Experiment (DOE)

Experiments for optimization of the synthesis parameters were planned using an orthogonal array proposed by the Taguchi method. The orthogonal array provides different combinations of parameters and their levels for each experiments. According to the Taguchi method, the orthogonal array allows to study the entire parameter space with a minimum number of experiments. The synthesis parameters we studied here were concentration of AMT, final temperature of heat treatment and the heating rate in the step 3 of the heat treatment with three levels for each as shown in Table 2.1.

Table 2.1: Levels of the synthesis parameters used for the Taguchi method for synthesis of WC from fibrous biopolymers.

Parameters	**Level 1**	**Level 2**	**Level 3**
Temperature	1100 °C	1200 °C	1300 °C
Heating rate	1 °C/min	2.5 °C/min	5 °C/min
AMT	10%	20%	50%

L9 orthogonal arrays were chosen for three synthesis parameters and three levels for each parameter. L9 orthogonal arrays provides nine set of experiments with best combinations of the synthesis parameters to study the results within the entire design space. The output signal chosen in this study was the relative amount of WC obtained after heat treatment. The relative amount of WC was determined by Equation 2.2. For analyzing the results in the Taguchi method, there exists three forms of signal to noise (S/N) ratio such as smaller-the-better, nominal-the-better, and larger-the-better. The larger-the-better S/N ratio was chosen in this study, as the relative amount of WC should be highest at the optimum conditions. For the larger-the-better condition, the S/N is determined by the Equation 2.3. Table 2.2 details the L9 orthogonal arrays and the corresponding results. ANOVA was used to analyze the effect of synthesis parameters on the output signal. Minitab 17 software was used to formulate the Taguchi orthogonal array and for computation for S/N ratio at each level of the control factors and in ANOVA analysis.

$$Relative\ amount\ of\ WC = \frac{Sum\ of\ the\ intensites\ of\ the\ peaks\ for\ WC\ in\ XRD}{Sum\ of\ the\ intensities\ of\ all\ the\ peaks\ present\ in\ XRD} \times 100\%$$

Equation 2.2

$$S/N = -10\log[mean\ of\ sum\ of\ squares\ of\ reciprocal\ of\ measured\ data]$$

Equation 2.3

Table 2.2: Experimental design in Taguchi L9 orthogonal array for synthesis of WC from fibrous biopolymers.

Experiment no	**Temperature (°C)**	**Heating rate (°C/min)**	**AMT (%)**
1	1100	1	50
2	1100	2.5	10
3	1100	5	20
4	1200	1	10
5	1200	2.5	20
6	1200	5	50
7	1300	1	20
8	1300	2.5	50
9	1300	5	10

2.2. Results and discussion

2.2.1. Carbonization of the biopolymers

We used TGA to determine the carbon yield from each of the biopolymers (Figure 2.2a). All the biopolymers exhibited a similar trend in their carbonization: (i) weight loss due to evaporation of water, (ii) a drastic weight loss due to thermal decomposition of the biopolymer, and (iii) gradual weight loss due to the escape of heteroatoms from the material. For CG paper, about 5% weight loss occurred up to 300 °C due to the evaporation of the water adsorbed on the cellulose fibers. In the temperature range 300 °C – 380 °C, about 85% weight loss occurred due to thermal decomposition of the cellulose and evaporation of the volatile by-products such as levoglucosan, hydroxyacetaldehyde, acetol, CO and CO_2 [99]. Above 380 °C, a gradual weight loss with a loss rate of 0.0097%/°C is observed due to the escape of oxygen and hydrogen atoms in terms of CO, CO_2 and C_xH_y [100]. At 900 °C, the carbon yield obtained from CG paper is 4.3%. Similar to CG paper, the BC also exhibits initial weight loss due to evaporation of water up to around 300 °C. However, the initial weight loss for BC is around 13%. BC is known to be an excellent water absorber material [101]. Hence, the moisture absorbed by BC is relatively higher than CG paper, which yields a higher weight loss due to evaporation of water. In the temperature range 300 °C – 380 °C, around 44% weight loss is observed for BC due to the thermal decomposition of the cellulose. Further 22% weight loss occurs in the temperature range 380 °C – 650 °C due to escape of other lighter volatile byproducts and oxygen and hydrogen atoms [102]. At 900 °C, the BC results in a carbon yield of 20%. As seen in the TGA results, the thermal degradation behavior of BC is significantly different than the CG paper, although the constituent material for both cases is cellulose. The thermal degradation behavior is known to depend of various structural parameters of the biopolymer which includes the crystallinity, molecular weight and orientation of the fibers [103]. It has been reported that BC exhibits higher crystallinity, better molecular arrangement and higher purity when compared to the cellulose derived from plant [104]. This may be the reason BC results in higher carbon yield than the CG paper. However, further study is needed to confirm this hypothesis. The carbon yield of the CG paper and the BC is in agreement with previous reports [105,106].

The main constituent of rice paper is starch. Hence, the TGA result of rice paper resembles that of starch. At room temperature, starch adsorbs significant amount of moisture due to its high hydrophilic nature [107]. Hence, around 13% weight loss can be observed due to the evaporation of the adsorbed water up to a temperature of 240 °C. The weight loss due to the thermal decomposition starts around 240 °C. A steep weight loss curve can be observed up to 350 °C followed by a gradual weight loss curve up to 600 °C. Similar to the rice paper, the steep weight loss curve is caused by the thermal decomposition of the starch and the gradual weight loss is attributed to the late evaporation of lighter volatile byproducts. The carbon yield at 900 °C for rice paper is 21.4%, which is slightly higher than starch (carbon yield ~ 15% [108]). The higher yield may be a result of other additives used for commercial production of rice papers.

Figure 2.2b shows the XRD pattern of the carbon material obtained from the pyrolysis of the biopolymers. The carbon from all the biopolymers are of amorphous nature. In all the XRD patterns, weak and broad peaks centered around $2\theta = 24°$ and $2\theta = 43°$ can be observed, which are the reflections of (022) and (100) planes of carbon material [109,110]. This confirms that the carbon obtained from the biopolymers is of amorphous nature. However, the peaks for the BC derived carbon are sharper when compared to the other two biopolymers. This again suggests the carbon from the BC is more crystalline than CG paper and rice paper derived carbon. This is further confirmed by the Raman spectra of the carbon samples (Figure 2.2c). Two peaks can be observed in between 1000 cm^{-1} and 1800 cm^{-1} in the Raman spectra of each carbon sample. The peak around 1300 cm^{-1} is D-band, which represents the disordered carbon present in the sample. The other peak, which is around 1580 cm^{-1} is G-band, representative of the crystalline planes of carbon presnet in the sample. Hence, the ratio of the intensities of D-band (I_D) and G-band (I_G) represents the degree of graphitization of the carbon sample [111]. For pure graphite, the ratio I_D/I_G is zero. Hence, lower value of I_D/I_G suggests higher crystallinity of the carbon material. The ratio for BC derived carbon is 1.28, whereas the ratio is 1.48 and 1.45 for rice paper and CG paper derived carbon. Clearly BC derived carbon shows higher crystallinity among the three carbon samples studied here.

Carbonization of the biopolymers studied here results in a cellular structure of carbon as shown in Figure 2.2d-f. The carbon sample derived from CG paper is a fibril network of randomly oriented carbon fibers featuring average diameter of 5.26 ± 2.53 µm. The sample obtained from BC is a fibril network of randomly oriented interconnected carbon fibers. The average fiber diameter is 21.33 ± 8.96 nm. On the contrary, the rice paper yields to a stochastic foam of carbon featuring open cells.

All the three biopolymers studied here exhibit high thermal stability; the biopolymers are resistant to thermal degradation up to at least 240 °C. This is important for high temperature carbide synthesis. This high thermal stability allows to retain the polymeric template of the biopolymers during a significant portion of the calcination step [47]. This helps the biopolymer to control the nucleation and growth of the crystalline intermediates and finally obtain similar morphology of the biopolymer in the heat treatment process [112].

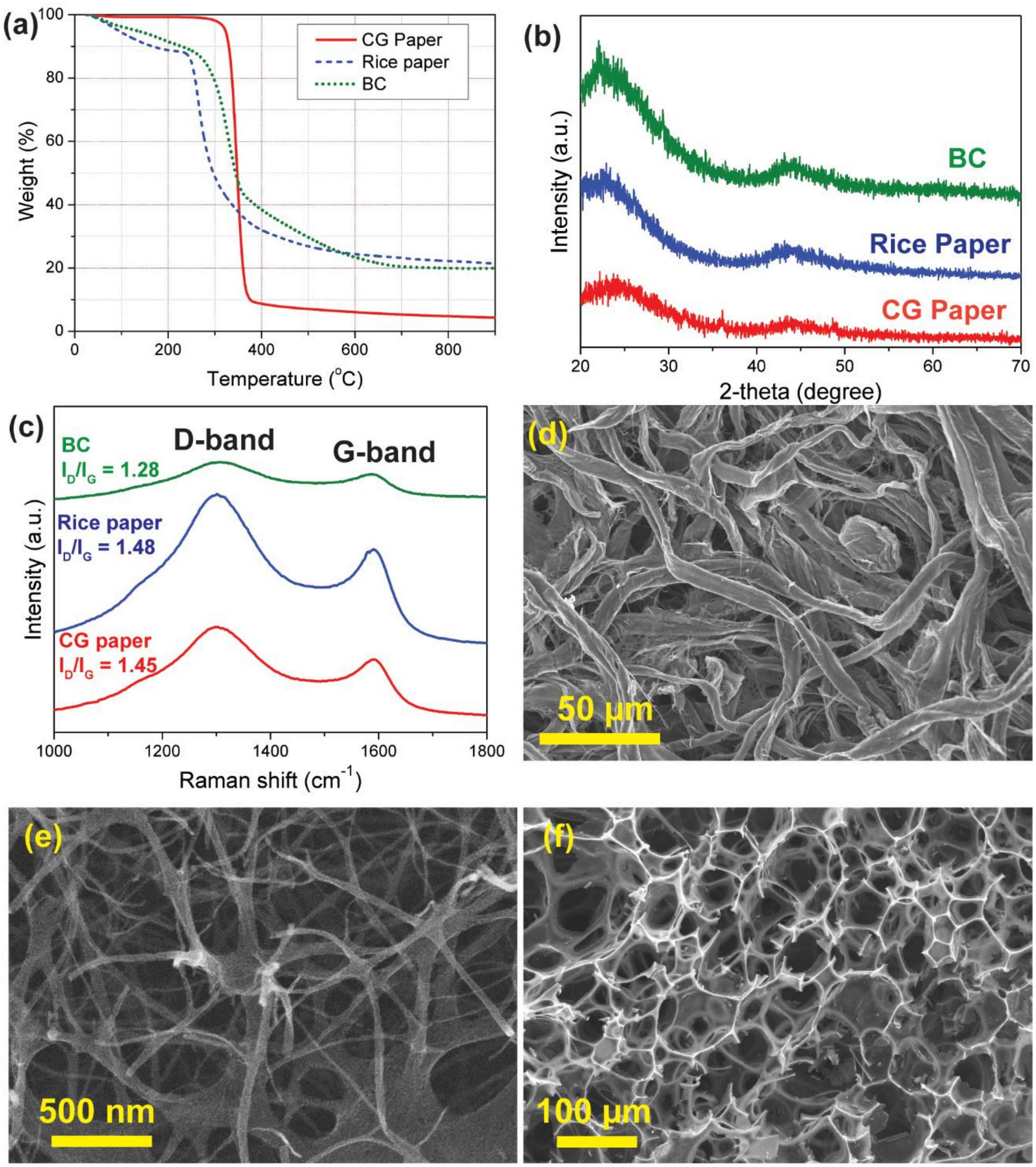

Figure 2.2: (a) TGA, (b) XRD pattern and (c) Raman spectra of the carbon obtained from CG paper, BC and rice paper. FESEM images of the carbon obtained from (d) CG paper, (e) BC and (f) rice paper. All the carbon samples here were obtained by carbonization of the biopolymers at 900 °C in nitrogen environment with a heating rate of 5 °C/min.

2.2.2. Characteristics of WC synthesized from the AMT infiltrated biopolymers

All the biopolymers show a strong and dominant presence of WC as seen in the XRD patterns in Figure 2.3a. No tungsten could be seen in the XRD pattern for any of the sample derived from the biopolymers. However, peaks of W_2C are present in the XRD patterns. As suggested from the XRD patterns, the amount of W_2C formed is around 9% for BC and rice paper. On the contrary, the amount of W_2C in the material derived from CG paper is around 27%. The formation of W_2C is caused by the inefficient diffusion of the carbon atom through the metallic W particles. Such diffusion inefficiency mostly occurs for the metallic W particles sitting on the carbon surface [113]. My hypothesis is the microstructure of the CG paper is responsible for synthesis of the relatively high amount of W_2C than the other two biopolymers. The CG paper is comprised of cellulose fibers with partially or completely open lumen structures. Because of the lumen structures, the fibers in CG paper feature higher surface area. Hence, there are higher chances for more W particle sitting on the carbon surfaces during reduction step of the heat treatment and this results in formation of higher amount of W_2C at a higher temperature. The W_2C can be further carburized to from WC by tuning the heat treatment protocol such as increasing the temperature or using slower heating rate [114]. However, the heat-treated sample retains the fibril structure of its precursor as seen in the FESEM image (Figure 2.3b). Formation of hexagonal WC grains can be seen in the higher magnification images (inset of Figure 2.3b).

Although the composition of the CG paper and BC is cellulose, BC produces 91% WC compared to 73% in case of CG paper as suggested by the XRD pattern. The fibrils in BC features an average diameter of 80.09 ± 16.85 nm, which is significantly smaller than the fiber diameter of the CG paper. Furthermore, the fibrils in BC do not feature a lumen structure. Hence, the fibrils in BC provide less surface area for the W particles for sitting on the carbon surface. Major reactions occur for the W particles which nucleates inside the fibers thanks to the infiltration of AMT in the BC fibers. Furthermore, the crystallinity of the BC derived carbon is higher than the carbon obtained from CG paper, as suggested by the Raman spectroscopy (Figure 2.3c). This higher crystallinity ensures higher reaction rate between the carbon derived from BC and the metallic W particles. These ensure the complete carbothermal reaction to form WC and less formation of W_2C. Figure 2.3c shows the morphology of the WC obtained from the BC. The WC retains the fibril structure of its precursor. The average diameter of the fibers is 177.16 ± 17.11 nm, which is almost 2 times larger than the fibers of precursor BC. We hypothesize that the hydrophilic nature of the BC is responsible for such increase in the diameter. BC is known to be an extremely hydrophilic material. The water retention value for wet BC pellicle is up to 1000% of the actual volume of the BC, whereas air-dried BC pellicle features a water retention value up to 625% [115]. Hence, the water used for the AMT solution swells the BC fibers significantly. However, the amount of swelling of individual fibers in the presence of AMT is still unknown. I hypothesize that during the heat treatment, the nucleation of the crystalline intermediates begins at such swollen conditions. Because of that, the WC obtained through heat treatment features larger diameter than the bacterial cellulose fibers.

The rice paper lost its unique cellular structure and formed a porous structure of the agglomerated WC particles during the formation of WC as seen in Figure 2.3d. The primary constituent of rice paper is starch. Starch is known to form a sol in presence of water through hydration reaction [116]. Due to the formation of the sol, the rice paper loses its unique cellular structure in reaction with water. Hence, here the starting material for WC synthesis is a starch sol infiltrated with AMT solution. The carbide synthesized from an aqueous sol precursor is expected to feature a porous structure of agglomerated grains of carbides [53,74], which agrees to the microstructure of our final product obtained from the heat treatment of AMT infiltrated rice paper. The average grain size of the WC synthesized from the rice paper is estimated to be 38.76 ± 6.27 nm.

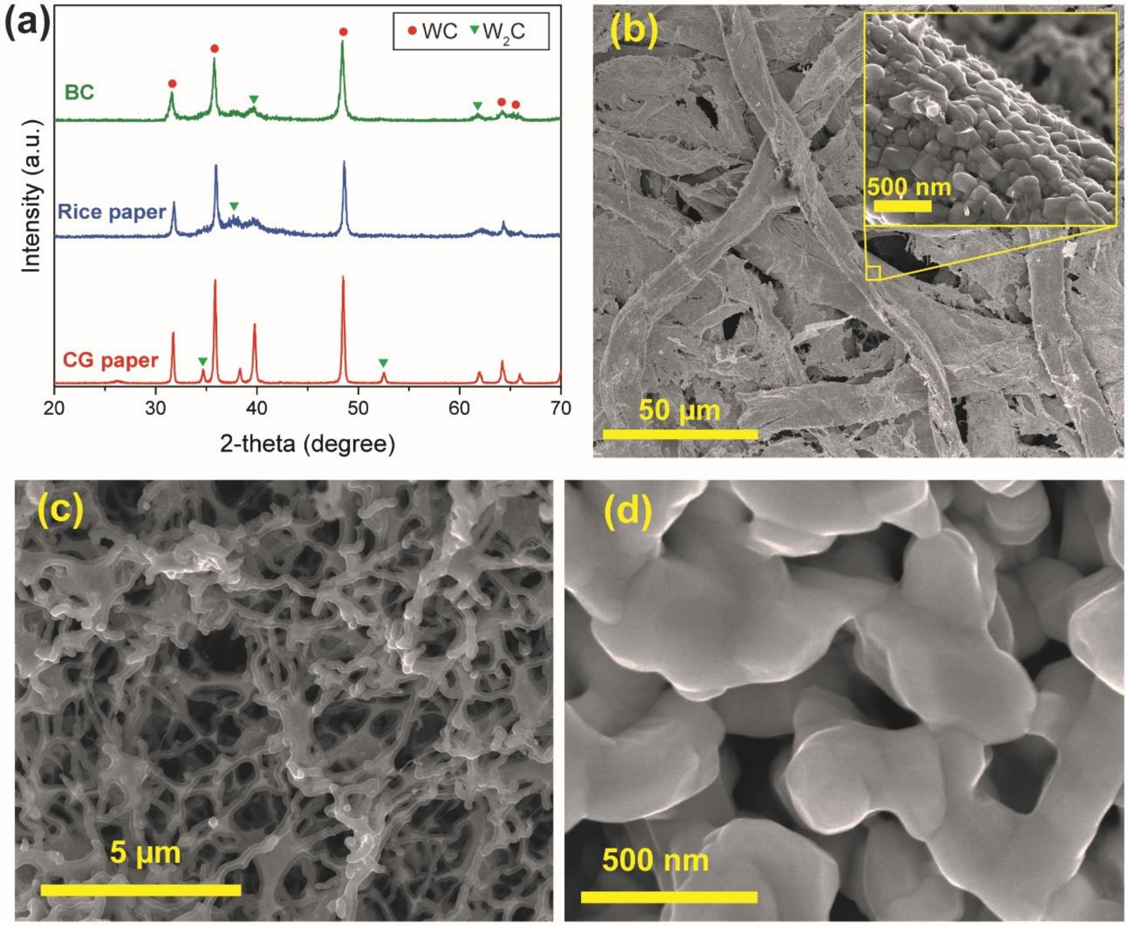

Figure 2.3: (a) XRD pattern of the carbonaceous material obtained by heat treating the biopolymers infiltrated with 20% AMT at 1300 °C with a heating rate of 5 °C/min in Vacuum environment. A strong and dominant presence of WC can be seen in the XRD patterns with a presence of W_2C. No peaks for metallic W are seen in the XRD patterns. FESEM images of the WC obtained from (b) CG paper, (c) BC, and (d) rice paper. WC from both CG paper and BC retains the fibril structure of their biopolymers. The inset of Figure (b) shows the formation of hexagonal WC from the CG paper. WC from rice paper loses the cellular structure and forms a porous agglomeration of particles.

2.2.3. Optimizing WC synthesis from CG paper

Although porous WC were synthesized from all the three fibrous biopolymers, there exists practical challenges with rice paper and bacterial cellulose. The rice paper I used here is commercially available rice paper. Although the main component of rice is starch, Other additives such as protein, vitamin B6, sugar and salt are added in minor amount to the rice starch for commercial grade production of rice paper [85]. Exact composition and quantity of these additives are made unavailable by the manufacturer. These additives generate impurities in the synthesized WC. These impurities may have an impact on the macrostructural properties of the 3D shapes of porous WC, once fabricated using the rice paper. As the composition and quantity of the impurities are unknown, the effect of the impurities will not be possible to characterize. The possible way to determine the impurities is to do elemental analysis of the synthesized WC from rice paper. However, elemental analysis is out of the scope of our facility. Hence, until the exact composition of the rice paper is characterized, it is impractical to advance towards fabrication of the 3D parts of WC using rice paper.

The challenge using bacterial cellulose is production of large sheets of bacterial cellulose. For a successful fabrication of a 3D shape using origami-inspired manufacturing, a relatively large (area ≥ 5 inch × 5 inch) and thick (≥ 10 mm) sheet of bacterial cellulose is required. It requires at least a week to produce such large sheet of bacterial cellulose. The culture media is carefully monitored for contamination during the entire time. Although in our lab we were successful to produce a bacterial cellulose pellicle of 1-inch diameter and a thickness of 5 mm, we have been suffering from contamination in our lab production of large sheets of bacterial cellulose. Once the production of the large sheets of bacterial cellulose will be possible, it will be feasible to fabricate 3D parts of porous WC using the bacterial cellulose.

In comparison to rice paper and bacterial cellulose, CG paper is pure cellulosic paper and uses a well-established paper manufacturing process for commercial production. It is easily available from its manufacturer with compositional and microstructural details. Hence, for practical reasons stated above, only CG paper is chosen for the production of 3D shapes of porous WC in the origami-inspired manufacturing. Hence, I focus on CG paper for further optimization of the synthesis conditions and study the effect of synthesis parameters on the synthesized WC using the design of experiment (DOE).

Nine different samples were prepared according to the L9 orthogonal arrays. The relative amount of WC was calculated from the XRD pattern of each sample and reported in the Table 2.3. The S/N ratio for each experiment is given in Table 2.3 as well.

Table 2.3: Results and signal to noise ratio for the experiments designed using the L9 orthogonal arrays for synthesis of WC from CG paper.

Exp. no	**Temperature (°C)**	**Heating rate (°C/min)**	**AMT (%)**	**Amount of WC (%)**			**S/N**
				Trial 1	Trial 2	Trial 3	
1	1100	1	50	14.47	14.98	15.21	23.45
2	1100	2.5	10	37.35	39.80	37.54	31.64
3	1100	5	20	36.06	18.01	40.33	28.27
4	1200	1	10	56.52	50.42	48.65	34.24
5	1200	2.5	20	59.40	68.58	66.58	36.19
6	1200	5	50	29.91	30.71	26.54	29.21
7	1300	1	20	55.46	63.46	69.81	35.86
8	1300	2.5	50	33.74	26.99	36.55	30
9	1300	5	10	69.53	78.54	75.54	37.41

Table 2.4: ANOVA of the S/N ratios for the relative amount of WC obtained from CG paper

Source	*DF*	*Adj SS*	*Adj MS*	*F-value*	*P-value*	*Mean S/N ratio*		
						Level 1	*Level 2*	*Level 3*
Temperature	2	75.08	37.54	17.61	0.054	27.79	33.21	**34.43**
Heating rate	2	3.16	1.58	0.74	0.574	31.19	**32.61**	31.63
AMT	2	82.99	41.49	19.46	0.049	**34.43**	33.44	27.55
Error	2	4.27	2.13					
Total	8	165.49						

ANOVA was used on the S/N ratios to determine the significance of the synthesis parameters on the results. ANOVA results of the S/N ratio is given in Table 2.4. The F-value indicates the effect of the control factor on the result obtained [117]. An F-value less than 1 indicates minimal effect of the control factor on the result. F-value around 2 represents moderate influence of the control factor on the outcome. An F-value more than 4 suggests strong and significant effect of the control factor. From Table 2.4, it can be observed that heating rate has an F-value of 0.74 suggesting its minimal influence on the synthesis of WC. However, temperature and AMT have strong impact on the WC synthesis with the F-value of 17.61 and 19.46 respectively. Similar results can be observed in Figure 2.4a-c, where the average relative amount of WC obtained from the Taguchi analysis is plotted for each synthesis parameter.

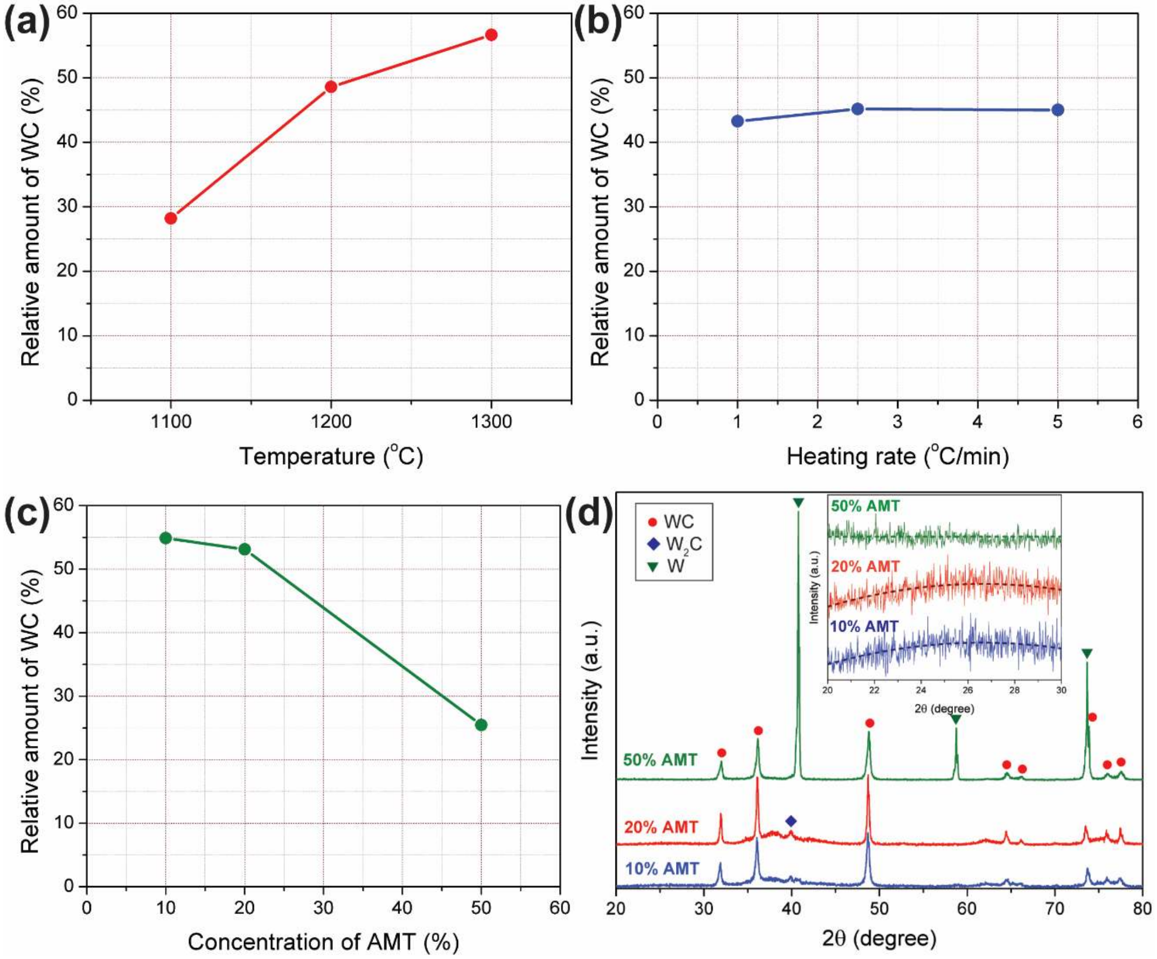

Figure 2.4: Effect of (a) temperature, (b) heating rate and (c) concentration of AMT on the synthesis of WC from CG paper obtained from the design of experiment using Taguchi analysis. This analysis is based on the crystalline phases obtained in the XRD patterns of the heat-treated sample. (d) XRD patterns for the samples obtained using different concentration of AMT. The inset shows the pattern zoomed in the range 2θ = 20° to 2θ = 30°, which is important to investigate the presence of any free carbon the sample. The samples for 10% and 20% exhibit a bulging curve in that range. This indicates a significant amount of free carbon present in both the sample.

The amount of WC increases with increase in the synthesis temperature, which is in agreement with previous literature [53]. The relative amount of WC does not change significantly within the heating rate 1 – 5 °C/min, as previously indicated by the F-value. The relative amount of WC exhibits decreasing trend as the concentration of AMT increases. The mean value of S/N ratio for each control factor is summarized in Table 2.4. The S/N ratio should be highest at the optimum condition, as the signal is desired to be much higher than the noise. The highest value of the S/N ratio for each of the synthesis parameter is indicated in bold characters. Therefore, the optimum conditions according to the design of experiments are the following: synthesis temperature of 1300 °C (level 3), heating rate of 2.5 °C/min (level 2) and AMT concentration of 10% (level 1).

It should be noted here that the relative amount of WC was measured considering only the crystalline material present in the sample. The presence of any free carbon is not considered here. In case of lower concentration of AMT, there is high possibility that significant amount of carbon present in the matrix. Hence, we performed the experiments with the different AMT concentrations at 1300 °C with 2.5 °C/min. The results of the XRD with the different AMT concentrations are shown in Figure 2.4d. The XRD patterns for sample with 10% and 20% AMT looks similar, where WC is the predominant material in the matrix with little amount of W_2C. No peaks for W were seen in either case. In both the samples with 10% and 20% AMT, significant amount of carbon was present as indicated by the bulge between $2\theta= 20°$ to $2\theta= 30°$ in the XRD pattern (Inset of Figure 2.4d). The best fit curve to the bump seems very similar for both the samples, so it cannot be estimated which sample contains more carbon. However, the WC peaks in sample for 20% AMT were relatively sharper than that of 10% AMT. The relative amount of WC is 94% for 20% AMT while compared to 85.39% for 10% AMT. Hence, it can be inferred that in case of 20% AMT, more WC was formed, and more carbon was consumed to form WC. With further increase of the AMT concentration to 50%, the bump for the amorphous carbon in the XRD pattern became flat, which suggests all the carbon was consumed to form WC. However, metallic W became the dominant material in the sample, which is not desired. Integrating the results from DOE and the XRD for different concentrations of AMT, we obtain the optimum conditions for the synthesis of WC from CG paper, which are: synthesis temperature of 1300 °C, heating rate of 2.5 °C/min and AMT concentration of 20%.

2.2.4. The effect of synthesis parameters on the grain size of WC

We used the Taguchi L9 orthogonal array to study the effect of the synthesis parameters on the grain size of the WC. The result of the Taguchi analysis is presented in the Figure 2.5. The grain size increases with the synthesis temperature, which is in agreement with previous reports [118]. The heating rate and the concentration of AMT have minimal influence on the grain size of the WC. This is further confirmed by the ANOVA analysis. The results from ANOVA is presented in Table 2.5 and the percentage of the contribution is shown in Figure 2.5d. The F value for the temperature is 5.94 whereas F values for heating rate and concentration of AMT are 0.77 and 0.59 respectively. Hence, temperature is the main influencing factor for grain size. The range of heating rate is narrow here. Within such narrow range, the effect of the heating rate on grain size is negligible, which is reported by previous authors [119,120]. However, the grain size of the WC is expected to decrease with faster heating rate, because faster heating rate induces high degree of pyrolysis of the precursor materials and allows lesser time for sintering of the particles [121]. However, the average grain size of the WC obtained at the optimum synthesis conditions i.e. at 1300 °C with 2.5 °C/min heating rate and 20% AMT is 58.8 ± 5.82 nm.

Table 2.5: ANOVA analysis for the grain size of WC synthesized from CG paper

Factors	*DF*	*Adj SS*	*Adj MS*	*F- value*	*P- value*	*Percentage of contribution (%)*
Temperature	2	12.95	6.47	5.94	0.144	71.6
Heating rate	2	1.68	0.84	0.77	0.565	9.27
AMT	2	1.28	0.64	0.59	0.630	7.07
Error	2	2.18	1.09			12.06
Total	8	18.09				100

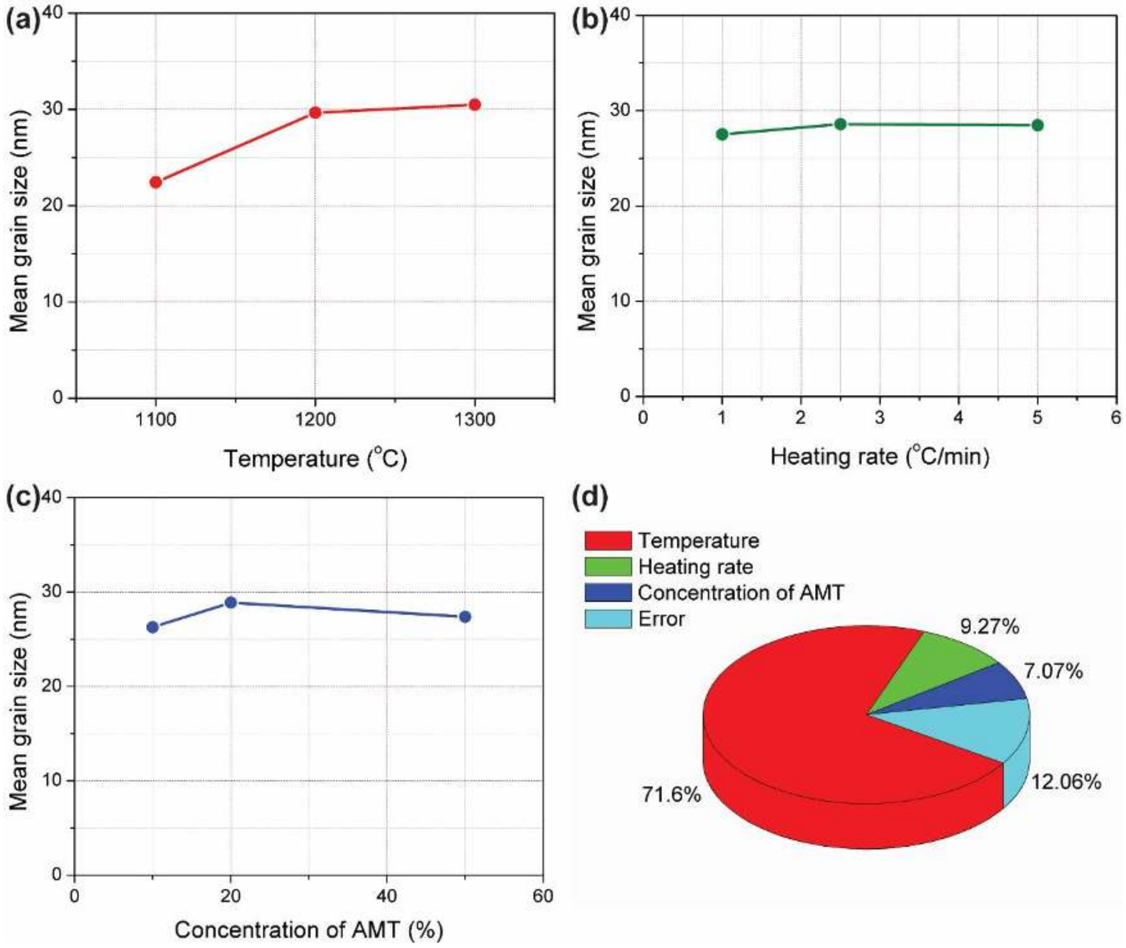

Figure 2.5: Effect of (a) synthesis temperature, (b) heating rate, and (c) concentration of AMT on the mean grain size of WC obtained from the Taguchi analysis. The Taguchi method uses the grain size estimated from the XRD pattern of the heat-treated sample using Scherrer equation. (d) The percentage of contribution of each factor on the grain size of WC obtained from the ANOVA analysis.

2.2.5. Microstructure of the WC obtained from CG paper

The microstructure was characterized for the sample obtained through heat treatment using the optimum synthesis parameter obtained from the DOE i.e. synthesis temperature of 1300 °C, heating rate of 2.5 °C/min and 20% concentration of AMT. The CG paper used in this work was basically a multilayered porous matrix of tightly packed cellulose fibers with an average diameter of 17.48 ± 3.06 µm. However, the electron microscopy revealed that the microstructure of the fibril network on the outer layer of the heat-treated sample is different from that in the inner layer. The average diameter of fibers forming the outer layer is 10.88 ± 2.05 µm, whereas the fibers in the inner layers feature an average diameter of 15.62 ± 1.73 µm. The spacing between fibers is random, which leads to macroporosity of varying dimensions in the range from 1.04 µm to 28.34 µm (Figure 2.6b). Higher magnification FESEM images further show that the fibers on the outer layer are composed of WC grains (Figure 2.7a). The lattice planes with a lattice spacing (d) of 2.5 Å can be observed in the HRTEM image of the outer-layer fibers (Figure 2.7b), which corresponds to (100) plane of hexagonal WC [122]. In contrast, the inner-layer fibers are composed of WC decorated in a carbon matrix as shown in Figure 2.7c. This can be further confirmed by the HRTEM image of the inner-layer fibers as shown in Figure 2.7e. The proportion of WC with respect to carbon in the inner-layer fibers is 2.59 ±0.39 as characterized by EDS analysis (data not shown). Our hypothesis is that the evaporation of water during the drying process after the infiltration of AMT is attributed to the difference in the composition of the inner and outer layer fibers. During the evaporation, some amount of AMT might be carried to the outer layer by the water from the inner layers. Hence, the stoichiometry between the carbon and

W met on the outer layer, whereas the inner layer experienced the W deficit. As a result, WC was formed on the outer layer of the paper and a WC decorated carbon matrix was obtained in the inner-layer fibers. However, further investigation is needed for validation of this hypothesis.

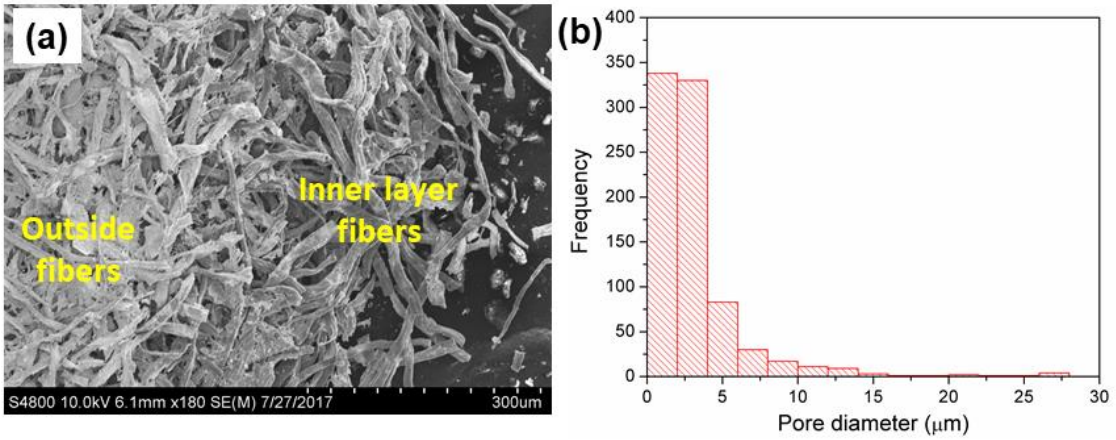

Figure 2.6: (a) FESEM image of the sample obtained from the heat treatment of CG paper using the optimum synthesis condition i.e. synthesis temperature of 1300 °C, heating rate of 2.5 °C/min and AMT concentration of 20%. The WC obtained here features a porous network of randomly oriented fibers. The microstructure of the fibers from outer layer of CG paper differs from the fibers from the inner layer. The fibers which forms the outer layer of the paper are shown as the outside fibers, and the fibers from the inside layers are indicated as the inner layer fibers. (b) The pore size distribution of the fibers showing the range from 1.04 μm to 28.34 μm.

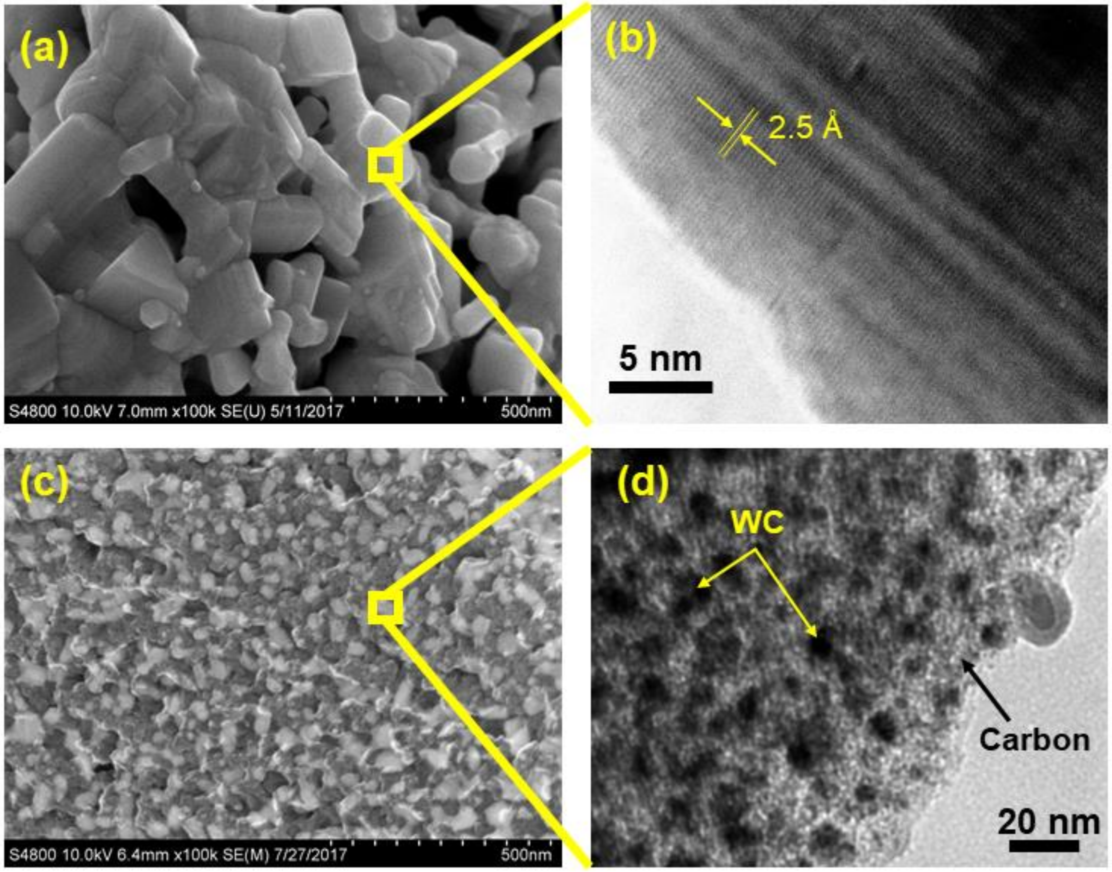

Figure 2.7: (a) Higher magnification FESEM image of the fibers from the outer layer showing the porous network of agglomerated WC particles. (b) HRTEM image of these WC particles shows the lattice planes of WC with a lattice spacing of 2.5 Å. (c) Higher magnification FESEM image of the fibers from the inner layer of the sample showing WC decorated in a carbon matrix. (d) HRTEM image of the inner layer fiber further confirms this phenomenon showing WC particles surrounded by carbon.

2.3. Concluding remarks:

In this chapter, we have presented the synthesis of porous WC materials using fibrous cellulose and starch as the biopolymer precursor. The WC obtained from rice paper loses the stochastic open cell cellular structure of the rice paper derived carbon. The potential solution to retain the cellular structure like the carbon derived from rice paper is infiltrating the carbon structure with the AMT solution instead of infiltrating the rice paper. This will prevent the formation of the starch sol structure and the open cell structure of carbon will minimize the amount of water absorbed by the structure. The bacterial cellulose derived WC retained the fibril network. However, production of a large sheet of bacterial cellulose, which is necessary for the fabrication of origami shapes, is a challenge in our laboratory set up due to the contamination issues. Ongoing work is to monitor the healthy growth of large sheets of the bacterial cellulose in our laboratory set up.

The results obtained from the DOE show that temperature is the most influential synthesis parameter in the synthesis of WC. Heating rate in the range from 1 °C/min to 5 °C/min has shown to be the least impact on the WC synthesis and grain size of WC. The optimum conditions obtained from the results of DOE for synthesis of WC from CG paper are: synthesis temperature of 1300 °C, heating rate of 2.5 °C/min, and 20% AMT concentration. However, the microstructure and the composition of the fibers from the outer layer are different from that from the inner layer. A homogenous microstructure throughout all the layers of the CG paper can be obtained if water can be replaced by some other solvent featuring weaker intermolecular bond strength. Other possible solution is freeze drying the

AMT infiltrated CG paper in liquid nitrogen to replace the AMT. Ongoing work is on obtainment of a homogenous WC material from CG paper using the proposed possible solutions.

Our goal is to fabricate 3D complex shapes of porous carbide materials using origami-inspired manufacturing using these fibrous biopolymers. Hence, based on the current results from the biopolymers used here, we continue our further work on shaping the porous WC using origami of CG paper. The fabrication of 3D complex shapes in the origami-inspired manufacturing using the CG paper are detailed in the Chapter 4. The methodology used for CG paper for synthesis as well as fabrication of 3D shapes could be applied to BC and rice paper in future, when the practical challenges corresponding to the rice paper and bacterial cellulose are resolved. When the fabrication of the 3D shapes using each of the biopolymers will be feasible, the choice of the biopolymer for manufacturing of the 3D shapes will depend on the desired application. This choice will mostly rely on the microstructure of the porous WC derived from the biopolymers. For example, the bacterial cellulose derived WC features smaller open pores within the fibril network when compared to the WC derived from CG paper. Hence, bacterial cellulose derived WC can be used for a filter application where filtration of finer particulates is necessary.

CHAPTER 3: Carbide synthesis from biopolymer gel composite

The second fabrication method I choose in my dissertation for the fabrication of the 3D shapes is additive manufacturing. The additive manufacturing relies on layer-by-layer deposition of a material. A gel-based material is a suitable candidate for such layer-by-layer deposition due to its bingham plastic nature. To obtain a gel-based material, we choose carrageenan and chitin as the gel forming biopolymers. Carrageenan is basically extracted from red seaweeds and widely used as a gelling agent in food processing, pharmaceutical and cosmetic industry [46]. Chitin is derived from the hard shells of different marine animals including shrimp, lobster and crabs, and is widely used in food processing, pharmaceutical, cosmetics and textile industries [123]. I seek to enable the gel obtained from carrageenan and chitin to produce 3D parts of porous WC in the additive manufacturing platform. Hence, it is important to first optimize the conditions for synthesis of the porous WC from the biopolymer gel.

In this chapter, I study how the precursor composition and heat treatment of a composite of carrageenan, chitin and tungsten oxide nanoparticles must be tailored to yield a porous WC. In this study, I first address the impact of the precursor composition and heating parameters on the properties of the final material towards minimizing the energy and time required for processing. I characterize the synthesized WC in terms of its grain size and porosity. The synthesis conditions optimized here will be further used during the fabrication of a 3D shape of porous WC using the additive manufacturing platform. The study presented in this Chapter is published in Ceramics International, a peer reviewed journal [53]. I use the published article as the Chapter detailed as following.

3.1. Experimental Section

3.1.1. Materials

Iota-carrageenan (IC) (catalog number: C1138) and chitin from shrimp shells (catalog number: C9213) were purchased from Sigma Aldrich, USA. High purity tungsten oxide (WO_3) nanoparticles featuring 23-65 nm diameter were purchased from US Research Nanomaterials, Inc (catalog number: US3540). All materials were used as received. Ultra-pure water was used for the preparation of the polymer composite.

3.1.2. Experimental Method

Dried powders of IC and chitin were manually mixed in a weight ratio of 1:4 to ensure intermolecular binding of IC and chitin [124]. WO_3 nanoparticles were then added to the powder mix to obtain a WO_3:C ratio of 1:6, and vortexed for 10 minutes (Thermo Scientific, Maximix M16710-33Q). Although a ratio of 1:4 WO_3:C is theoretically required [125], other authors have reported the need for a 1:6 ratio to ensure the occurrence of a carbothermal reduction reaction [114]. The exact amount of WO_3 to be added to the biopolymer mix was deducted based on the carbon yield from such mix detailed in the results section below. Once the biopolymers and WO_3 were appropriately mixed, 5 g of this powder mixture were then added to 15 ml of ultra-pure water and manually mixed using a spatula. The resultant material resembles a gel and will be referred to as the biopolymer gel composite (BGC).

The BGC was heat treated at different temperatures ranging from 750 °C to 1450° C in an alumina tube furnace (TF1400 or TF1700, Across International, USA) under a constant nitrogen gas flow rate of 10 SCFH (Standard Cubic Feet per Hour). The heating protocol consisted of 5 steps: (a) from room temperature to 300 °C with a heating ramp of 5 °C/min; (b) a dwell at 300 °C for 30 minutes to eliminate the excess oxygen from the furnace tube; (c) from 300 °C to final temperature with 5 °C/min temperature ramp; (d) dwell at the final temperature and finally (e) natural cooling to room temperature by turning off the furnace. The temperature and dwell duration of the final step (d) were parameters of study.

3.1.3. Characterization

Thermogravimetric analysis (TGA) was performed for the IC-chitin biopolymer complex without the nanoparticles at 1000 °C under nitrogen gas flow with a heating rate of 5 °C/min to investigate the carbon yield of such mixture. The crystallinity and composition of the carbonaceous materials obtained after heat treatment were characterized by X-ray diffraction (XRD) spectroscopy using Cu-Kα radiation (Rigaku Ultima IV, Japan). Material correlation was performed using International Centre for Diffraction Database (ICDD). The morphology and elemental analysis of the carbonaceous materials were characterized using field-emission scanning electron microscopy (Hitachi SU6600, Japan) and energy dispersed X-ray spectroscopy (EDX, Oxford Instruments, USA) mounted on the SEM. High Resolution Transmission Electron Microscopy (HRTEM) analysis was performed using a H9500 (Hitachi, Japan) electron microscope with an acceleration voltage of 200 kV. Sample preparation for the TEM was performed using a Focused ion beam (FIB) milling machine (NB5000, Hitachi, Japan). Nitrogen adsorption-desorption was performed for the pore size distribution using Quantachrome Autosorb iQ gas sorption analyser (Quantachorme Instruments, USA). Brunauer–Emmett–Teller (BET) method was used for measuring the specific surface area of the resultant materials.

3.2. Results and Discussion

3.2.1. Carbon yield of water-based IC-chitin composite

The first step was to characterize the carbon yield of the water-based IC-chitin composite in order to determine the correct amount of WO_3 particles to add to the biopolymer mix to achieve a ratio WO_3:C of 1:6 and a stoichiometric reaction during heat treatment. As illustrated in Figure 3.1, the carbon yield of this pure biopolymer composite was 7.7% when accounting for water evaporation. Around 60% weight loss is observed within the temperature of 100 °C which is attributed to water evaporation. A significant weight loss is observed in the temperature range 200 °C – 400 °C, which is attributed to the escape of volatile products caused by thermal degradation of the biopolymers [126,127]. As the temperature increases, further gradual weight loss is observed due to the elimination of heteroatoms such as hydrogen, nitrogen and oxygen from the carbonaceous material [128]. The biopolymers yield to a carbonaceous material having more than 90% carbon at 1000 °C which is in agreement with previous reports [128–130]. Other elements in the material are nitrogen, oxygen and hydrogen [128,130,131]. It is important to note that the carbon yield reported above is when analyzing the water-based gel-like material. If only the weight of the biopolymers is considered without the amount of water in the precursor gel, the carbon yield is 30.8% which is much higher than the carbon yield of iota-carrageenan and chitin by themselves [132,133]. Our hypothesis is that the strong intermolecular binding of iota-carrageenan and chitin prevents the release of the carbon atoms to some extent during the thermal degradation, which results in the higher carbon yield of the gel complex. However, extensive study is needed to understand the thermal degradation process of such biopolymer composite.

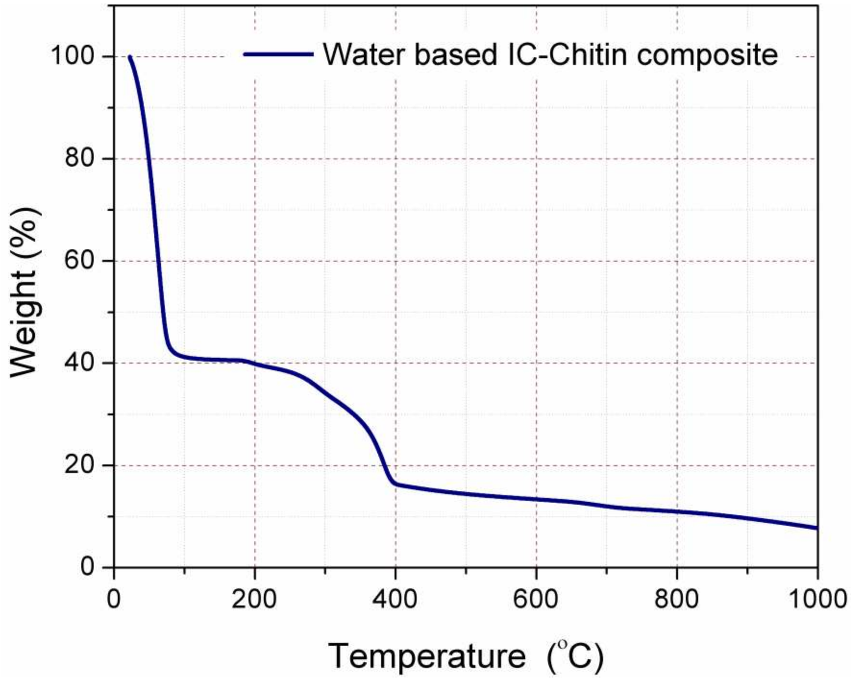

Figure 3.1: TGA result when heating the water-based IC-chitin composite up to 1000 °C in nitrogen with a heating rate of 5 °C/min. Note how a significant weight loss occurs within 100 °C due to the evaporation of the water. Another significant weight loss can be observed in the temperature range 200 °C – 400 °C, due to the escape of the volatile products during thermal decomposition of the biopolymers.

3.2.2. Effect of Temperature on Tungsten carbide synthesis

The XRD patterns of the carbonaceous materials obtained from the heat treatment of the BGC (the gel-like, water-based composite of IC, chitin and WO_3 particles) at different temperatures are shown in Figure 3.2a. Major peaks are identified at the 2θ angles of 31.7, 35.9, 48.6, 64.4 and 66.1 which are indexed to (001), (100), (101), (110) and (002) crystal planes of hexagonal tungsten carbide (WC) respectively (ICDD PDF number 01-072-0097). The other peaks in the XRD patterns correspond to tungsten hemicarbide (W_2C) and tungsten (W) as matched to the ICDD PDF numbers 01-071-6322 and 00-001-1204 respectively. No presence of carbide was observed in XRD patterns for 750 °C and 900 °C. At 750 °C, the peaks in the diffraction pattern correspond to WO_3 and $W_{18}O_{49}$ which infers that WO_3 is partially reduced to its metastable oxide $W_{18}O_{49}$. At this state, the nanoparticles are expected to be surrounded by amorphous carbon that resulted from the carbonization of the biopolymers at temperatures of 350 °C – 600 °C. WO_3 and $W_{18}O_{49}$ are completely reduced by the surrounding carbon material to metallic tungsten at 900 °C. At 960 °C, the presence of a small amount of WC along with its hemicarbide form W_2C is observed, although metallic tungsten is the dominant material present in the sample as indicated by the XRD pattern. This indicates the synthesis reaction of WC started in the temperature range between 900 °C- 960 °C. The intensity of the peaks for WC increases proportional to the temperature, whereas the peak intensity of W decreases. Increasing the temperature further results in the disappearance of metallic tungsten as observed in the XRD pattern for 1300 °C and 1450 °C. The presence of W_2C hemicarbide phase also decreases with the increase in temperature as observed by the diminishing peaks at temperatures 960 °C – 1450 °C.

To better visualize and estimate the relative proportion of WC, W_2C and W phases in the material, I_n/I_{total} was plotted against the reaction temperature as shown in Figure 3.2b. Here I_n is the sum of the peak intensities corresponding to a particular phase, WC for example, and I_{total} is the sum of all the peak intensities present in the XRD pattern. The formation of

WC clearly improves with the increase in reaction temperature, whereas the relative proportions of W_2C and W is lowered. An increase of the reaction temperature enhances the carburization reaction of W to form WC along with the phase transformation from W_2C to WC. At 1300 °C, the relative amount of metallic tungsten decreases down to zero which indicates complete carburization of W. A small amount of W_2C is still present in both of the samples for 1300 °C and 1450 °C. However, the amount of W_2C is less for the sample of 1450 °C with comparison to 1300 °C and the amount of WC is proportionately higher in the sample of 1450 °C than that of 1300 °C. We assume that at higher temperature further carburization of W_2C into WC phase will take place and WC will be the sole material present in the sample [134]. Hence, metallic tungsten disappears from the material at 1300 °C and WC of 98.2% purity is obtained, with W_2C as the other material in the matrix. A WC purity of 99% is obtained when heating at 1450 °C. This is significant because when compared to current synthesis techniques, the temperature required is up to 1800 °C to obtain a carbide with up to 99% purity [135].

The presented XRD analysis is in good agreement with the theory of WC formation from solid-solid reaction between WO_3 and carbon [56]. From the TGA results in Figure 3.1, it is evident that the IC-chitin biopolymer complex decomposes to a carbon rich material in the temperature range 350 °C – 600 °C. This carbon excess causes a reduction of the WO_3 nanoparticles to metallic W [57,136]. During such reduction, WO_3 transforms into several other oxide forms such as WO_{3-x} and WO_2. The oxygen molecules present in these oxides react with the surrounding carbon to form carbon monoxide (CO) and carbon dioxide (CO_2) [134]. Once the reduction process is complete and the temperature is further increased above 900 °C, tungsten reacts with the surrounding carbon to form WC. During this carburization process, tungsten hemicarbide (W_2C) is also formed likely due to the carbon deficiency in the reaction [56]. W_2C can be further carburized to WC at higher temperature in presence of carbon [114].

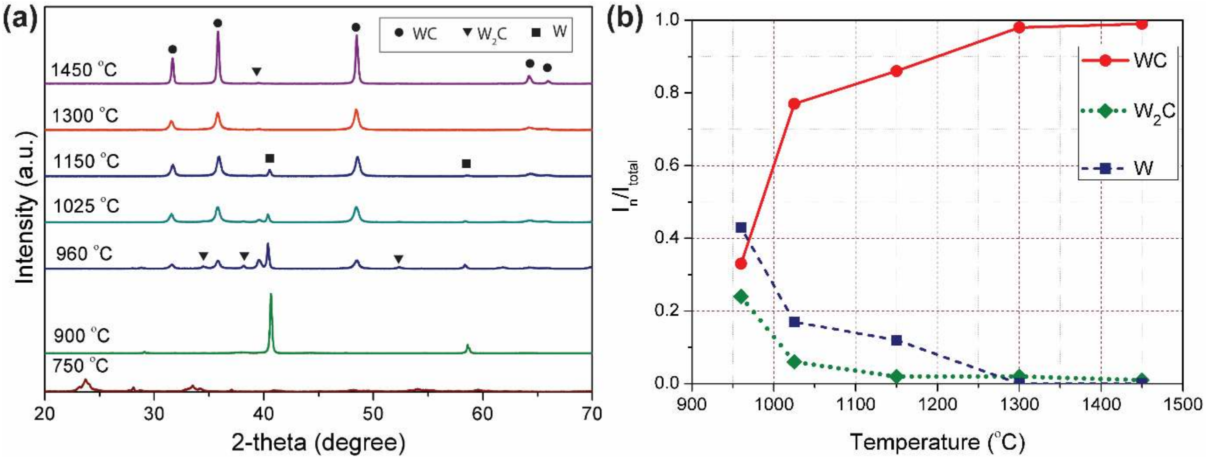

Figure 3.2: (a) Illustrative example of the XRD patterns of carbonaceous materials obtained from heat treatment of the PCP composite at different temperatures in nitrogen for 3 hours. At least 3 independent experiments were performed for each temperature and reproducible results were obtained; (b) plot of I_n/I_{total} against the reaction temperature. Note the obtainment of a 98.2% pure WC at temperature of 1300 °C and further increase in purity to 99% as the temperature increases to 1450 °C.

3.2.3. Effect of Dwell Time on tungsten carbide synthesis:

The impact of dwell time at the final temperature of 1300 °C is illustrated in Figure 3.3 using the obtained XRD patterns and the proportion of W, WC and W_2C in the samples. Dwell time of zero represents the incidence when the furnace is immediately turned off when the furnace temperature reached 1300 °C. Under this condition, a strong presence of WC can be observed with a small amount of W_2C in the sample. A significant amount of metallic tungsten is also present in the sample along with a small amount of metastable phase of tungsten oxide (W_5O_{14}). This indicates the incomplete reduction of WO_3 to W. As the dwell time increases to 15 minutes, tungsten oxide is eliminated, and the intensity of the metallic tungsten is decreased in a significant amount. metallic W can be eliminated from the material when the dwell time is of 3 hours. The use of longer dwell times only yields incremental improvements to the purity of WC in the material, from 98.2% at 3 hours to 99% at 9 hours. Our hypothesis is that major carburization reactions between the precursors completed in 3 hours after reaching 1300 °C and at that point there was almost no material available for reaction in the sample. Furthermore, the energy available for reaction remained constant, as the temperature did not increase. Hence, no significant improvement in the proportional quantity of WC was observed after 3 hours. Hence, a dwell time more than 3 hours does not seem to be necessary. This is beneficial because a shorter dwell time is enough to obtain a material with small grain size, high porosity and high specific surface area as characterized in the later sections.

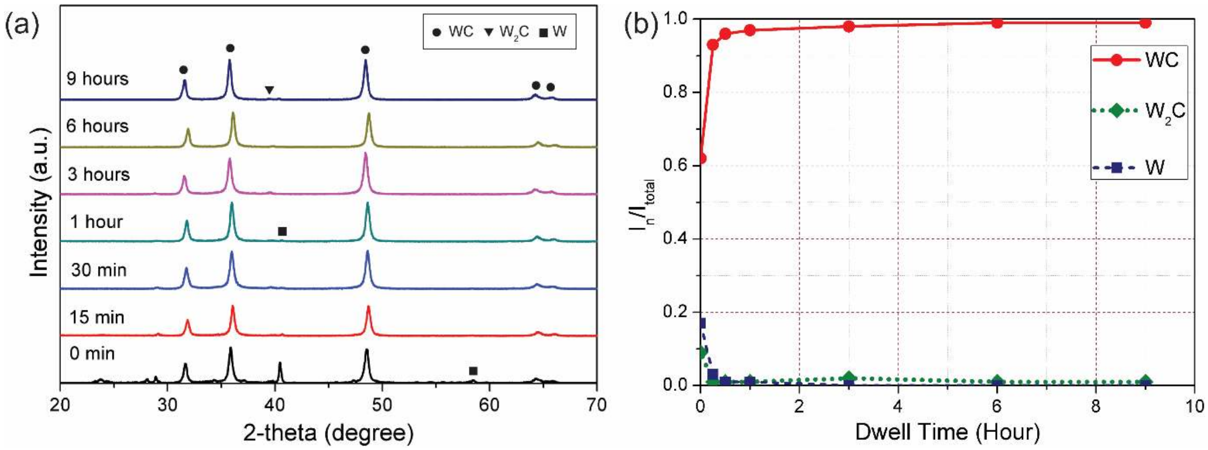

Figure 3.3: (a) XRD pattern of carbonaceous material obtained from heat treatment of IC-Chitin-WO_3 composite at 1300 °C in nitrogen for different dwell time; (b) Plot of I_n/I_{total} versus dwell time. Note that a pure tungsten carbide can be obtained at the dwell time of 3 hours.

3.2.4. Microstructure characterization:

Electron microscopy was used to characterize the grain size obtained in the sample heat treated at 1300 °C for 3 hours, as a highly pure carbide material can be synthesized at this condition. As shown in Figure 3.4a obtained using FESEM, the microstructure is characterized by particle agglomerates and a porous nature. The size of agglomerates ranges from tens of nanometers to 800 nm. Further analysis using HRTEM resulted in the characterization of the carbide particle size in the order of tens of nanometers (Figure 3.4b). The nature of the sample was confirmed to be tungsten carbide by visualizing the lattice fringes shown in Figure 3.4c, featuring a d-spacing of 0.25 nm that is attributed to the (100) plane of hexagonal tungsten carbide; and by electron diffraction (Figure 3.4c inset), which matches with the WC lattice z-plane of [001].

Based on the results using electron microscopy, the grain size of the tungsten carbide was estimated from the XRD patterns using the Scherrer equation (See Equation 2.1). Using such equation, the estimated grain size is plotted for different temperatures and dwell times in Figure 3.5a and b respectively. The grain size of tungsten carbide increases from 17.5 nm at 960 °C to 43.3 nm at 1450 °C. This supports the findings of previous authors on the fact that grain size increases with increasing temperature [118]. In contrast, there is almost no change in grain size with the increase in the dwell time. At 1300 °C, the grain size remains constant at around 20 nm for different dwell time. Hence, this indicates that temperature is a more critical parameter to control to obtain small grain sizes. Small grain size yields better mechanical strength [137], which is essential for applications such as structural components. Small grain size also yields higher surface area, which is characterized here in later section.

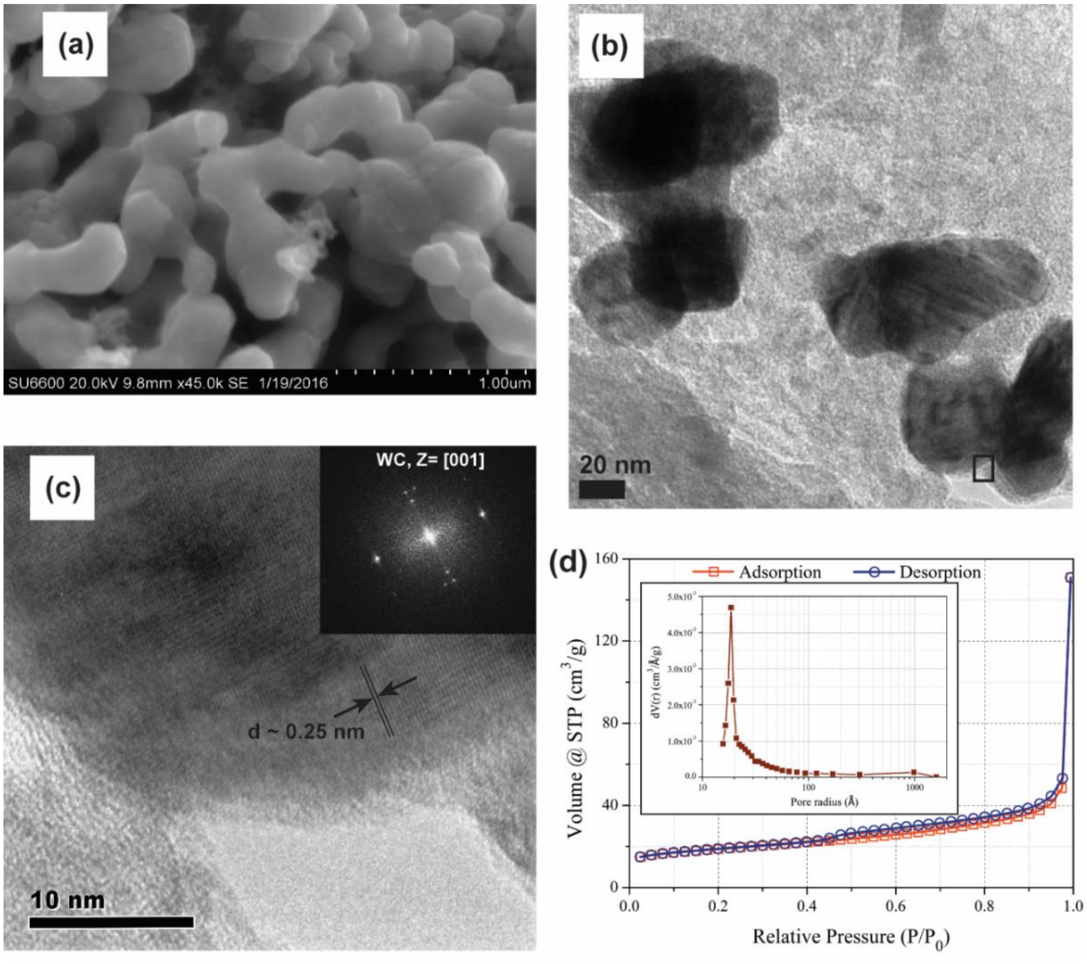

Figure 3.4: (a) SEM image of the synthesize tungsten carbide showing agglomerates of the particles. (b) HRTEM image of the tungsten carbide; (c) HRTEM image of WC image showing the lattice fringes and electron diffraction pattern at the inset. (d) Nitrogen adsorption desorption isotherm of the tungsten carbide and the pore size distribution in the inset. The tungsten carbide was synthesized by heat treatment at 1300 °C for 3 hours using the heat rate of 5 °C/min.

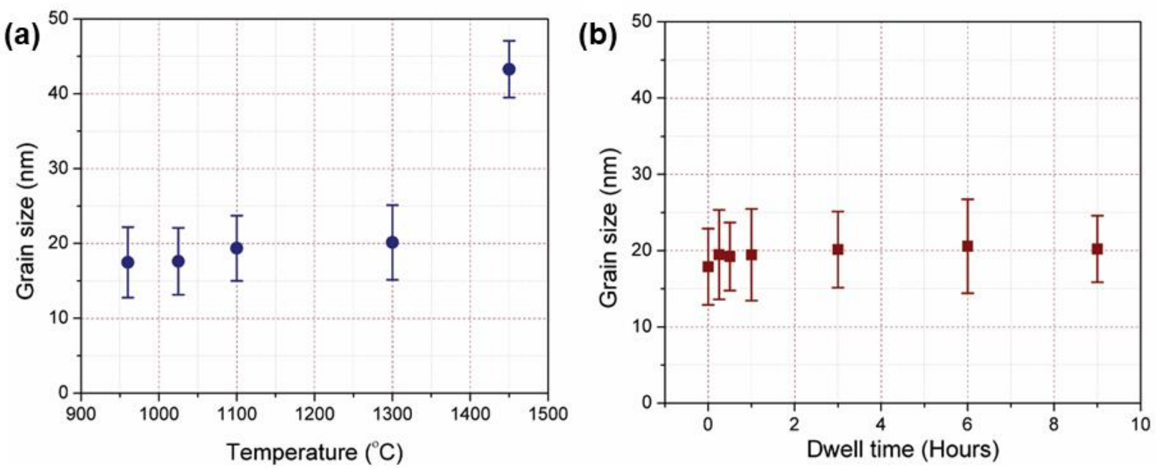

Figure 3.5: Grain size of tungsten carbide (a) at different temperatures and (b) for different dwell time at 1300 °C. The grain size was calculated from the XRD data using Scherrer formula. Note that the grain size increases with the synthesis temperature, whereas there is no effect of the dwell time on the grain size.

The nitrogen adsorption desorption isotherm is shown in Figure 3.4d. The isotherm is of type II and hysteresis of H3 type which confirms the formation of particle agglomerates and open pores. The steep slope in high relative pressures ($P/P_0 > 0.8$) also suggests the presence of macropores (pore diameter > 50 nm) in the material. Although the pore size ranges from 2 nm to 100 nm, most of the pores present in the material are mesopores (pore diameter = 2 – 50 nm) as seen in pore size distribution (inset of Figure 3.4d). The total pore volume in the material was measured to be 0.9 cm^3/g. Our hypothesis is that the evaporation of water in the early stage of heat treatment causes the large pores, whereas the escape of gaseous material during carbothermal reduction reaction leads to the formation of the mesopores in the material. The BET surface area of the tungsten carbide was measured to be 67.03 m^2/g.

3.2.5. Advantages and Disadvantages

3.2.5.1. Renewable resources

The biopolymers used here as carbon precursors are inexpensive and renewable resources. Iota-carrageenan is extracted from red algae and widely used in the food industry as a food thickener. Although the market price varies, carrageenan (CAS 9062-07-1) is significantly less expensive (USD$0.5/g vs. $16.45/g as retrieved from Sigma Aldrich 12/7/2016) than mesoporous carbon (CAS 1333-86-4) used in the carbide industry. *Eucheuma* and *Kappaphycus* are two well-known species for the production of iota-carrageenan. The global production of these algae is around 20 million wet tons among which around 9 million tons are cultivated in developing countries [46]. The countries with major contribution to the production of carrageenan includes Indonesia, the Philippines, the United Republic of Tanzania, and Malaysia. In these countries, the cultivation of seaweed has a positive socio-economic impact because of short production cycles, low capital cost and simple farming technology that can be conducted by various members of a family. Indeed, seaweed farming has become a source of income in coastal areas that had no economic prospects before [138].

Chitin is the second most abundant biopolymer in nature, preceded only by cellulose. The annual turnover of chitin is estimated to be 10^{10}-10^{11} tons [139]. The major source of industrial chitin is the exoskeleton of shellfish disposed as waste by the shrimp, lobster and crab industries [140]. According to the United Nations' Food and Agriculture Organization, the world annual production of shrimp alone is around 9.6 million tons, including extraction from the seas and grown in farms [141]. In terms of human consumption of shrimp, around 40% – 50% of the total mass turns out to be waste material [142]. Extensive research to enable the use of the otherwise wasteful shells into a useful commodity is ongoing around the world [142,143]. Powdered chitin from shrimp shells (CAS 1398-61-4) can be purchased at USD$0.59/g.

A disadvantage about the use of carrageenan and chitin is the fact that their extraction from their source involves alkali or acidic wash. For example, dried seaweed is boiled and washed in hot alkali to eliminate the sulphate groups and the minerals from the seaweed [144] and increase the quality of carrageenan. The production of chitin from shrimp shells includes alkali treatment by 4% NaOH for deproteinisation and acidic treatment by 4% HCl for demineralization [145]. Several studies are ongoing to find alternatives to the chemical extraction method. For carrageenan extraction, the microwave heating method reduces the use of alkali in a significant amount [146]; while for extraction of chitin, few biotechnological methods have been developed where bacterial fermentation has been employed for deproteinisation and demineralization [142,147]. It is also important to note that the amount of carrageenan and chitin is much higher than the carbon black required for the synthesis of an equivalent amount of carbide. Despite this, the production of chitin and carrageenan demands far less energy than oil extraction and subsequent derivation of carbon black. Furthermore, the price of oil is volatile and dependent on several variables which are hard to predict. Although the price of renewable carrageenan and chitin also depend on the market, their price has been more constant and their supply stable.

3.2.5.2. Synthesis temperature

The traditional tungsten carbide synthesis methods can be categorized in three categories: high temperature direct carburization, carbothermal reduction reaction and carburization by gaseous hydrocarbon. The high temperature carburization involves fusion of tungsten and carbon around 2800 °C in hydrogen atmosphere [148]. Both carbothermal reduction reaction and carburization by gaseous hydrocarbon include the carburization of tungsten by carbon in a temperature range 1400 °C – 1800 °C [149]. All of these traditional processes use temperatures in excess of 1400 °C for the synthesis of tungsten carbide. Here, we have demonstrated the synthesis of >98% pure tungsten carbide at temperatures as low as 1300 °C. Lower synthesis temperature implies lower energy required in the process, which together with the choice of precursors makes our process more energy efficient than the traditional methods.

3.2.5.3. Porosity

The tungsten carbide synthesized here is mostly mesoporous and features a BET surface area of 67.03 m^2/g which is higher than the surface area of commercial grade tungsten carbide (BET < 10 m^2/g) synthesized using carbon black and tungsten precursors [95]. We expect the porosity of the matrix to change depending on the composition of the precursor, mixing protocols and heating ramp during treatment. Ongoing work is on understanding the specific impact of these processing parameters on the WC. Nevertheless, materials having high specific surface area and porosity similar to the tungsten carbide presented here have been used as catalytic materials [150] and for sensor applications [151]. Other applications include energy absorbers and high temperature filters. Although tungsten carbide with higher porosity and surface area (BET > 100 m^2/g) can be synthesized using the template method [152], where a sacrificial material in the matrix is disolved, removal of the template generally requires washing with highly corrosive agents such as hydrofluoric acid. The precautions taken to enable processing with such agents, together with the cost of highly selective sacrificial materials, significantly increase processing costs. Hence, further investigation into the process presented here can lead to materials with high surface area which are derived using renewable materials and a less expensive, less dangerous and more environmental-friendly process.

3.3. Conclusion

In this chapter, we have presented a sustainable and environment-friendly method for tungsten carbide synthesis from a biopolymer gel composite. The renewable biopolymer-complex was used here as the carbon source, which eliminates the use of petroleum-based carbon precursors. Porous tungsten carbide was synthesized by heat-treating the BGC at 1300 °C for 3 hours, which is lower than the temperature used in traditional methods of tungsten carbide synthesis. Grain size of the tungsten carbide at this condition was estimated to be around 20 nm. Such small grain size is expected to yield high mechanical strength of the material. The tungsten carbide obtained here is mostly mesoporous, although few macro-pores were present in the material. The BET surface area was measured to be 67.03 m^2/g. Such small grain size, porosity and surface area are preferable for potential catalysts, fuel cell, structural filters and battery applications.

As stated earlier, the goal to use a gel composite for the synthesis of porous WC is to implement an additive manufacturing platform to fabricate 3D shapes of porous WC. The fabrication of 3D shapes of porous WC using the synthesis process presented here is detailed in the Chapter 5.

CHAPTER 4: Origami-inspired manufacturing

As discussed in the Introduction chapter, one of the manufacturing technique I use here to shape the porous carbides is origami-inspired manufacturing. Origami is an ancient art of paper folding, where 3D complex architecture can be fabricated from a flat piece of paper by folding the paper along prescribed creases [28,29,27]. Traditionally, the original purpose of origami is for recreational and artistic purpose [30]. However, in the last four decades, origami has gained significant scientific and technological interest among the scientific community due to its potential to fabricate numerous intricate architectural shapes of engineering value. Utilizing the deformability and compactness of the folded structures, origami has been employed to a wide range of applications including deployable structures for space exploration [153,154], solar cells [155], batteries and capacitors [156,157], biomedical devices [158,159], and energy absorption systems [160]. However, origami folding has so far been limited to the use of paper and soft polymeric sheets [161]. There is no manufacturing technology to fabricate origami-inspired structures of resilient engineering materials e.g. metals and ceramics. Sheet metals and composites are relatively thick and stiff and can be bent into very simple patterns with limited property programming potentials. Hence, there is the need for a manufacturing technique that can enable the versatile origami shaping of the engineering materials.

In this chapter, we address a novel method to demonstrate the use of origami technique to fabricate 3D complex shapes of WC material. To fabricate the origami shapes, I use the pure cellulosic chromatography paper (CG) as the biopolymer precursor due to the reasons detailed in the Chapter 2. Before fabrication of the origami shapes of WC using the CG paper, it is important to study the fabrication of carbonized paper first to understand the structural geometry under heat treatment conditions. Furthermore, carbonized cellulose paper has been shown to be an excellent material for different electrochemical applications such sensors and batteries [162–164]. Therefore, in this chapter we first demonstrate the fabrication of carbon origami structures using the CG paper. Later in the second part of the chapter, we continue discussion for the origami-inspired manufacturing with fabrication of WC origami structures using the synthesis conditions discussed in Chapter 2.

SECTION 4.1: Origami-inspired manufacturing of fibrous carbon shapes

In this work, we present the characterization of the carbon microstructure resulting from carbonizing paper and a discussion of its effect on the mechanical properties of the origami structure. Although we present results using a specific kind of cellulosic chromatography paper, there is an immense potential to tailor the mechanical properties of carbon origami by tailoring the microstructure of the precursor paper. We also address the effect of carbonization on the cellulose fibers and on the origami structure in terms of structural shrinkage. We finish by showcasing the versatility of this technique to make different origami structures of different sizes. The use of origami-based techniques to manufacture carbon cellular materials has excellent scalability prospects. Due to the maturity of the paper making industry, it is possible to produce relatively inexpensive, pure cellulose paper rolls. These could be creased and folded after optimizing continuous embossing and folding techniques, such as those used in the manufacturing of paper bags and paper filters. Continuous heat treatment of the folded shapes can be implemented using belt conveyor or pusher tunnel furnaces, common in the production of tile and other ceramic pieces.

The work presented in this Section is published in Carbon, a peer reviewed international journal [105]. The published article is used as the section for the carbon origami.

4.1.1. Experimental section

4.1.1.1. Fabrication of carbon origami

The fabrication process consisted of four steps illustrated in Figure 4.1: 1) design of crease pattern, 2) automatic pre-creasing, 3) manual folding and 4) carbonization. Pure cellulose chromatography papers Fisherbrand Chromatography Paper, Cat. No. 05-714-1 with thickness of 0.19 mm or Whatman 3MM Chromatography paper, Cat. No. 3030-6158 with a thickness of 0.34 mm were used for this work. Although we can fabricate different origami patterns, we focused our study on Miura-ori, a pattern that belongs to the family of rigid origami. In this case, the facets are considered as rigid panels and creases are considered as hinges [165,166]. The geometry of Miura-ori resembles a herringbone pattern and consists a series of convex “mountains” and concave “valleys”. This origami tessellation has gained much attention among the engineering communities because of its simplicity and mechanical properties such as high specific stiffness [36,167], impact energy absorption [168,169], and negative Poisson’s ratio [170,171]. The Miura-ori pattern has been employed in different applications including packaging of solar panels for space mission [172] and deformable energy storage devices [156]. The pattern can be also found in nature in different forms such as leaves [173,174], embryonic intestines [175] and insect wings [176].

4.1.1.1.1. Design of crease patterns

Fig. 1a shows the crease pattern for a unit cell of a Miura-ori fold. The dotted and solid lines in the unit cell represent the creases to create “valleys” on one side of the paper and “mountains” on the other. The Miura-ori design used here featured 16 unit cells. A unit cell can be defined by the design parameters h, l and α [166]. All the Miura-ori samples fabricated here featured an α of 75° and a 3:5 ratio between h and l. Such specific ratio resulted from fitting 16 unit cells in a square. We only varied the value of h from 3.1 mm (1/8 in) to 15.3 mm (5/8 in) as the size of the pieces increased from 1 inch × 1 inch to 5 inch × 5 inch.

Although the focus of this paper was the Miura-ori structure, other origami structures were studied to assess scalability and complexity of the process. We characterized the Waterbomb base and Yoshimura origami structures. These designs also featured 16 unit cells. The Waterbomb base unit cell was defined by the design parameter s. The Yoshimura unit cell was defined by the design parameters x and y (Figure 4.7b and 4.7c).

Individual crease patterns for “valleys” and “mountains” for all origami structures were designed using Solidworks (Dassault Systems, Waltham, MA, USA). Examples of valleys and mountains for Miura-ori are shown in Figure 4.1b and c respectively. These design files enabled the automatic pre-creasing detailed in the next section.

4.1.1.1.2. Automatic pre-creasing

We used a modified desktop cutting-plotter machine (Graphtec CE6000-40, Japan) to automatically pre-crease the paper and facilitate folding. We replaced the cutting blade with an empty, generic ballpoint pen with a ball diameter of 1.5 mm. Parameters of interest during pre-creasing included speed of movement, acceleration, number of passes and pressing force of the pen. We defined a speed of 12 cm/s, acceleration of 0.71 m/s^2, a force of 2.16 N, and three passes as the ideal parameters to achieve the targeted creasing that will facilitate folding of the origami tessellation. An example of the pre-creased paper for Miura-ori in such process is shown in Figure 4.1d. Alignment of valleys and mountains was implemented using marks that were automatically generated by the software of the cutting plotter and printed on the paper. Pre-creased samples with any visible misalignment were discarded.

4.1.1.1.3. Manual folding

Following Miura-ori techniques, folding was done manually to ensure facets adjacent to the creases for the “valleys” were rotated into the paper, while the facets adjacent to the creases for the “mountains” were rotated out of it [161]. An example of the folded paper Miura-ori is illustrated in Figure 4.1e. As indicated in Figure 4.1e, the angle obtained after folding, α', was smaller than designed. Hence, instead of 75° we obtained 43.75° ± 0.33°. Five paper Miura-ori were folded for each value of design parameter h.

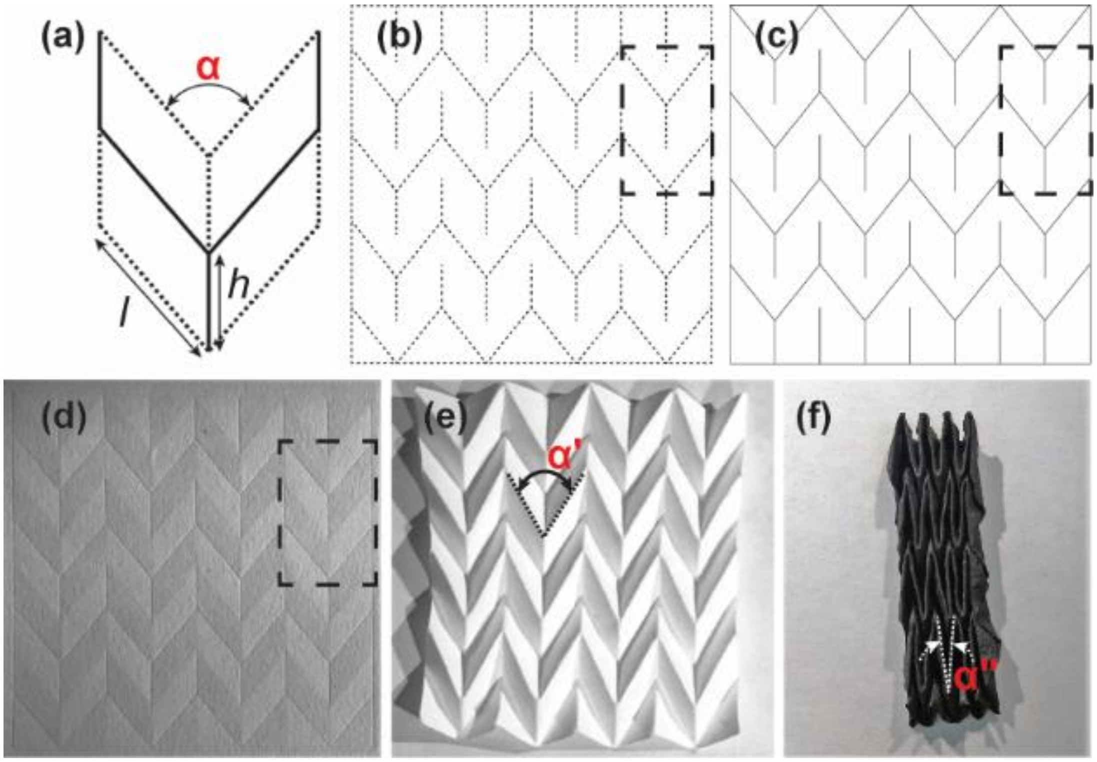

Figure 4.1: Fabrication process of carbon Miura-ori. (a) Unit cell of a Miura-ori pattern. The dotted lines represent the “valleys” and the solid lines indicate the “mountains”. The unit cell is defined by the characteristic design paremeters h, l and α. CAD software was used to create the crease patterns for (b) “valleys” on one side and (c) “mountains” on the opposite side of the paper for fabrication of Miura-ori. (d) Example of a paper creased using a modified cutting plotter. The unit cell of the Miura-ori pattern is indicated by the dashed rectangle, compare to (a). (e) Paper Miura-ori obtained by manually folding the creased paper shown in (d). because of manual folding, the design angle α decreased to the folding angle α'. (f) Carbon Miura-ori obtained by heat treatment of the paper Miura-ori at 900 °C in nitrogen atmosphere. Although shrinkage occurs, the shape is conserved. Because of the shrinkage, folding angle α' decreased to α'' for the carbon Miura-ori.

4.1.1.1.4. Carbonization

Once folded, the paper Miura-ori origami structures were carbonized in a tube furnace (TF1400, Across International, USA) using a well characterized protocol [177–180]. Due to a limitation on the size of the tube, the maximum dimension of the samples was 115 mm. The carbonization protocol featured 5 steps: (1) heating from room temperature to 300 °C at 5 °C/min; (2) dwell at 300 °C for 30 min to allow the excess oxygen to escape the furnace; (3) heating from 300 °C to 900 °C at 5 °C/min; (4) dwell at 900 °C for 75 min; and (5) cooling down to room temperature at a cooling rate of 5 °C/min. Process was done under a nitrogen atmosphere. An example of the resultant carbon Miura-ori is shown in Figure 4.1f. Shrinkage occurs, which yields a sharper folding angle, α'', when compared to the angle α' present after folding.

4.1.1.2. Characterization

4.1.1.2.1. Material characterization

The carbon miura-ori structure was characterized using X-ray diffraction (XRD, Rigaku Ultima IV, Japan) spectroscopy to determine its crystallographic structure. Thermogravimetric analysis (TGA) was performed to characterize weight loss during carbonization in nitrogen atmosphere with a heating rate of 5 ºC/min. The microstructures of both the precursor paper and the resultant carbon were using scanning electron microscopy (SEM, S4800, Hitachi, Japan). A thin carbon film (10 nm) was sputtered on the precursor paper to facilitate its imaging. The microstructure of the carbonized paper was further analyzed by high resolution transmission electron microscopy (HRTEM, H9500, Hitachi, Japan). The pore size distribution of the carbonized paper was characterized by image analysis of the SEM images using the particle analyzer, an inbuilt macro in the ImageJ software.

4.1.1.2.2. Structure characterization

Following current practices in cellular materials, the structural density (ρ) of the carbon Miura-ori structures was determined by the envelop method, which is the ratio between the mass of the carbon Miura-ori and the total volume it occupied [181,182]. The compression tests of the carbon Miura-ori structures were performed at a rate of 1 mm/min to 80% strain using an Instron Single Column Testing System (Model 5944). A load cell of 50 N was used for the compression tests. The stress-strain curve obtained in the compression test had three distinct regions: the elastic region, post-yielding softening and densification [183,184]. We calculated the compressive strength (σ_m) of the carbon Miura-ori sample as the onset point of fracturing of the panels, and the elastic modulus (E) as the slope of the elastic region of the stress-strain curve. This elastic region is characterized by the fact that the panels can stretch away from the creases to absorb the compression force.

4.1.2. Results and Discussion

4.1.2.1. Compressive strength and Elastic Modulus depending on structural density

The structural density (ρ) of different carbon Miura-ori structures is plotted in Figure 4.2a for different lengths of the characteristic dimension h of a Miura-ori unit cell (see Figure 3.1a). The density decreases from 0.03 ± 0.004 to 0.014 ± 0.005 g/cm^3 as h increases from 6.12 to 12.24 mm. An h of 6.12 mm is currently the smallest dimension we can fabricate with our current setup. The density of the structure as measured with the envelope method shows strong dependence on the length of h and hence size of the panel. This suggests that deformation of the structure during shrinkage and possibly elimination of byproducts during carbonization play an important role on determining the density of the carbon Miura-ori. These mechanisms are discussed in the shrinkage section. In this current section, we present the density values to emphasize the potential of carbon Miura-ori as a lightweight material. The structural density of the carbon Miura-ori obtained here ranges from 0.93% to 2% of the density of bulk glass-like carbon (1.3-1.5 g/cm^3 [185]).

The results from the characterization of σ_m and E are shown in Figure 4.2b. As expected, σ_m and E increase with the increase in density of the carbon Miura-ori. The value for σ_m increased from 4.12 ± 1.29 kPa for $\rho = 0.014$ g/cm^3 to 15.85 ± 2.21 kPa for $\rho = 0.03$ g/cm^3. The value of E increased from 49.37 ± 6.24 kPa for $\rho =$ of 0.014 g/cm^3 to 193.83 ± 32.17 kPa for $\rho = 0.03$ g/cm^3. Hence, σ_m and E are also inversely proportional to the design parameter h. In comparison, the average compressive strength of bulk glass-like carbon is in the range 300 – 700 MPa [186,187].

Cellular materials, including stochastic foams, can be characterized by the dependence on density of elastic modulus given by Gibson and Ashby's scaling law (Equation 4.1) [188]:

$$E \propto E_S(\rho/\rho_S)^n \qquad \text{Equation 4.1}$$

where E_S and ρ_S are the elastic modulus and the density of the solid respectively, and n is an exponent that represents the mode of deformation, e.g. bending or stretching [189]. The value of the constant n depends on the microstructure of the material as well as the structural geometry which includes the cell type (open or closed), the geometrical arrangement of the cells and the size of the cells [190]. Values of n beyond 2 represent rapid loss of interesting properties as density increases and signifies inefficient load transfer between the ligaments of the cellular structure [191]. Values of n less than 2 signifies better load transfer capability through the structure ligaments. A $n = 1$ denotes a stretch dominated structure, which exhibits higher compressive strength and stiffness in comparison to bending-dominant structures ($n = 2$) [189]. Plotting the relative elastic modulus, E/E_S, versus their relative density, ρ/ρ_S, shows that the Carbon Miura-ori origami structures features a $n = 1.76$ when considering the values for E_S and ρ_S as 20 GPa and 1.5 g/cm^3 for glass-like carbon respectively [192,193] (Figure 4.2c). This value is close to 2 which suggests a bending-dominant mechanical behavior similar to open cell cellular materials [194]. This was expected for Miura-ori because of the random collection of 5.26 ± 2.53 µm-thick fibers in the facets. Furthermore, Miura-ori in particular does not feature any strut at its basal plane, as in the case of octet-trusses for example [195], which is a characteristic for stretch-dominated microlattices [196]. A n = 1.76 also means that the carbon Miura-ori exhibits better scaling and better load transferring capability than other cellular materials with higher values of n. For example, silica aerogel and carbon nanotube (CNT) foams used for catalysts supports and energy storage applications respectively feature a n = 3 [181,197]. Carbon aerogels derived through carbonization of resorcinol-formaldehyde aerogel at 1100 °C feature a n = 2.7 at a porosity ranging from 80% to 95% [198]. Metallic microlattices feature a n = 2.4 [191], while graphene foams display a n = 2.5 [199]. Hence, the carbon Miura-ori structures presented here compare advantageously to other common lightweight cellular materials in terms of scaling and load transfer capabilities. However, the compressive strength of the carbon Miura-ori structures (4.12 kPa – 15.85 kPa) feature less compressive strength than other structural materials with similar density such as metallic microlattices (70 kPa – 3 MPa) [195] and carbon foam (~ 50 kPa) [198]. We hypothesize that the random distribution of the open pores among the carbon fibers and the high standard deviation of the fiber diameter are the reason for the low compressive strength. We provide further details on the microstructure of the carbon fibers in later scetion. Ongoing work is on using different pure cellulose films with different microstructures. The control over smaller scales is expected to yield a significant increase in compressive strength as recently reported by other authors [200].

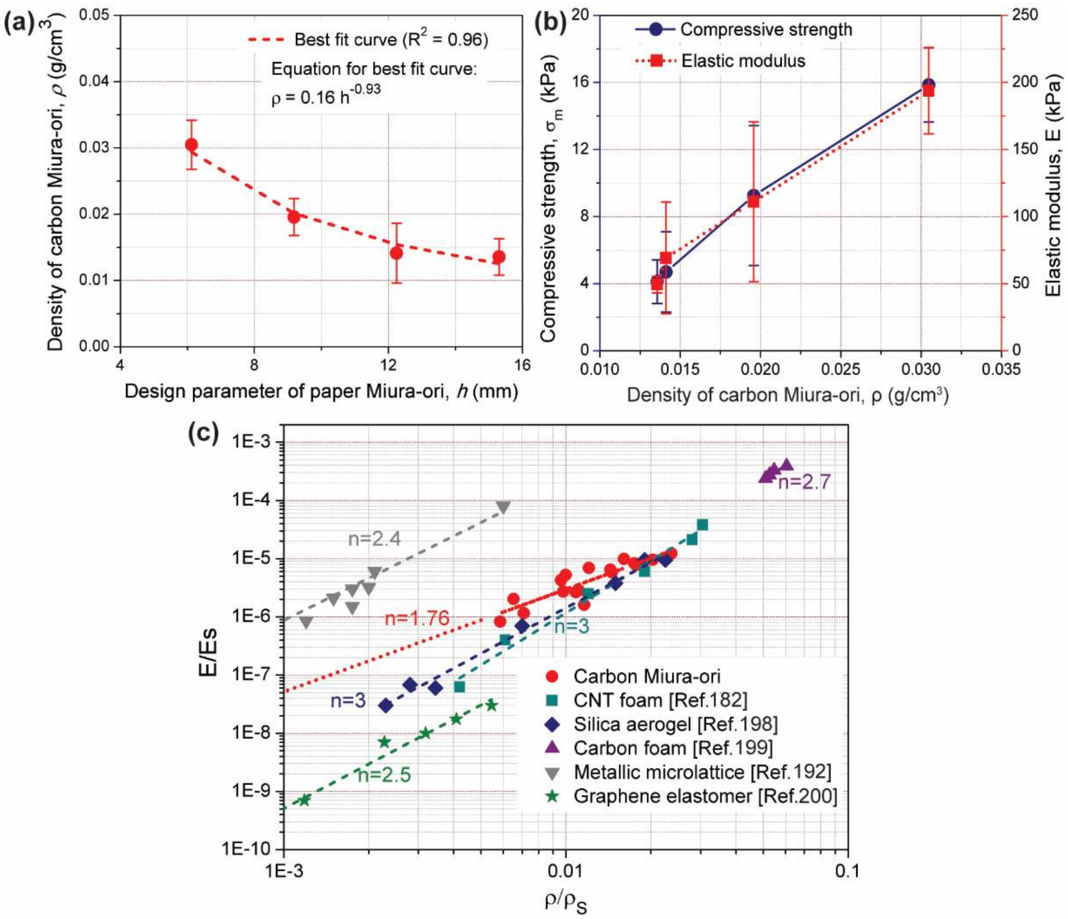

Figure 4.2: **(a)** Density (ρ) of carbonized Miura-ori of different sizes. At least five Miura-ori were characterized for the shrinkage and the density for each value of *h*. The error bars represent the standard deviation in the measurement. The red dashed line represents the best fitted curve to the density. **(b)** Plots of compressive strength (σ_m) and elastic modulus (E) against density of the carbon Miura-ori. The large standard deviations are attributed to the random distribution of carbon fibers. **(c)** Relative elastic modulus (E/E_S) of carbon Miura-ori with comparison to other low-density materials.

Paper manufacturing involves pulping of wood chips followed by chemical treatment of the pulps, mechanical pressing, and drying [201]. The microstructure of paper, i.e. fiber dimension and spatial arrangement, depends on the source of the wood pulp, pulping method, treatment of the pulp and the mechanical pressing [202]. Different microstructure of the paper can be obtained by controlling these processing steps. For example, fibers from softwood feature slenderness ratio (length/diameter) ranging from 95 to 120, whereas fibers from hardwood have slenderness ratio ranging from 55 to 75 [202]. Higher slenderness ratio translates to a higher density of paper and lower pore size distribution. Furthermore, paper made from thermomechanical pulping possesses 25-40% higher porosity than that made from chemical pulping [203]. The maturity of the paper industry represents an excellent stepping stone towards manufacturing carbon origami of tailored properties. Once paper is obtained with specific microstructural properties, the continuous processing for carbon origami will be enabled.

4.1.2.2. Characterizing the microstructure of carbon origami

The results from the XRD characterization of the carbonized paper (Figure 4.3) show weak and broad peaks centered around $2\theta = 24°$ and $2\theta = 43°$, which are the characteristics of (002) and (100) reflections of amorphous carbon [109,110].

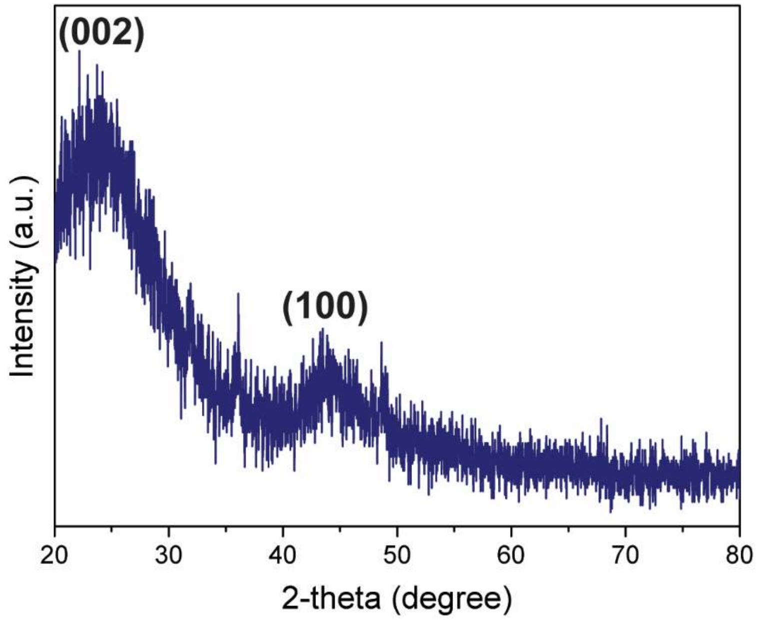

Figure 4.3: XRD of the carbonized chromatography paper. The presence of peaks at 24 and 43° indicate amorphous carbon.

The chromatography paper used in this work was basically a collection of tightly packed cellulose fibers as shown in Figure 4.4a. The average diameter of these fibers was 17.48 ± 3.06 µm. The carbon obtained after heat treatment is shown in Figure 4.4b. No impurities were observed on the carbon matrix. This in contrast to significant impurities reported when carbonizing other paper types which are not marketed as pure cellulose [164]. The fibers shrank to an average diameter of 5.26 ± 2.53 µm, resulting on an average linear shrinkage of fiber diameter of 69.89 ± 5.59%. The spacing between fibers is of random nature leading to macroporosity of varying dimensions in the range from 1.56 µm to 21.71 µm (inset of Figure 4.4b).

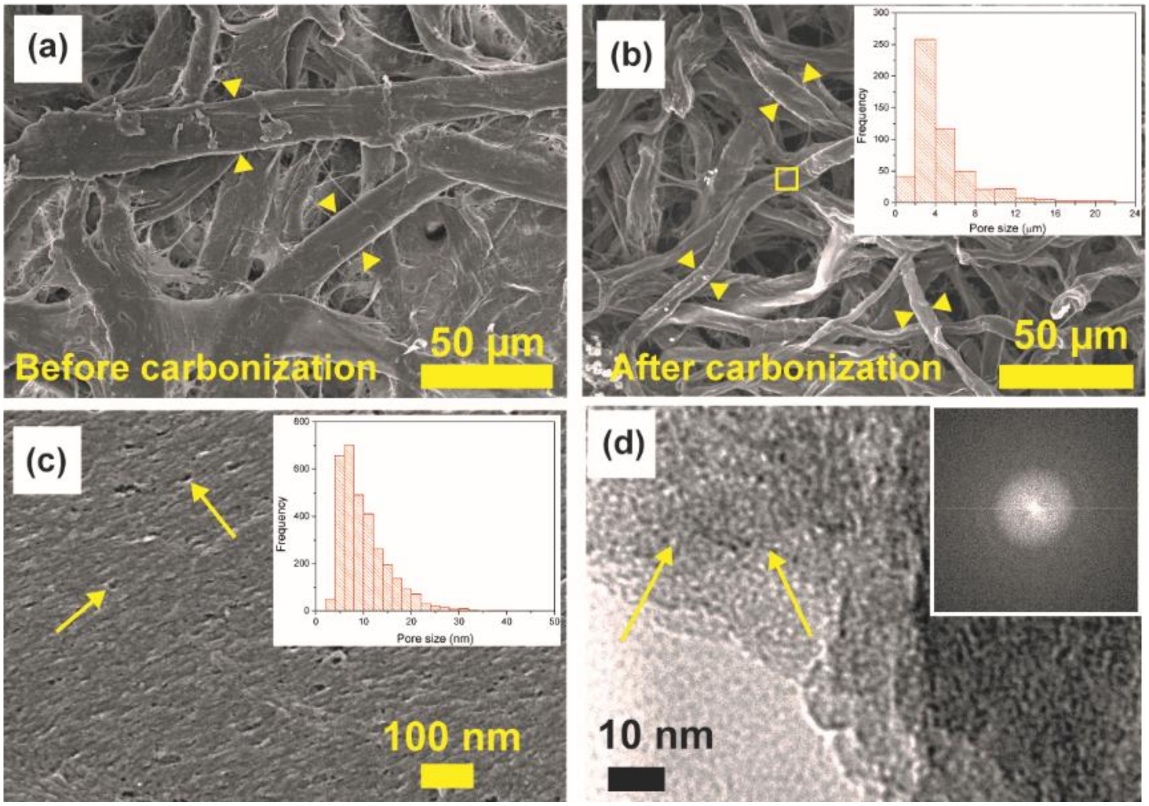

Figure 4.4: FESEM image of chromatography paper **(a)** before and **(b)** after carbonization at a magnification of 600X. The arrows indicate the diameter of the fibers. Diameters were measured for at least ten fibers in both cases. Inset of (b) represents the pore size distribution of the open pores. The diameter of the open pores ranges from 1.56 µm to 21.71 µm. (c) High magnification FESEM image of the carbonized chromatography paper at a magnification of 120k showing the mesoporous structure of the carbon fibers. Representative examples of the pores are indicated by the arrows. Pore diameter ranges from 3.15 nm to 44.78 nm as shown in the inset. (d) HRTEM image of the carbonized chromatography paper showing the micropores in the carbon material. Examples of the micropores are indicated by the arrows. The electron diffraction pattern in the inset shows no ring or spot, which confirms the amorphous nature of the carbon sample.

The mechanical properties of a material are known to depend on its microstructure [204]. Hence, the compressive strength (σ_m) and elastic modulus (E) of the carbon Miura-ori would depend on the fiber composition, diameter and spacing between them. We hypothesize that the high standard deviation in the carbon fiber diameter and random and wide distribution of the open pores caused the high standard deviation in σ_m and E as seen in Figure 4.2b. An improvement of mechanical properties is to be expected if using a fiber matrix with smaller fiber diameter, as reported by other authors [204–206]. Use of smaller fibers can enhance packing in the matrix, thus yielding smaller pores between fibers. Ongoing work is on elucidating the impact of using different cellulose matrices as carbon precursors.

The carbon fibers themselves display a wide range of open pore sizes. SEM analysis at magnification of 120k revealed a mesoporous structure with pore diameter ranging from 3.15 nm to 44.78 nm (Figure 4.4c). TEM studies at magnification up to 500k further suggested presence of micropores (pore diameter < 2 nm) within the fibers (Figure 4.4d). However, at the presented scale, it is hard to identify and measure the size of the micropores. Further studies using nitrogen adsorption-desorption will be needed to properly characterize these micropores. Our hypothesis is that the escape of gaseous substances during carbonization causes these micropores in the carbon material and the compact aggregation of these material results in the mesoporous structure. This hypothesis is in accordance with previous reports on synthesis of porous carbon from biopolymer precursors [178,207,208]. These micro- and mesopores also contribute to the microstructure and mechanical properties of the carbon Miura-ori. With increased micro-and mesopores, the carbon fibers become less dense resulting in a decrease in σ_m and E [209]. We expect the micro- and mesoporosity to be increased by augmenting the carbonization temperature. The use of carbonization temperatures up to 1000 °C has been shown to enhance material release during carbonization and yield a material with increased micro- and meso-porosity [210].

The electron diffraction analysis performed during TEM revealed no spots or rings that correspond to any crystal plane (inset of Figure 4.4d). This supports the previous finding from XRD about the amorphous nature of the carbon sample.

4.1.2.3. Structural shrinkage

Thermogravimetric analysis (TGA) was performed to calculate the carbon yield of chromatography paper. The results from the TGA are shown in Figure 4.5 and are in accordance with other authors [211–214]. A sharp weight loss occurs between 300 °C and 380 °C, which is attributed to the thermal decomposition of cellulose in form of volatile components such as levoglucosan, hydroxyacetaldehyde, acetol, CO and CO_2 [99]. Above 380 °C, a gradual weight loss at approximately 0.0097%/°C can be observed which is mainly caused by elimination of oxygen and hydrogen in the form of CO, CO_2 and C_xH_y [100]. The carbon yield at 900 °C in nitrogen atmosphere for the chromatography paper used here is 4.4%, which is in agreement with previous reports [164]. Other types of paper, such as printing paper and Whatman filter paper, were reported to feature a yield in the range of 3 – 23% [99,164]. The yield of 4.4% may seem to conflict with the ~70% linear fiber shrinkage reported above. The theoretical linear shrinkage of the diameter of a solid carbon fiber derived from cellulose is expected to be 79% when considering a 4.4% carbon yield and assuming similar densities for both carbon and cellulose [215,216]. This value can be obtained by equating the mass of a cellulose fiber per unit length (cross-sectional area times density) with that of a carbon fiber featuring a diameter 0.044 times of the cellulose fiber. However, such calculation does not consider the porosity of the fibers illustrated in Figure 4.4. We expect the porosity to account for the difference between the theoretical 79% and the observed 70% linear shrinkage. Further studies are required to fully characterize the porosity and exact density of both cellulose and carbon fibers.

The carbon yield is expected to change according to the heating environment. Inert gases commonly used for carbonization include helium, nitrogen, argon and forming gas (Nitrogen and 5% Hydrogen). Su and Lua reported that the thermal conductivity of the gas has an important role on the carbon yield [200]. They determined the convection heat transfer coefficient of helium, nitrogen and argon using an equation correlating Nutshell number with Prandtl number at a volume flow rate of 11.3 ml/min and an inside diameter of 23.55 mm for the tube furnace [200,217]. At 800 °C, they calculated the convection heat transfer coefficient of helium, nitrogen and argon to be 109.20, 18.89 and 12.79 W/m^{2}K respectively. This suggests that a helium environment will result in a lower carbon yield when compared to nitrogen and argon environments. Furthermore, Dickens reported that the use of vacuum facilitates the evacuation of carbonization byproducts when compared to the use of inert gas atmospheres; which would translate to a lower carbon yield as well [218]. Further work is needed to determine the convection heat transfer co-efficient of different gases for our system and characterize the weight loss in such heating environment for Miura-ori.

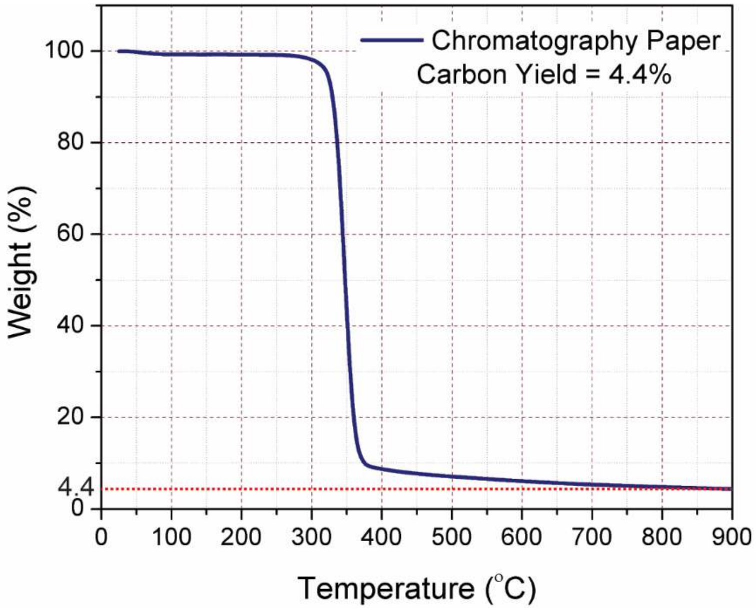

Figure 4.5: TGA of chromatography paper with a heating rate of 5 °C/min in nitrogen atmosphere. Around 90% weight loss occurs in the range 320 °C – 380 °C. A 4.4% carbon yield was obtained at 900 °C.

The structural shrinkage of the Miura-ori structure is the result of processes at various length scales: from micrometric fibers to centimetric structures. As a reference, the carbonization of a flat piece of paper without the Miura-ori structure resulted in a curved carbon film (see insert in Figure 4.6a). The possible reasons for such curved film include induced pressure by the volatile products and associated swelling or blistering during the heat treatment, and the thermal contraction that results during cooling [219–221]. We further speculate that the random distribution of the fibers causes unequal stresses within the fibers during carbonization. However, further investigation is needed to understand such phenomena. Remarkably, a paper piece of the same dimensions but shaped as Miura-ori does not curve during carbonization (Figure 4.6a). Our hypothesis is that the dynamics of the Miura-ori structure facilitates the release of thermal stress and thermal contraction through shrinkage, which prevents it from curving. Interestingly, the amount of shrinkage in different axis of the Miura-ori is different as shown in Figure 4.6a. We calculated shrinkage using Equation 4.2, where L_{Pi} and L_{Ci} are the dimensions of the paper Miura-ori and carbon Miura-ori respectively in the i-axis. Most of the shrinkage occurs on the horizontal plane and in the direction perpendicular to the characteristic dimension h. We denoted this direction as the Y-axis. The least shrinkage happens in the X-axis, or the direction parallel to h. The shrinkage in X with respect to h is constant, slightly variable in the case of Y-axis and significantly different for the Z-axis.

$$Shrinkage\ (\%) = \frac{L_{Pi} - L_{Ci}}{L_{Pi}} \qquad \text{Equation 4.2}$$

The material loss during carbonization results in shrinkage of the fibers and this can be explained by the elimination of byproducts from carbonization. We hypothesize that the origami structure has an impact on the evacuation of byproducts. This is because the weight of a carbonized piece of paper with the same dimension than the one used for Miura-ori but without creasing and folding is 10–20% less than the carbon Miura-ori. During carbonization, the decomposition of cellulose produces condense-phase product, which evaporates. The nitrogen gas flowing in the tube aids the evaporation of the byproducts by increasing the mass transfer co-efficient [222]. However, in the case of Miura-ori, it can be possible that the nitrogen gas cannot reach the intricate parts of the Miura-ori uniformly.

For example, disturbances in the laminar flow in the tube can be introduced at the folding corners. This results in inefficient mass transfer from those intricate parts and volatile intermediates may get enough time to crosslink and stay as a part of the solid. Therefore, a higher mass is obtained for the carbon Miura-ori. Future work will be required to support this hypothesis and characterize this phenomenon further.

The dynamics of the Miura-ori structure are likely to play a role in shrinkage. It is known that a Miura-ori structure offers the least mechanical resistance in the Y-axis, followed by the Z-axis and lastly the X-axis. The shrinkage reported here follows this trend in all samples (Figure 4.6b). Shrinkage of the fiber network during carbonization leads to pulling stresses that find the least resistance in the Y- and Z-axis. Shrinkage also depends on the characteristic dimension h. As h increases, the shrinkage in Y-axis slightly decreases and Z-axis slightly increases. The characterization of the fold angle after carbonization (α'') of Miura-ori structures exposes the fact that α'' is directly proportional to h (Figure 4.6b). Hence, the unit cell of a Miura-ori is elongated during carbonization and this elongation increases as h decreases (plot of α" in Figure 4.6b). According to the geometry of Miura-ori, the dimension in Y-direction is directly proportional to α'' and the dimension in Z-direction is inversely proportional to α'' [171]. Hence, the dimension in Y-direction increases with h resulting in decreasing shrinkage, whereas the dimension in Z-direction decreases with the increase in h resulting in higher shrinkage. The results obtained here suggest a plateau on the folding angle value α'' for $h > 12.2$ mm. However, further experiments in a bigger furnace than ours are required to conclude on this. In order to assess the effect of the thickness of the precursor paper, we compared the dimensions of i) paper

Miura-ori folded with chromatography paper of 0.19 or 0.34 mm and the ii) resultant carbon origami after similar heat treatment of both paper Miura-ori. The dimensions in paper were similar, and the amount of shrinkage during carbonization remained the same in all directions regardless of the paper thickness (data not shown). Since both papers featured similar pure cellulose fibers and fiber density, our hypothesis is that the fibers experience similar material loss and thermal contraction force during the heat treatment irrespective of the paper thickness.

The shrinkage behavior detailed above helps explain the decreasing density of the carbon Miura-ori as h increases. An increasing value of h means that the size of the panels of the paper Miura-ori structure increases. This effectively decreases the density of the Miura-ori by introducing larger voids in the structure. Furthermore, shrinkage during carbonization results in retraction of the panels towards each other, caused by the reduction of the folding angle as h decreases. The angle between panels in the vertical plane is 44.08° ± 7.81°. The bigger the reduction on the folding angle is, the higher the density of the structure becomes. Hence, small values of h yield increased values of structural density. The plateau in α'' in Figure 4.6b results in a plateau in structural density reflected in Figure 4.2a. As mentioned before, further experiments are needed with Miura-ori structures with $h > 16$ mm to validate this observation.

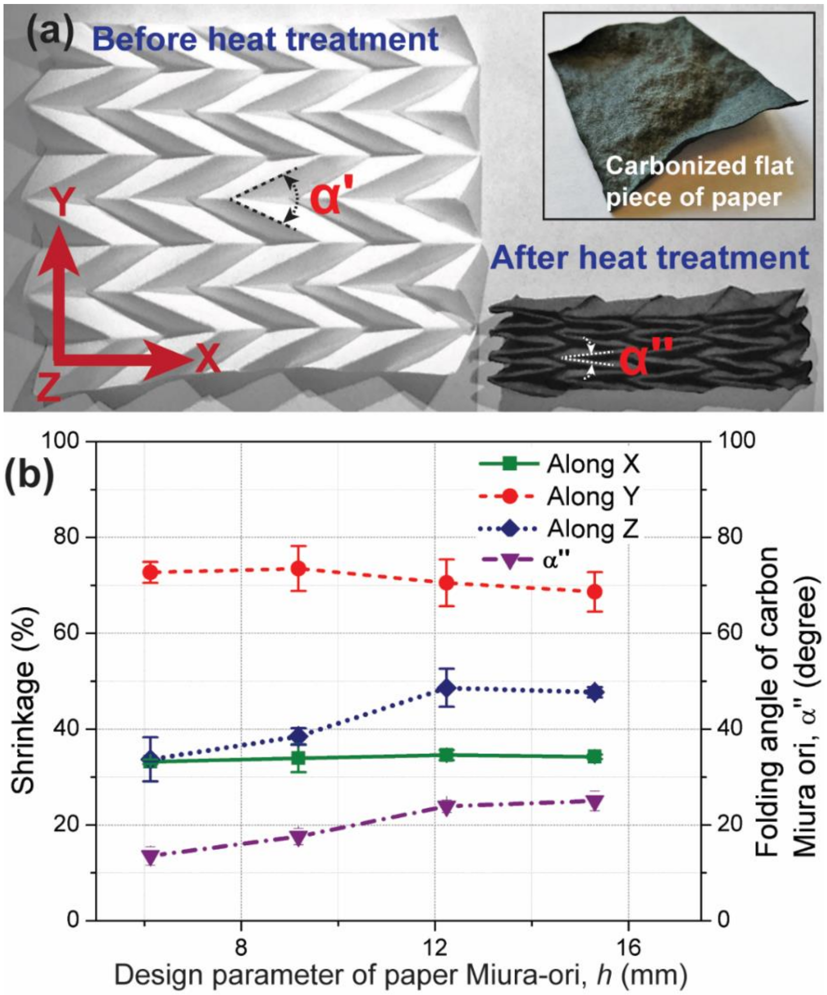

Figure 4.6: (a) Miura-ori before and after heat treatment. Note that the carbon structure retained the Miura-ori pattern, whereas carbonization of a flat piece of paper results in a randomly curved piece of paper as shown in the inset. Shrinkage occurs during the carbonization. In case of carbon Miura-ori, maximum shrinkage occurs along Y-axis, followed by X- and Z-axis. (b) Shrinkage in X-, Y-, and Z-direction for different sizes of Miura-ori. Maximum shrinkage occurred in Y-direction followed by Z- and X-direction. The folding angle of the carbon Miura-ori (α'') was also plotted for different sizes of Miura-ori. The error bars represent the standard deviation in the measurement.

4.1.2.4. Versatility of the fabrication process

We performed studies to elucidate the minimal dimensions achievable in different origami structures when using the manual fabrication technique presented here. The ultimate goal is to automate folding techniques and this initial study is aimed at identifying challenges towards this goal. Previous authors attributed the failure of folding Miura-ori to the occurrence of folding defects such as curl, crimps and kinks in the facets, which were due to bending and compressive stresses exerted on the facets during manual folding [223]. Here we focused on elucidating the impact of shape complexity on the minimal origami dimensions that are achievable by an average human folder. We studied Miura-ori, Waterbomb base and Yoshimura (Figure 4.7) to account for different complexities. The upper limit on dimensions was given by the diameter of the furnace tube used in this work (120 mm). Pre-creasing was achieved across all dimensions tested here since the resolution of the pen, 1.5 mm, was smaller than the separation between all lines.

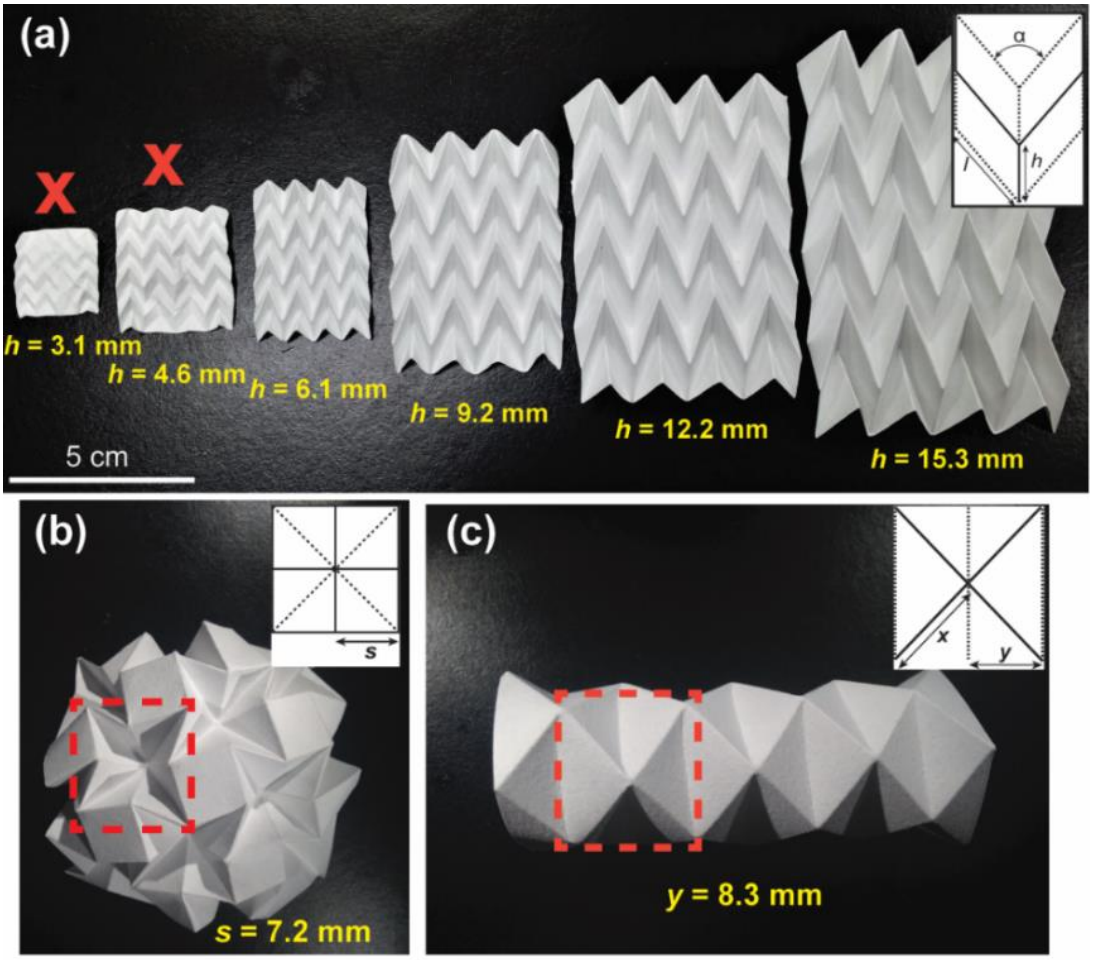

Figure 4.7: (a) Paper Miura-ori with different value of design parameter *h*. The Miura-ori with red cross at the top represents the failed attempts. In case of a failed structure, folding defects such as curl, crimps and kinks occurred due to bending and compressive stress exerted on the facets during the manual folding. (b) Waterbomb base and (c) Yoshimura were folded to characterize the effect of complexity on scalability. Unit cells of each origami structures are shown in the inset of corresponding images and denoted by the red dotted square in the folded paper structures.

The complexity of the origami structure can be characterized by N, which is the ratio between the number of crease lines and the area of paper. Miura-ori is the most complex, with highest N, shape among the three studied here followed by Waterbomb base. This means that for a given paper area, a Miura-ori fold features more crease lines. N can then be related to the characteristic size of the different origami structures as given by their unit cell. In this work, the unit cell of Miura-ori is characterized by h, the Waterbomb base by s and Yoshimura by y. For a given length of h, s and y, a Miura-ori features a higher N. Results (Figure 4.8) indicate that the achievable structure depends on the attempted shape and the characteristic size of its unit cell. The minimal length of the characteristic dimension to achieve an origami structure depends on the shape. A value of $h \leq 4.6$ mm was not achievable in Miura-ori, while values of $s \leq 3.6$ mm and $y \leq 2.1$ mm were not possible with Waterbomb based and Yoshimura respectively. In other words, Miura-ori requires the largest size of paper area among the three shapes for a specific N. A value of N greater than 0.05 mm^{-2} failed for all the three shapes during the manual folding. At such value of N, the number of crease lines per unit area of paper becomes so high that the distance between adjacent creases becomes extremely close for manual folding. At such condition, the fold propagates beyond the prescribed crease lines during manual folding and interferes with other adjacent crease lines. This results in folding defects such as curl, crimps and kinks in the facets.

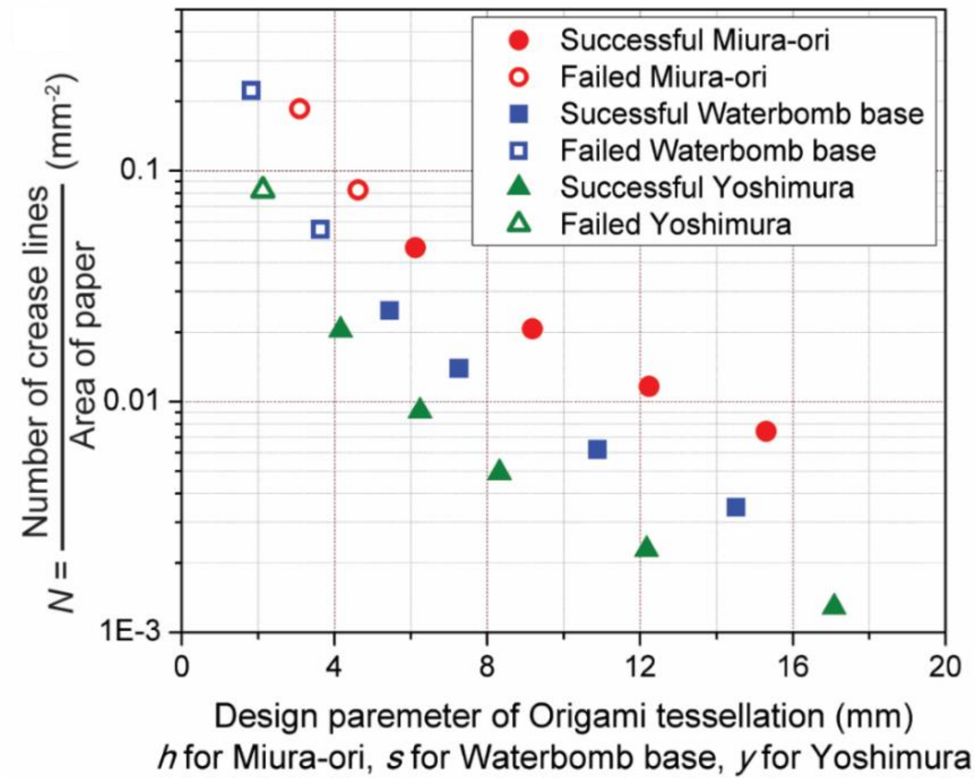

Figure 4.8: The number of crease lines per unit area of paper represents the complexity of the origami structures. Ratio of number of crease lines over area of paper were plotted for different sizes of Miura-ori, Waterbomb base and Yoshimura. Note that manual folding fails over a number of crease lines to area of paper ratio of 0.05 mm^{-2}.

The upper limit of scalability for paper creasing in our case is entirely dependent on the capabilities of the cutting plotter used to pre-crease the paper. The cutting plotter used in this experiment features a maximum cutting area of 375 mm × 50 m. This large cutting area can permit large patterned sheets to be created using the pre-creasing method as long as the features are scaled to the appropriate size. However, large sheet of paper may be more difficult to control, especially during manual folding of the complex origami structures. In future large-scale manufacturing, the manual folding can be avoided by using upcoming reprogrammable robots [224–226] or processes akin to those used in the manufacturing of paper bags and filters [227]. This will eliminate the dependence of dexterity of the user and likely allow for defect-free folding of the creased paper. It could also allow for fabrication of origami shapes having $N > 0.05$ mm^{-2} and afford better control while handling large sheets of paper. The use of embossing rollers [228–230] to automate the continuous creasing of paper, and the use of rolling furnaces to carbonize origami structures complement automatic folding towards large-scale manufacturing of carbon origami. Rolling furnaces are already common practice in the manufacturing of tiles and other ceramic parts [231].

4.1.3. Concluding remarks

In this work, we demonstrated the fabrication of lightweight, rigid carbon cellular materials using origami techniques. We automated the pre-creasing of flat pieces of cellulosic paper to facilitate the manual folding of origami structures. 3D complex origami shapes of carbon were obtained after carbonization. These featured a unique hierarchical porous microstructure as characterized by SEM and TEM. Shrinkage occurred both in the micro- and macro-scales during the carbonization due to the release of carbonization byproducts. The shrinkage in the macro-scale also depended on the dynamics of the origami shape. The carbon structures featured low density, comparable to other materials such as CNT foams and graphene elastomer that require more complex fabrication processes. The Miura-ori cellular material displays a bending dominant failure under compression (n = 1.76). The carbon Miura-ori exhibited low absolute compressive strength and elastic modulus due to the random and wide distribution of the open pores. However, it featured better scaling of relative stiffness when compared to other cellular engineering materials such as silica aerogel, carbon aerogel, graphene elastomers, metallic microlattices and CNT foams. This indicates better load transfer capability of the carbon Miura-ori when compared to these other cellular engineering materials. The large-scale manufacturing of carbon origami is envisioned to include embossing rollers to pre-crease the paper, automatic folding using robots and continuous heat treatment using rolling furnaces.

We postulate carbon origami as a technique to fabricate multifunctional cellular materials. Here we demonstrated the initial mechanical properties of carbon Miura-ori structures. Further work is necessary to improve these properties by controlling the microstructure of the carbon by tailoring the structure of the precursor paper and heating protocols. The use of porous carbon in energy applications such as batteries, fuel cells and capacitors is well known. In fact, cellulose derived carbon by itself or functionalized with metallic nanoparticles has been shown to have excellent electrochemical responses preferable for applications such as batteries, capacitors, CO_2 reductors and fuel cells [163,232–234]. Further work to elucidate the effect of processing on the surface area and electrochemical properties of carbon origami is necessary. Such studies will also further the use of porous carbon for sensing [163]. The combination of the results emanating from electrochemical and mechanical studies can lead to the development of origami structures with tailored mechanical, energy and sensing properties. For example, lightweight structural capacitors and batteries that are capable to sustain a mechanical load and can monitor their environment. The fact that such carbon material has excellent chemical inertness and can sustain temperatures up to 500 °C under oxidative environments [235] and up to 2500 °C in inert conditions [236] suggests their use in harsh, high temperature applications such as structural filters in diesel engines [237] and during the processing of certain molten materials [238].

SECTION 4.2: Origami-inspired manufacturing of fibrous tungsten carbide shapes

In this work, we present the fabrication of 3D origami structures of WC material by integrating the folding technique described in the Section 4.1 with the synthesis method discussed in the Chapter 2. As found in the Chapter 2, temperature is the most influencing parameter for synthesis of WC from CG paper, we characterize the effect of synthesis temperature on the composition and the grain size of WC. Further we discuss the effect of temperature on the mechanical properties of the heat-treated Miura-ori samples. We also address the mechanical properties of WC Miura-ori of different sizes. We point out the place of the WC Miura-ori in the material chart among different other cellular ceramic materials. We finish by furthering the discussion for the potential for large-scale manufacturing of WC Miura-ori.

4.2.1. Experimental section

4.2.1.1. Materials

As mentioned in Section 4.1, pure cellulose chromatography paper (Fisherbrand Chromatography Paper, Sigma Aldrich, Cat. No. 05-714-1) with a thickness of 0.19 mm was used for this work. Ammonium Meta tungstate (AMT, Sigma Aldrich, Cat. No. 463922) was used as the liquid precursor for synthesis of WC as mentioned in Chapter 2.

4.2.1.2. Fabrication of WC Miura-ori

The fabrication of the paper Miura-ori is detailed in the previous section (Section 4.1). Briefly, the paper Miura-ori was fabricated by automatic pre-creasing of a flat piece of paper by a modified cutting plotter machine followed by manual folding. The Miura-ori samples fabricated here featured an α of 75° and a 3:5 ratio between h and l. Once the Miura-ori is folded, we immersed the paper Miura-ori in a 20% AMT solution for 20 minutes to make sure the paper is inflitrated with the AMT. At this point, the folded structures generally became almost flat beacause of the weight of the water. To reatin the Miura-ori structure, the paper needed to be folded again. However, it is extremely challenging to fold the paper in wet condition. Therefore, the AMT infiltrated Miura-ori structures were taken out from the solution and dried on a hot plate at 85 °C for 1 hour to facilitate the second folding.

Once folded, the folded Miura-ori structures were heat-treated in a tube furnace (TF1400, Across International, USA). As mentioned in Chapter 2, the heat treatement protocol featured 5 steps: (1) heating from room temperature to 300 °C at 5 °C/min; (2) dwell at 300 °C for 30 min to allow the excess oxygen to escape the furnace; (3) heating from 300 °C to an elevated temperature; (4) dwell at the temperature for 3 hours; and (5) cooling down to room temperature at a cooling rate of 5 °C/min. As temperature is the most influential parameter for the synthesis (See Chapter 2), different final temperatures were used in step (3) to investigate the effect of temperature on the macro-structural and compositional properties of the Miura-ori samples. The whole process was performed under a vacuum atmosphere.

Furthermore, the macrostructural properties were characterized for different sizes of Miura-ori which were heat traeted using the optimum heating conditions i.e. synthesis temperature of 1300 °C, heating rate of 2.5 °C/min and 20% AMT concentration. As we obtain WC as the main material at these conditions, we refer the Miura-ori samples obtained using these synthesis conditions as WC Miura-ori. To obtain different sizes of WC Miura-ori, we varied the value of *h* from 6.12 mm to 10.7 mm. An example of the WC Miura-ori after heat-treatment is shown in Figure 4.9c.

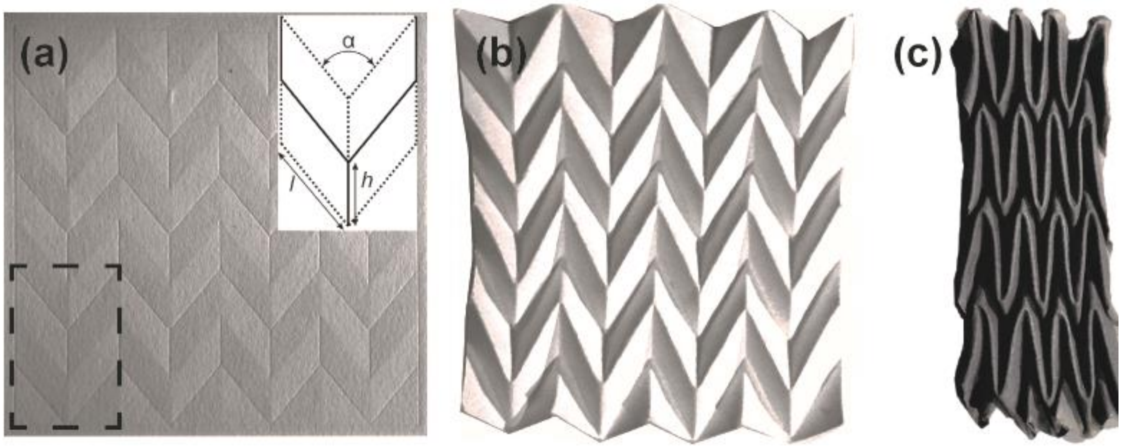

Figure 4.9: (a) The flat piece of paper pre-creased with the cutting plotter machine. The inset shows the unit cell of a Miura-ori. The unit cell parameters are indicated on the unit cell. The rectangle shown by the dahsed line shows the unit cell on the precreased paper. (b) Paper Miura-ori structure obtained after manually folding of the pre-creased paper. (c) WC Miura-ori obatined after heat treatment of a paper Miura-ori infiltrated by 20% AMT solution at 1300 °C with a heating rate of 2.5 °C/min in vacuum environment.

4.2.2. Results and Discussions

4.2.2.1. Effect of synthesis temperature

4.2.2.1.1 Effect of temperature on the composition and grain size

The XRD patterns of the samples obtained from the heat treatment of the AMT filtrated Miura-ori at different temperatures are shown in Figure 4.10a. The peaks for hexagonal tungsten carbide (WC) are identified at the 2θ angles of 31.7°, 35.9°, 48.6°, 64.4°, 66.1°, 73.5°, 75.8°, and 77.3° which are indexed to the (001), (100), (101), (110), (002), (111), (200) and (102) crystal planes respectively (ICDD PDF number 01-089-2727). The other major peaks in the XRD patterns are indexed to tungsten hemicarbide (W_2C) and tungsten (W) according to ICDD PDF numbers 01-071-6322 and 00-001-1204 respectively. No presence of WC is observed in the XRD patterns for 800 °C and 900 °C. At 800 °C, the peaks in the XRD pattern correspond to WO_3, which suggests that the AMT is reduced to WO_3. The peaks for WO_3 disappear in the XRD pattern for 900 °C. However, in both the XRD patterns, a wide peak around 2θ = 40.3 °C can be observed, which is reflection of metallic tungsten. This suggests that the reduction of WO_3 to metallic W started before 800 °C and completed at 900 °C. At 1000 °C, peaks for WC can be observed along the hemicarbide form (W_2C). However, metallic W is the dominant material in the sample at this temperature. This indicates the carburization of the metallic W starts in between the temperatures 900 °C – 1000 °C. The intensities of the peaks for WC increases as the synthesis temperature increases, whereas as the peak intensity for metallic W decreases. Finally, the peak for the W disappears in the XRD pattern for 1300 °C. However, a small amount of W_2C is present in the sample. In all the XRD spectra, a bulging pattern can be observed in between the angles 2θ = 20° to 2θ = 30°. Such bulging pattern corresponds to the amorphous nature of the free carbon present in the material.

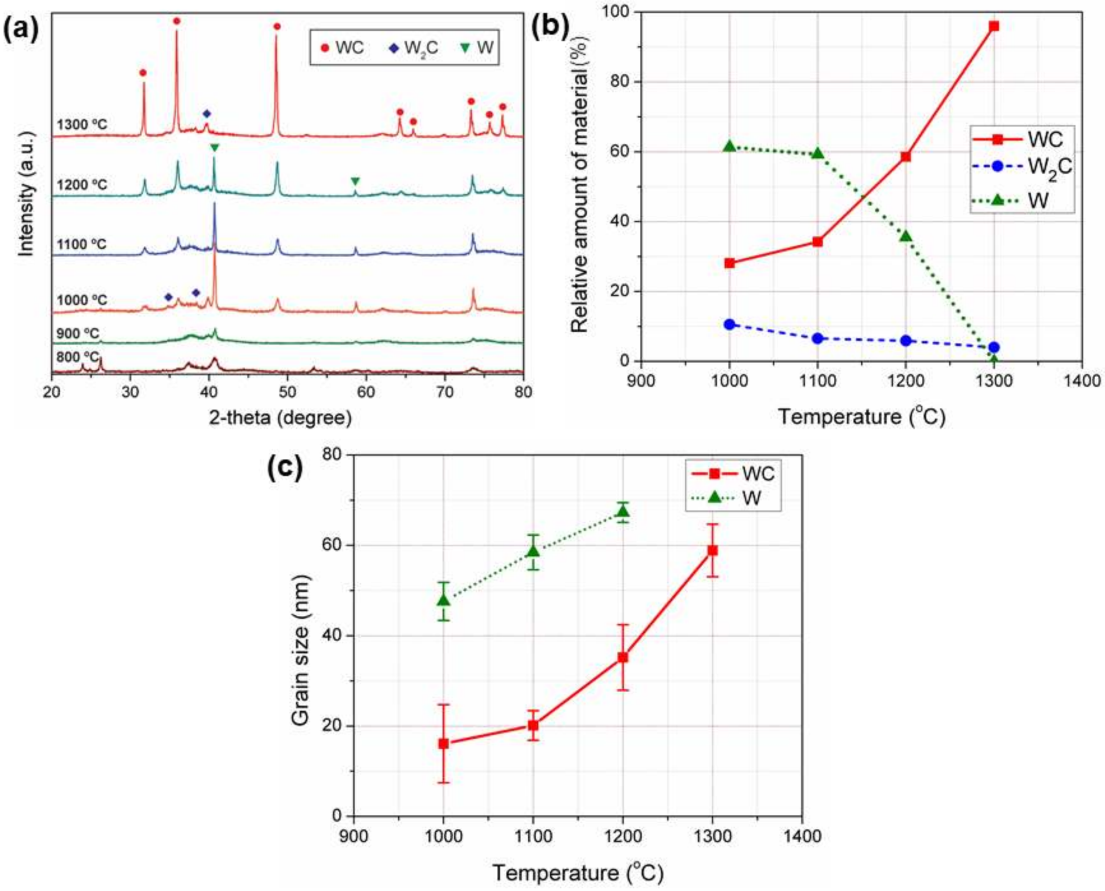

Figure 4.10: (a) XRD patterns for the heat-treated Miura-ori samples at different temperature. (b) Relative amount of the crystalline materials present in the heat-treated Miura-ori samples at different temperature. The relative amount was calculated from the XRD patterns using the Equation 4.3. (c) Effect of synthesis temperature on the grain size of WC and W. The grain size was estimated from the XRD patterns using Scherrer equation (Equation 2.1).

We estimated the relative proportion of the materials present in the sample using the XRD patterns. The relative amount of each material is estimated using Equation 4.3 and is plotted in Figure 4.10b. This proportion is limited to only the crystalline materials present in the sample. The free carbon in the sample is not considered here due to its amorphous nature. As the temperature increases, the relative amount of WC increases proportionately, whereas relative amount of W decreases with increasing temperature. At 1300 °C, the relative amount of W becomes zero, which suggests complete carburization of the metallic W. Although the amount of W_2C decreases with temperature, a small amount of W_2C is still present in the sample obtained at 1300 °C. At this temperature, the amount of WC is 96% and the rest of 4% is W_2C. We expect the W_2C to completely carburized to WC by heating above 1500 °C [134]. However, we could not do test at a temperature higher than 1300 °C due to the limitation of the experimental set up.

$$Relative\ amount\ of\ a\ material =$$

$$\frac{Sum\ of\ the\ intensites\ of\ the\ peaks\ for\ the\ particular\ material\ in\ XRD}{Sum\ of\ the\ intensities\ of\ all\ the\ peaks\ present\ in\ XRD} \times 100\%$$

Equation 4.3

We estimated the grain size of the WC and metallic W using the Scherrer equation and plotted in the Figure 4.10c. We did not plot the grain size for W_2C, as the amount of W_2C present in the samples are insignificant compared to the amount of WC and W. Hence, there is minimal impact of the W_2C on the macrostructural properties. The grain size of both WC and W increases with the increase of temperature. The grain size of WC increases from 16.1 ± 8.63 nm at 1000 °C to 58.88 ± 5.81 nm at 1300 °C. The grain size of metallic

W increases from 47.6 ± 4.22 nm at 1000 °C to 67.3 ± 2.19 nm at 1200 °C. This is expected as higher temperature facilitates the sintering of the particles yielding larger grains.

4.2.2.1.2 Effect of temperature on structural density and mechanical properties

We characterized the structural density and the mechanical properties of the Miura-ori obtained at different temperatures. The results for the structural density is shown in Figure 4.11a. No significant change in the structural density could be observed with increasing temperature. By the temperature of 1000 °C, all the AMT is reduced to W and the cellulose is decomposed to carbon. Hence, no material release occurs above the temperature of 1000 °C. In the temperature range 1000 °C to 1300 °C, the main chemical process that occurs is the carburization of the W. Due to this compositional change, the density of the material changes in the molecular level. However, the scale of the Miura-ori is extremely large. Hence, the density change in the material is not realized in the structural density.

The compressive strength and the elastic modulus of the Miura-ori treated at different temperature are plotted in Figure 4.11b. Both the compressive strength and elastic modulus decreases proportionately with the increase of temperature. The compressive strength decreases from 28.34 ± 1.25 kPa at 1000 °C to 20.14 ± 3.54 kPa at 1300 °C. The elastic modulus decreases from 227.57 ± 24.72 kPa at 1000 °C to 151.82 ± 24.77 kPa at 1300 °C. In other words, the compressive strength and elastic modulus decrease 28.93 ± 0.23% and 33.29 ± 1.61% respectively in the temperature range 1000 °C to 1300 °C. Such decreasing trend of mechanical properties can be attributed to the grain size of the materials. The grain size of WC and W increases with the temperature as shown in Figure 4.9c. According to the Hall-Petch equation, the mechanical properties of metals decrease with the increase in the grain size. The Hall-Petch equation is also valid for ceramic material with a grain size larger than 15 nm [239,240]. Furthermore, there is a significant amount of carbon of amorphous nature present in the Miura-ori samples, especially in the fibers of the inner layers as mentioned in Chapter 2. The mechanical properties of amorphous carbon also decrease with increasing temperature [241,242]. However, it should be noted that the standard deviation in both compressive strength and elastic modulus is significantly high. Such high standard deviation is attributed to the random distribution of the constituent fibers and high standard deviation in the fiber diameter.

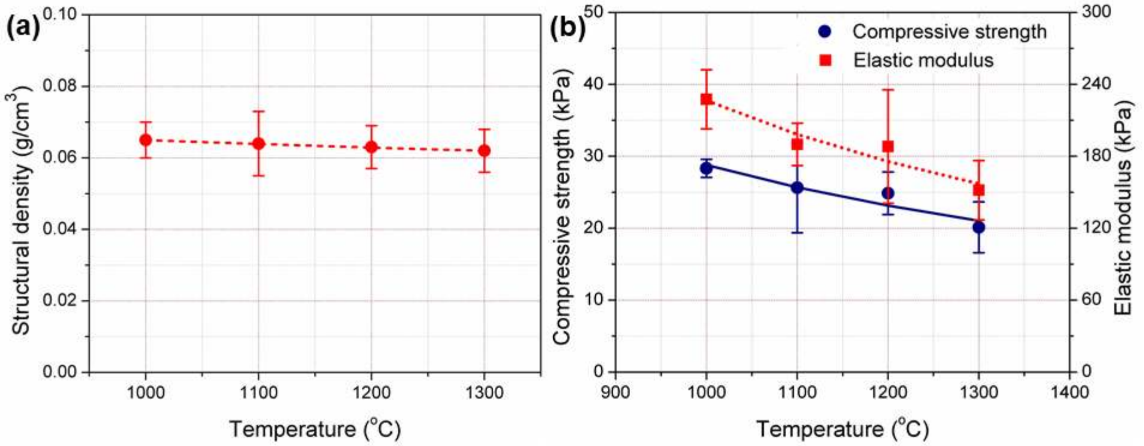

Figure 4.11: (a) Structural density of the Miura-ori samples obtained at different temperatures. (b) Compressive strength and elastic modulus of the Miura-ori samples heat-treated at different temperature. A Miura-ori folded from a flat piece of paper featuring area of 3" X 3" was used here. The Miura-ori samples were infiltrated with 20% AMT solution. The heat treatment was performed in vacuum environment using a heating rate of 2.5 °C/min. At least 4 experiments were performed for each data point. The error bar represents the standard deviation in the measurement.

4.2.2.2. Effect of size of the WC Miura-ori on structural density and mechanical properties

The structural density and the mechanical properties were also characterized for different sizes of Miura-ori. To characterize the effect of different sizes, we performed the heat treatment using the optimum synthesis conditions i.e. synthesis temperature of 1300 °C, heating rate of 2.5 °C/min and 20% AMT concentration. As we obtain WC as the main material at these conditions, we refer the Miura-ori samples obtained using these synthesis conditions as WC Miura-ori.

The structural density of the WC Miura-ori was plotted in Figure 4.12a for different lengths of design parameter *h* of a Miura-ori unit cell. The density of the WC Miura-ori decreases from 0.108 ± 0.015 g/cm^3 to 0.052 ± 0.006 g/cm^3 as *h* increases from 6.12 mm to 10.71 mm. The density of the WC Miura-ori obtained ranges from 0.33% to 0.7% of the density of bulk WC (15.63 g/cm^3) [243].

Figure 4.12b and 4.12c show the compressive strength (σ_c) and the elastic modulus (E) of the WC Miura-ori samples. The σ_c ranges from 8.49 kPa to 44.47 kPa, and E ranges from 38 kPa to 293 kPa. In comparison, the compression strength and elastic modulus of bulk WC ranges from 3.3 to 6.8 GPa and 600 GPa to 700 GPa respectively [244,245]. The low values of σ_m and E of the WC Miura-ori are attributed to the compositional difference in the outer and inner layer fibers (See Chapter 2), the fiber diameter and the spacing between them [204]. Our hypothesis is a homogeneous WC matrix in all layers of the fibers will improve the mechanical properties of the Miura-ori significantly. Ongoing work is on tuning the synthesis process to achieve a homogeneous WC matrix throughout all the layers of the fibers. Furthermore, the variation in σ_c and E from the mean line as seen in the Figure 4.12b and 4.12c respectively were result of the variation in the fiber diameters in the layers and the random and wide distribution of the open pores as seen in Figure 2.6a.

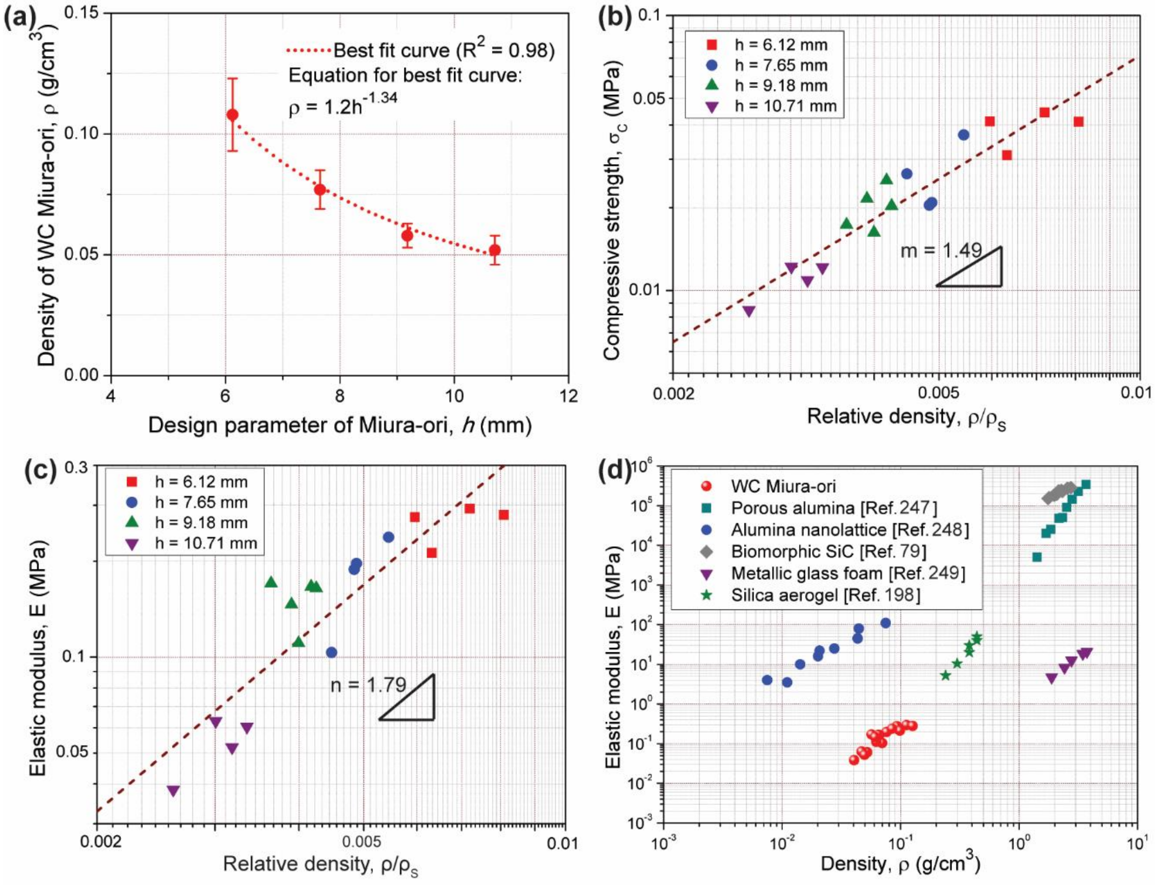

Figure 4.12: (a) The structural density of WC Miura-ori for different sizes. (b) The compressive strength and (c) elastic modulus of the WC Miura-ori with respect to the relative density of the samples. The compressive strength exhibits a scaling of 1.49 and the elastic modulus exhibits a scaling of 1.79. The scaling suggests a bending dominant failure mode of WC Miura-ori. (d) The comparison of the elastic modulus of WC Miura-ori structures with different other ceramic materials.

The compressive strength (σ_c) and elastic modulus (E) of cellular material follows the Ashby and Gibson scaling law as shown below [189]:

$$\sigma_c \propto \sigma_S \left(\frac{\rho}{\rho_S}\right)^m \qquad \text{Equation 4.4}$$

$$E \propto E_S \left(\frac{\rho}{\rho_S}\right)^n \qquad \text{Equation 4.1}$$

where, σ_S, E_S and ρ_S are the compressive strength, elastic modulus and the density of the solid parent material respectively. *m* and *n* are the scaling exponents which represents the failure mode of the material such as bending or stretching. The values of *m* and *n* depend on the microstructure of the material, material composition and geometry of the cellular material which includes cell type (open or closed), geometrical arrangement of the cells and size of the cells [190]. For a stretch dominant material the value of both *m* and *n* is 1, whereas the value of *m* and *n* for a bending dominant material is 1.5 and 2 respectively [189]. As seen from Figure 4.10b and 4.10c, the WC Miura-ori featured an $m = 1.49$ and an $n = 1.79$. Hence, the WC Miura-ori resembles a bending dominant failure under compressive load similar to other open cell cellular material. This was expected as the Miura-ori does not contain any lateral member or panel at its base to carry tensile load, which is an important feature for a stretch dominant cellular structure [195]. However, the scaling of the WC Miura-ori outperforms the traditional lightweight bending dominant cellular materials such as carbon aerogel ($n = 2.7$), carbon nanotube foam ($n = 3$), metallic microlattices ($n = 2.4$) and alumina foam ($n = 4$). Figure 4.12d shows the comparison of the elastic modulus of our WC Miura-ori with other cellular ceramic materials such as porous alumina [246], alumina nanolattices [247], biomorphic silicon carbide [76], metallic glass foam [248], and silica aerogel [197]. It can be clearly seen that other than alumina nanolattice there is no other ceramic materials presently available in the given density range. The elastic modulus of our WC Miura-ori is 100 times lower than that of an octet-truss design made of alumina nanolattices fabricated by Greer and their group [247]. The octet-truss design is a stretch dominant material, which in general is capable of carrying higher load than any bending dominant material. However, we assume obtainment of homogeneous WC matrix in all the layers of the fibers will bring up the mechanical properties comparable to that of the alumina nanolattices.

It should be noted here that the fabrication of alumina nanolattices involves complex and expensive processes such as two photon lithography of the polymer scaffold, atomic layer deposition of the alumina and plasma etching of the polymer. This makes this process highly expensive and difficult for large scale manufacturing of ceramic cellular material. On contrary, WC origami is simple, inexpensive and feasible for large-scale manufacturing. The potential for the large-scale manufacturing is discussed in the section for Carbon origami (See Section 4.1). Similar manufacturing line can be employed for commercial production of carbide origami structure with inclusion of an added step of infiltration. A generalized schematic of the production line is shown in Figure 4.13 for the large-scale manufacturing of carbon and carbide origami structures.

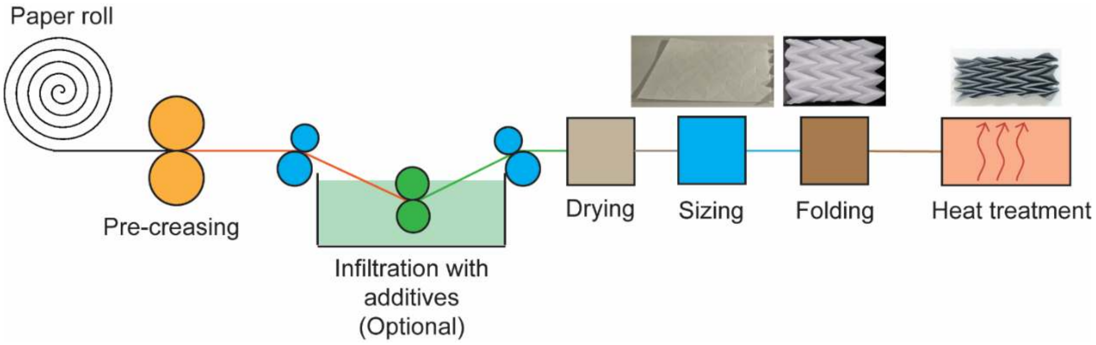

Figure 4.13: Proposed production line for fabrication of WC Miura-ori for large scale manufacturing.

4.2.3. Concluding remarks

In this section, we demonstrated the fabrication of 3D complex shapes of lightweight, cellular WC material using origami techniques. We integrated the synthesis knowledge explored in the Chapter 2 for synthesis of WC from CG paper with the fabrication technique described in the Section 4.1. We characterized the effect of synthesis temperature on the composition, grain size and mechanical properties of the heat-treated Miura-ori samples. With increase in temperature from 1000 °C to 1300 °C, decrease of 28.93 ± 0.23% and 33.29 ± 1.61% were shown in the compressive strength and elastic modulus respectively. This decrease can be attributed to the increase in the grain size with the increase of synthesis temperature. As expected, the WC Miura-ori exhibits a bending dominant failure under compression ($m = 1.49$ and $n = 1.79$). Similar to the carbon origami structures, the WC Miura-ori structures featured low density and low absolute compressive and elastic modulus. Higher mechanical properties are expected upon obtainment of a homogenous WC material throughout the whole cross-section of the Miura-ori. At a low density, the Miura-ori exhibited better elastic modulus than other popular cellular ceramic material at a low density except from alumina nanolattices. However, the processing of WC is simpler, easier and cost effective when compared to the fabrication of alumina nanolattices. Furthermore, WC Miura-ori has an immense potential for large-scale manufacturing when compared to the other cellular ceramic materials.

Similar to the carbon origami structures, WC origami is a preferable candidate for multifunctional material. Further work is necessary here as well to improve the material homogeneity and mechanical properties of the WC origami structures. The use of porous WC is well known for electrochemical applications such catalyst supports [249], fuel cells [94], and oxygen redactors [250]. Furthermore, WC has excellent chemical stability and high oxidation resistance. WC can sustain a temperature up to 400 °C under oxidative conditions [251]. WC origami allows for integrating such excellent material properties of WC with the structural properties of origami structures. Hence, such WC origami structures may find uses in potential applications such as high temperature filters, structural filters in toxic environments, and structural electrodes in different electrochemical devices.

CHAPTER 5: Additive manufacturing of porous tungsten carbide

Additive manufacturing or popularly known as 3D printing is a technology in which three-dimensional objects are made directly from CAD models by layer-upon-layer addition of material. This offers the ability to fabricate more complex geometries when compared to subtractive manufacturing methods. Porous honeycomb structure used for filters in automobile engines is an example that are generally manufactured using molds in the traditional industrial process [39]. Previous work in biopolymer shaping using additive manufacturing includes fabricating tissue to replace damaged human body parts [252]. Several biopolymers have been used for additive manufacturing, such as collagen [253], gelatin [254], and alginate [255].

In this chapter, we present the additive manufacturing of the biopolymer gel composite used in the Chapter 3 for synthesis of porous WC. Bingham plastic nature of the composite allows it to be extruded and printed into various shapes at room temperature. Heat treatment of the 3D printed biopolymer gel composite leads to 3D printed structure of porous WC. Here we detail on the scalability and shrinkage at different stages of the process. Further we study the effect of layer thickness on the mechanical properties of the 3D printed WC structures. Depending on the results obtain here, we lay out a plan for fabricating 3D printed cellular architecture to achieve high specific mechanical properties. We finish the sub-chapter by discussing potential applications of the 3D printed porous WC structures.

5.1. Experimental section

5.1.1. Materials

The water-based biopolymer gel composite (BGC) comprising of iota-carrageenan, chitin and WO_3 nanoparticles is used here as the WC precursor as well as the material for 3D printing. Details of the constituents of the BGC are provided in the Chapter 3. A Taz Lulzbot 5 3D printer along with a Discov3ry paste extruder was used for additive manufacturing of the BGC. The designs for 3D printed parts were created in SolidWorks (Dassault Systems, Waltham, MA, USA). Cura software was chosen to control the parameters of the printer and run the printer. The set up for the 3D printing of the BGC is shown in the Figure 5.1.

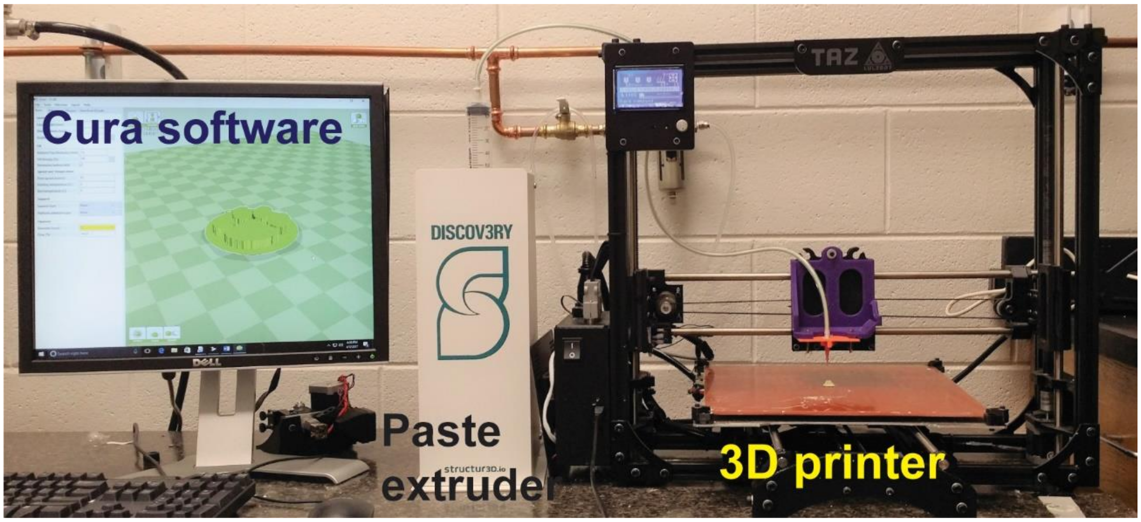

Figure 5.1: The experimental set up for 3D printing of the biopolymer gel composite. The experimental set up includes a 3D printer, a paste extruder and a 3D printing software.

5.1.2. Fabrication protocol

The preparation of the BGC is detailed in the Chapter 3. Briefly, the iota-carrageenan and chitin powders were mixed in a weight ratio of 1:4. WO_3 nanoparticles were added to the biopolymer powder mix to achieve a molar ratio of WO_3:C = 1:6. The biopolymer- metal oxide powder mixture is mixed using a vortex mixture (Thermo Scientific, Maximix M16710-33Q) to obtain a homogenous mixture of the biopolymer-metal oxide nanoparticles. Ultra-pure water was added to the biopolymer-metal oxide nanoparticle mixture and stirred manually using a spatula until a homogeneous gel composite was obtained. The as prepared BCG was put into a 60 mL syringe and inserted into the Discov3ry Paste Extruder that was connected to the printer. Vinyl-Flex (NSF-61) PVC 18-14 (1/8” x 1/4") tubing was attached to the syringe on one end, and a desired nozzle of 1.5 mm diameter was attached to the other end of the tube. The nozzle was then inserted into the holder on the printer.

Using SolidWorks, the designs for 3D printing were created and exported as .stl files, which is the CAD format suitable for 3D printers. The .stl files were imported into the Cura software and adjusted the printing parameters such as nozzle size, printing speed, fill density, and layer thickness. In this work, a print speed of 80 mm/s, a nozzle size of 1.5 mm and a fill density of 100% were used to print the 3D shapes of the BGC. Using a layer thickness of 0.5 mm, cylindrical structures of different sizes were attempted to 3D print. The designed diameter of the cylindrical structures varied from 5 mm to 15 mm. Furthermore, effect of different layer thicknesses ranging from 0.25 mm to 1 mm was investigated on the WC parts obtained from the BCG. To do so, cylindrical structures featuring a designed diameter of 15 mm were printed with different layer thicknesses. All the cylindrical structures designed in this work featured an aspect ratio of 1. An alumina substrate was used for 3D printing of the BGC.

After printing a design using desired printing parameters, the sample was left to dry at room temperature for a minimum of 48 hours to obtain a BGC xerogel. The BGC xerogel was heat treated in a nitrogen atmosphere for 3 hours at 1300 °C in a tube furnace (TF1700, Across International, USA) to obtain a 3D printed WC structure.

5.1.3. Characterization

Measurements were taken of each of the fabricated sample, BGC xerogel and heat-treated samples using the Dino-Lite Digital Microscope (Product number: AM4815ZT). The shrinkage was calculated using the Equation 5.1. The heat-treated sample was characterized by X-ray diffraction (XRD) spectroscopy (Rigaku Ultima IV, Japan) to confirm the formation of WC during the heat treatment. The structural density was calculated by the ratio of the mass of the heat-treated sample and the volume occupied by the heat-treated sample. The compression tests of the 3D printed WC structures were performed at a rate of 1 mm/min to 80% strain using an Instron Single Column Testing System (Model 5944). A load cell of 50 N was used for the compression tests. We calculated the elastic modulus (E) from the slope of the elastic region of the stress-strain curve obtained during the compression test. The highest value obtained in the elastic region of the stress-strain curve was considered as the compressive strength (σ) of the 3D printed structures.

$$Shrinkage\ (\%)$$
$$= \frac{Fabricated\ dimension - Dimension\ of\ xerogel\ or\ WC\ part}{Fabricated\ dimension} \times 100\%$$

Equation 5.1

5.2. Results and discussions

5.2.1. Fabrication results

Figure 5.2a-c shows an example of the 3D printed cylindrical structure of BGC, BGC xerogel and heat-treated xerogel respectively. It can be seen from Figure 5.2a-c that a significant shrinkage occurred during the drying and heat treatment process. The shrinkage occurred in BGC xerogel is due to the evaporation of the water from the gel composite. The escape of the volatile byproducts generated during the carbonization, and the carbothermal reduction reaction results in the shrinkage in the heat-treated samples. As reported in the Chapter 3, WC is main material present in the heat-treated samples. This is further confirmed here by the XRD pattern of the heat-treated BGC xerogel sample (Figure 5.2d). The microstructural properties of the WC are detailed in the Chapter 3. Briefly, the synthesized WC features a porous network of agglomerated WC grains. The average grain size of WC is 20.15 ± 4.99 nm and it features a BET surface area of 67.03 m^2/g.

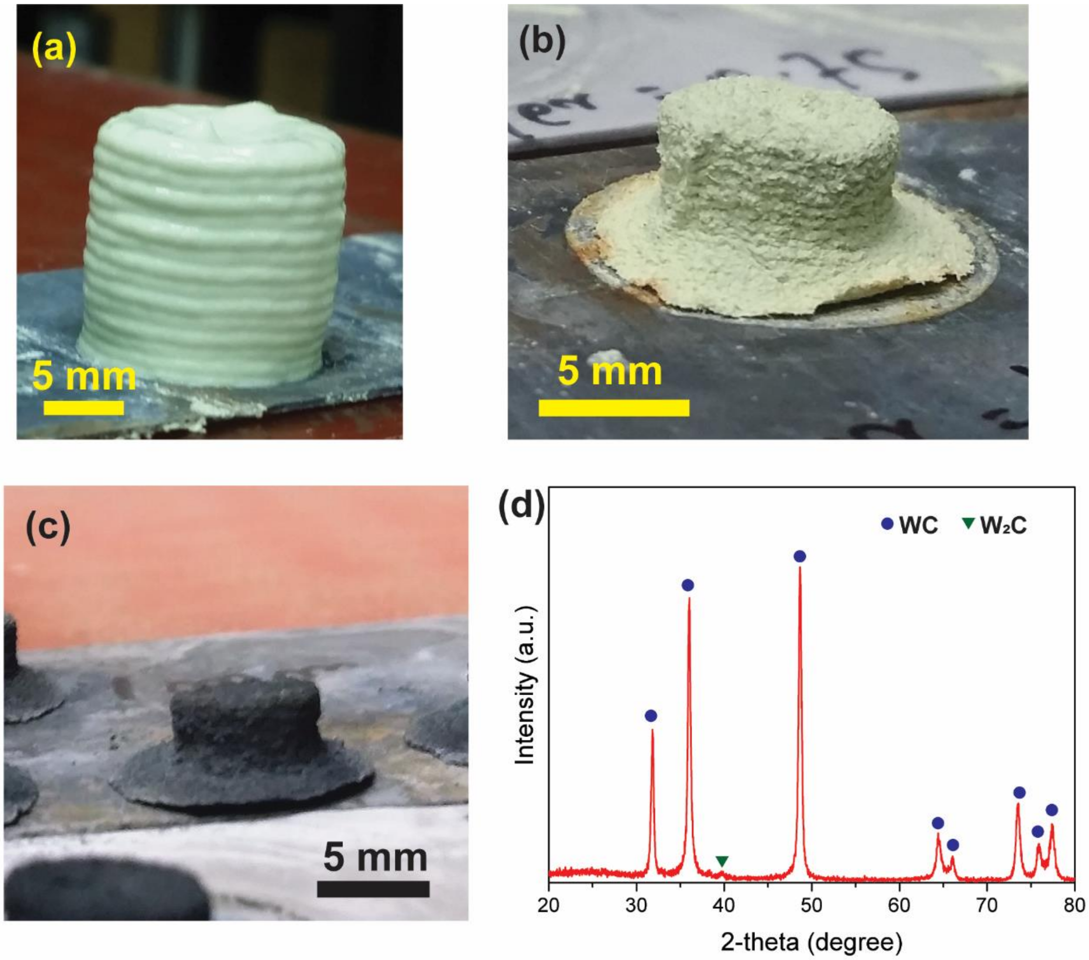

Figure 5.2: (a) Example of a cylindrical structure fabricated by 3D printing of the biopolymer gel composite. (b) Xerogel obtained after natural drying of the 3D printed biopolymer gel composite. (c) The cylindrical structure of WC obtained by heat treatment of the xerogel at 1300 °C in nitrogen environment. (d) XRD pattern of the heat-treated sample confirming the formation of WC in the heat treatment process.

Figure 5.3a and 5.3b show the data points for the measurements of diameter and height respectively for 3D printed BGC, BGC xerogel and WC samples. The data points referred to as failures in the figure reflect the challenge to obtain geometries with characteristic dimension less than 5 mm. The BGC comes out of the nozzle continuously during the 3D printing. Hence, as the 3D printing progresses in the vertical direction, the BGC tries to drag the material deposited earlier. Here if the base material is strongly adhered to the substrate, the impact of the dragging becomes insignificant. However, for smaller base area, the overall adherence strength is much weaker. Hence, during printing at an elevated height, the material dragging force overcomes the adherence strength at the base and fails the printing process. Therefore, 3D printing of the cylindrical structures with a dimension of 5 mm was not successful here. However, a cylindrical structure having 5 mm diameter but an aspect ratio <1 may be successful. Ongoing work is to characterize the scalability in 3D printing of different structures with a varying aspect ratio. The structures with a dimension higher than 5 mm exhibits a 3D printed dimension close to the designed dimension. Our hypothesis is the deviation of the 3D printed dimension from the designed dimension can be attributed to the use of a relatively large nozzle size. Smaller nozzle size will improve the preciseness of the fabricated dimensions. However, smaller nozzle size is more prone to clogging, which fails the 3D printing process. As mentioned earlier, shrinkage occurs for both BGC xerogel and WC structures. Around 48% shrinkage occurred in the diameter of the cylindrical structures during this drying process, whereas the shrinkage in height was around 58%. We hypothesize that the use of water as the gel forming solvent is responsible for such difference in the shrinkage of dimeter and height. The water tends to pull down the deposited BGC because of its high density, which in result increases shortens the height and fattens the diameter. This phenomenon is reflected in the xerogel dimensions showing a higher shrinkage in height than diameter. However, further study is needed to validate this hypothesis. Additional 10% shrinkage occurred during the heat treatment for both the diameter and height.

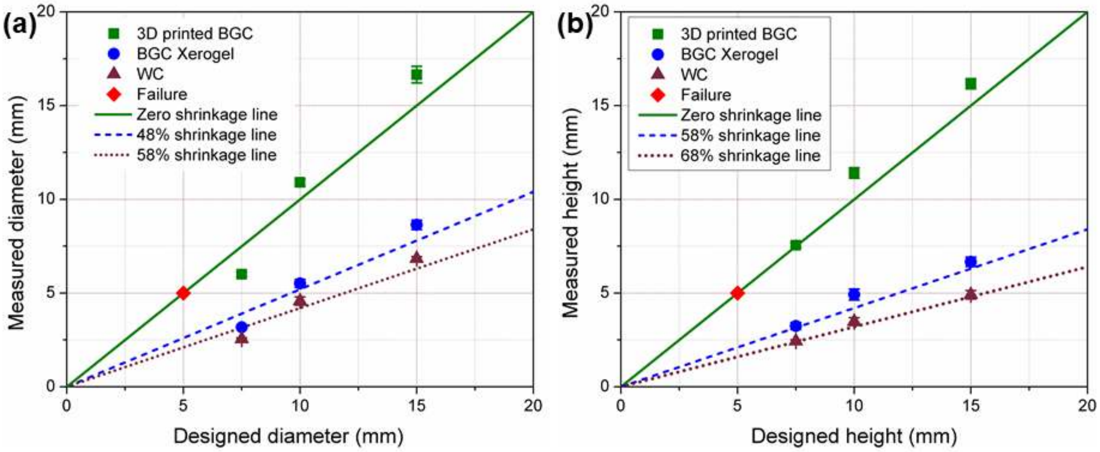

Figure 5.3: The results of the 3D printing of different sizes of cylindrical structures in terms of their (a) diameter and (b) height showing the shrinkage occurred in the case of BGC xerogel and WC with respect to the designed dimensions.

5.2.2. Effect of layer thickness on the mechanical properties of the 3D printed WC

Fill density and layer thickness are the two most important parameters, which are responsible for the mechanical properties of 3D printed parts [256]. Here in this work, we characterized the effect of layer thickness on the structural density and the mechanical properties of the 3D printed WC cylindrical structures. 100% fill density was used for 3D printing of the cylindrical features. The results are presented in the Figure 5.4. No change was observed in the structural density of the 3D printed WC parts with the change of layer thickness. This is because net volume of the cylindrical structures does not change with the layer thickness. Further, the layer thickness only changes the number of layers required to achieve a specific height of the part. Although, the amount of material deposited for each layer is different for different layer thickness, the net amount of material required to build a specific structure remains almost same for different layer thickness. Hence, the density of the structure remains unchanged irrespective of the layer thickness. The constant density the 3D printed structures featured was around 0.48 g/cm^3, which is only 3% of the density of bulk WC material (density of WC =15.72 g/cm^3 [4]).

As expected, the layer thickness has a significant impact on the elastic modulus and compressive strength. For an increase in the fabricated layer thickness from 0.25 mm to 1mm, the elastic modulus increases from 2.02 ± 0.31 MPa to 3.22 ± 0.45 MPa and the compressive strength increases from 196.34 ± 38.16 kPa to 477.89 ± 3.7 kPa. This is because with increasing layer thickness, each layer feature higher homogeneity which leads to uniform molecular bonding strength. This results in higher resistance to the compressive stress, leading to higher mechanical properties [257]. However, the molecular bond strength increases with the decrease in the layer thickness below a certain layer thickness. Hence, below that threshold layer thickness, the mechanical properties of the 3D printed parts are expected to increase with decreasing layer thickness [257]. In general practice, lower layer thickness is desired in 3D printed parts to minimize the surface roughness generated by the stacking of the layers. Furthermore, lower layer thickness yields to a better dimensional accuracy of the 3D printed part [258].

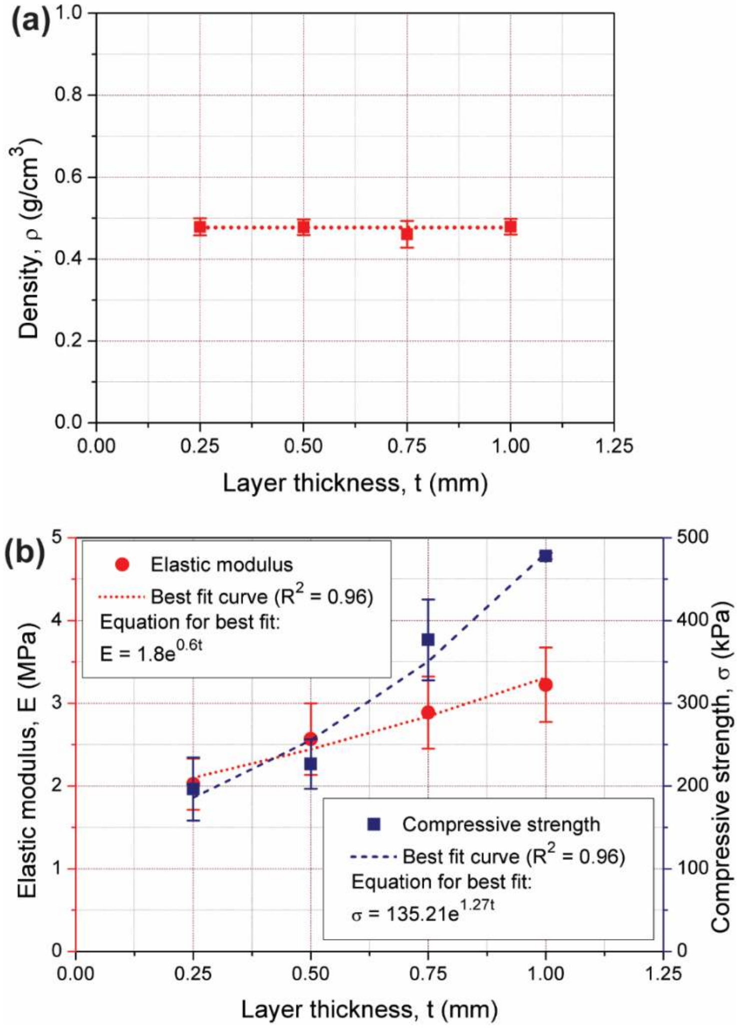

Figure 5.4: (a) Effect of layer thickness on the density (ρ) of the 3D printed WC cylindrical structures. The layer thickness does not have any effect on the density of the 3D printed WC material. (b) Effect of the layer thickness on the elastic modulus (E) and compressive strength (σ) of the 3D printed WC cylindrical structures. The error bars represent standard deviation in the measurement. At least 3 experiments were performed for each data point.

Based on the results obtained here for solid cylindrical structures, future work will include fabrication of lightweight cellular structures of porous WC which can exhibit high mechanical properties at a low structural density. This work will include the study the impact of 3D printing of BGC for different cellular structures featuring varying number of nodes and varying width of each strut. A design of experiment will be implemented to understand the effect of the parameters of the nodal geometry such as number of nodes, strut width, and thickness on the mechanical properties of the 3D printed WC structures.

5.3. Concluding remarks and practical challenges

Here we presented the fabrication of 3D shapes of porous WC by additive manufacturing of a biopolymer gel composite following by natural drying and heat treatment in inert atmosphere at 1300 °C. The drying and heat treatment result in a significant shrinkage of the 3D printed parts because of evaporation of the water and escape of volatile byproducts respectively. As expected, the layer thickness of the 3D printed part has a strong impact on the mechanical properties of the 3D printed part. The mechanical properties increase with the increase in the layer thickness. However, larger layer thickness is not desired in 3D printing to minimize the surface roughness and achieve a better dimensional accuracy of the fabricated part.

Theoretically, numerous complex shapes can be fabricated in additive manufacturing. Few examples of different other complex shapes of 3D printed WC are shown in the Figure 5.5.

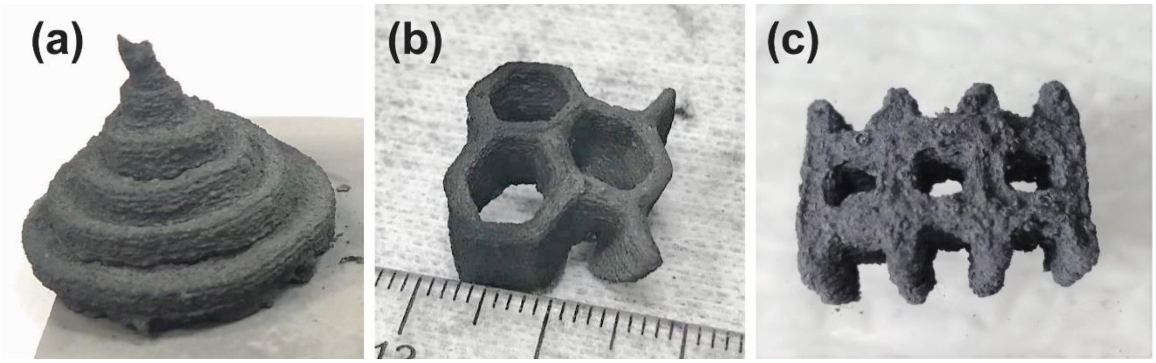

Figure 5.5: Different complex shapes fabricated by the 3D printing of WC. (a) A stepped cylindrical structure of 3D printed WC. (b) A hexagonal honeycomb structure of 3D printed WC. (c) A rectangular honeycomb structure of 3D printed WC.

However, our system has several limitations in the shape complexity. One of the important limitation is inability to fabricate overhangs and suspended structures. As water is used here as the gel forming solvent, it makes the gel relatively heavy. Because of this, the material deposited to print an overhang or suspended feature falls due to absence of any support structure and fails the attempt to fabricate overhang structure. It is challenging to fabricate high aspect ratio inclined trusses due to the same reason. Possible solution is to replace water as the gel forming solvent by another solvent featuring a low density and a considerable solubility in water. In that case, it might be possible to fabricate overhang and suspended structures and high aspect ratio inclined trusses. However, long overhangs or suspended structures will not be possible in this system without using any support structures, which is a limitation of deposition based additive manufacturing system [259].

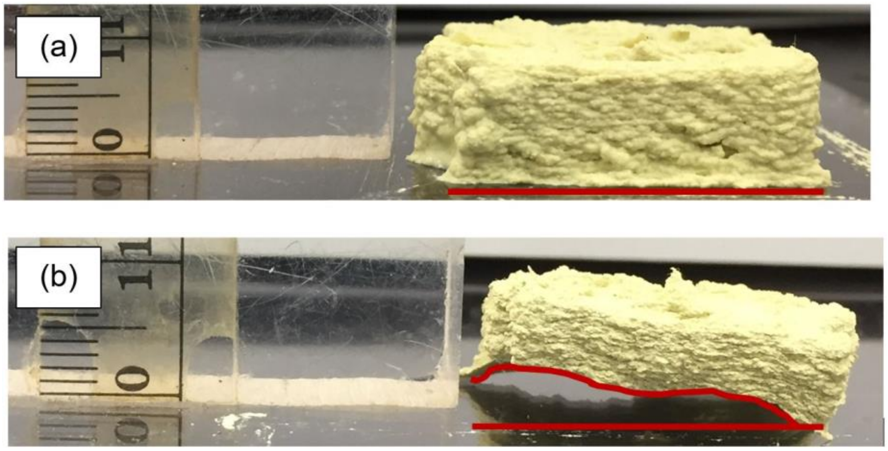

Figure 5.6: (a) 3D printed sample showing no deviation between the structure's foundation and the horizontal substrate; (b) Xerogel obtained after natural drying of the 3D printed gel composite showing the concave deformation that occurred during the drying process. This is indicated by deviation between the outline of the structure's foundation and the horizontal substrate.

The substrate used for the 3D printing has an important role on the final shape of the 3D printed structures. In Figure 5.2b, a larger diameter was achieved at the base of the structure in the BGC xerogel, when an alumina substrate was used. Such larger base diameter was further replicated in the WC structures. This is because the alumina substrate features larger grain size and rough surface finish, which enhances the adherence of BGC with the substrate [258]. The higher adherence restricts the shrinkage of structure at the base during the drying process, resulting in larger diameter on the base. A different phenomenon occurred when a polycarbonate substrate was used. A concave deformation at the base was observed after drying of the 3D printed BGC as seen in Figure 5.6b. This deformation may have been due to the surface tension of the gel on the polycarbonate substrate. The contact angle after fabrication in Figure 5.6a appeared to be perpendicular. Hence, the concave shape at the base drying suggests that the post-fabrication contact angle should have been obtuse for the sample to rise to a perpendicular orientation once the solvent had evaporated. Further study is needed to fully understand the causes of the deformation with respect to printing substrate and material solvent.

The 3D printed WC structures can be useful as a candidate for multifunctional material. Further work is necessary here as well to solve the issues with the shape complexities. However, porous WC has shown to perform remarkably in different electrochemical applications such catalyst supports [249], fuel cells [94], and oxygen redactors [250]. Furthermore, WC has excellent chemical stability and high oxidation resistance. WC can sustain a temperature up to 500 °C under oxidative conditions [251]. Integrating such interesting material properties with the freedom of fabricating 3D complex shapes makes 3D printed WC structures a suitable candidate in different applications such as lightweight structural material, structural electrodes in electrochemical applications and filters for harsh environments.

CONCLUSION AND FUTURE WORK

The dissertation has presented an origami-inspired manufacturing and an additive manufacturing platform for the fabrication of 3D complex shapes of porous carbides using different biopolymer precursors. The origami inspired manufacturing used a pure cellulosic chromatography paper due to its ability to be creased and folded into different 3D origami shapes. A water-based gel composite featuring iota-carrageenan, chitin and WO_3 nanoparticles was used to fabricate the 3D parts in the additive manufacturing platform, which utilized the capability of layer-by-layer deposition of the gel composite. Use of the biopolymeric precursors has been demonstrated for the first time to fabricate 3D complex shapes of carbide materials. The methodology used here to obtain the 3D shapes of porous WC from the biopolymers was: (1) infiltrate the biopolymer with tungsten precursor, (2) shape the tungsten precursor infiltrated biopolymer using origami or additive manufacturing depends on the biopolymer form, and (3) heat treatment of the 3D shapes of the precursor materials to obtain porous WC. The porous WC obtained after the heat treatment retained the 3D shapes of the precursor materials, although a significant shrinkage occurred. The shrinkage depends on the precursor material as well as the geometry of the 3D parts. This biopolymeric route affords several advantages: (1) Carrageenan, chitin and cellulose are three of the most abundant biopolymers in the nature. Till now, the use of these abundant biopolymers has been limited to mostly food processing, pharmaceutical and cosmetic industries. Here for the first time, these biopolymers were used for production of engineering ceramic materials, which expands use of these abundant biopolymers. (2) The use of the biopolymers yielded a synthesis temperature of 1300 °C to obtain a WC with a purity >96%. This is advantageous when compared to a temperature >1400 °C required in the industrial synthesis approaches. (3) The biopolymers yielded a WC grain size ranging from 20 nm to 60 nm, which is advantageous when compared to a grain size >100 nm obtained in the industrial production of WC.

The origami-inspired manufacturing has been demonstrated here, for the first time, for the fabrication of 3D complex shapes of carbonaceous materials including carbon and WC. The method presented here expands the horizon of the versatile origami-inspired manufacturing. The 3D origami shapes of the carbon and WC fabricated here featured low density. For example, both carbon and WC Miura-ori fabricated here featured a density less than 1% of the density of bulk glassy carbon and WC respectively. Although the absolute value of the mechanical properties of the carbon and WC Miura-ori samples were significantly lower than their corresponding bulk monolithic material, they exhibit advantageous scaling of the elastic modulus with the density when compared to other lightweight cellular materials. Another advantage of the origami-inspired manufacturing over the fabrication methods of other lightweight cellular materials is its immense potential for large-scale manufacturing using the existent industrial infrastructure.

The main contribution for the additive manufacturing is the fabrication of a 3D shape of porous WC which starts with 3D printing of a biopolymer gel composite. The technique presented here integrates, for the first time, the knowledge of 3D printing of a gel-like material to the synthesis of a carbide material. The cylindrical structures of porous WC fabricated in the additive manufacturing platform featured a density <3% of the density of bulk WC material. The effect of layer thickness was characterized here on the mechanical properties of the 3D printed porous WC material when a 100% fill density was used for 3D printing. The elastic modulus and compressive strength exhibited an increasing trend with the increase in layer thickness. However, the additive manufacturing process exhibited deformability of the final shape of WC parts, which was mainly attributed to the use of water as the solvent material. The future work includes replacement of the water with an alternative solvent material to form the precursor gel which can felicitate fabrication of cellular architectures for achieving higher mechanical properties at a low structural density.

The manufacturing techniques presented here marry the interesting material properties of porous WC with the structural properties of the 3D architecture. This makes these 3D structures of porous WC a suitable candidate for multifunctional material. For example, WC exhibits high chemical inertness in corrosive environment. Hence, the 3D architecture of the porous WC can be used as a structural filter material in harsh environments. Other potential applications of the 3D architectures of porous WC include structural batteries and capacitors, high temperature filters and lightweight structural material.

The work presented in this dissertation opens different directions for future work. The future works from this dissertation need to be addressed are:

(1) The proposed applications of the 3D shapes of the porous carbide shapes need to be validated experimentally. For example, the impact of the 3D architectures needs to be characterized in terms of their electrochemical properties such as capacitance, electrochemical sensitivity and areal current density over a porous WC film or WC

powders. This will validate the application of the 3D shapes of the porous carbide as a suitable candidate for structural batteries and fuel cells.

(2) The design parameters of a 3D architecture have a significant role on the mechanical properties of the 3D architecture. A parametrical study is needed to exploit the design parameters of the 3D architectures to achieve a higher mechanical properties/weight ratio.

(3) Although the elastic modulus and compressive strength of the 3D shapes of porous carbide materials were characterized in this dissertation, the behavior of the porous carbide under compressive load is still not well understood at the microstructural level. For example, in case of an origami structure, it is currently unknown what happens to the constituent fibers under compressive load. Do the fibers slips over each other to accommodate the compressive strain or break immediately? Do the fibers break at the grain boundaries or break randomly? What is impact of the spatial distribution of the fibers in terms of the load distribution under compressive stress? Hence, it is important to understand these microstructural behaviors to understand the macrostructural properties of the 3D shapes. Future work includes study of the microstructural behavior under compression and build a numerical model based on the study. This model will help to predict the mechanical properties of a 3D shape, when WC with different porous microstructure will be used to fabricate the 3D shape.

(4) The heat treatment process itself is still under investigation. For example, how different heating parameters such as temperature, heating rate, heating environment and cooling rate will affect the structural deformability and shrinkage of the 3D structures is still not well understood. The orientation of the 3D shapes inside the furnace during the heat treatment

process has also shown to have significant impact on the density of the 3D shapes. The explanation is not clear for such cases. Hence, extensive studies are needed to understand effect of the heat treatment conditions on the 3D shapes of the carbide materials.

BIBLIOGRAPHY

[1] N.A. Fleck, V.S. Deshpande, M.F. Ashby, Micro-architectured materials: past, present and future, Proc. R. Soc. A Math. Phys. Eng. Sci. 466 (2010) 2495–2516. doi:10.1098/rspa.2010.0215.

[2] J.H. Lee, J.P. Singer, E.L. Thomas, Micro-/nanostructured mechanical metamaterials, Adv. Mater. 24 (2012) 4782–4810. doi:10.1002/adma.201201644.

[3] A.A. Zadpoor, Mechanical meta-materials, Mater. Horiz. (2016). doi:10.1039/C6MH00065G.

[4] Y. Zhong, X. Xia, F. Shi, J. Zhan, J. Tu, H.J. Fan, Transition Metal Carbides and Nitrides in Energy Storage and Conversion, Adv. Sci. 3 (2016) 1500286. doi:10.1002/advs.201500286.

[5] J.S. Lee, S.H. Lee, S.C. Choi, Improvement of porous silicon carbide filters by growth of silicon carbide nanowires using a modified carbothermal reduction process, J. Alloys Compd. 467 (2009) 543–549. doi:10.1016/j.jallcom.2007.12.042.

[6] N. Ji, T. Zhang, M. Zheng, A. Wang, H. Wang, X. Wang, J.G. Chen, Direct catalytic conversion of cellulose into ethylene glycol using nickel-promoted tungsten carbide catalysts, Angew. Chemie - Int. Ed. 47 (2008) 8510–8513. doi:10.1002/anie.200803233.

[7] J. Patt, D. Moon, C. Phillips, L. Thompson, Molybdenum carbide catalysts for

water–gas shift, Catal. Letters. 65 (2000) 193–195. doi:10.1023/a:1019098112056.

[8] Z. Chen, D. Higgins, A. Yu, L. Zhang, J. Zhang, A review on non-precious metal electrocatalysts for PEM fuel cells, Energy Environ. Sci. 4 (2011) 3167. doi:10.1039/c0ee00558d.

[9] M. Naguib, J. Halim, J. Lu, K.M. Cook, L. Hultman, Y. Gogotsi, M.W. Barsoum, New two-dimensional niobium and vanadium carbides as promising materials for li-ion batteries, J. Am. Chem. Soc. 135 (2013) 15966–15969. doi:10.1021/ja405735d.

[10] M. Naguib, J. Come, B. Dyatkin, V. Presser, P.L. Taberna, P. Simon, M.W. Barsoum, Y. Gogotsi, MXene: A promising transition metal carbide anode for lithium-ion batteries, Electrochem. Commun. 16 (2012) 61–64. doi:10.1016/j.elecom.2012.01.002.

[11] D. Garg, P.N. Dyer, Tungsten Carbide Erosion Resistant Coating for Aerospace Components, Mater. Res. Soc. Proc. 168 (1989) 213.

[12] F. Li, Z. Kang, X. Huang, X.G. Wang, G.J. Zhang, Preparation of zirconium carbide foam by direct foaming method, J. Eur. Ceram. Soc. 34 (2014) 3513–3520. doi:10.1016/j.jeurceramsoc.2014.05.029.

[13] J.H. Eom, Y.W. Kim, I.H. Song, H.D. Kim, Processing and properties of polysiloxane-derived porous silicon carbide ceramics using hollow microspheres as templates, J. Eur. Ceram. Soc. 28 (2008) 1029–1035.

doi:10.1016/j.jeurceramsoc.2007.09.009.

[14] L. Borchardt, C. Hoffmann, M. Oschatz, L. Mammitzsch, U. Petasch, M. Herrmann, S. Kaskel, Preparation and application of cellular and nanoporous carbides, Chem. Soc. Rev. 41 (2012) 5053. doi:10.1039/c2cs15324f.

[15] J. Barker, M.Y. Saidi, J.L. Swoyer, A Carbothermal Reduction Method for the Preparation of Electroactive Materials for Lithium Ion Applications, J. Electrochem. Soc. 150 (2003) A684. doi:10.1149/1.1568936.

[16] X. Guo, L. Zhu, W. Li, H. Yang, Preparation of SiC powders by carbothermal reduction with bamboo charcoal as renewable carbon source, J. Adv. Ceram. 2 (2013) 128–134. doi:10.1007/s40145-013-0050-4.

[17] J. Wang, R. Ishida, T. Takarada, Carbothermal reactions of quartz and kaolinite with coal char, Energy and Fuels. 14 (2000) 1108–1114. doi:10.1021/ef000084x.

[18] C. Czosnek, J.F. Janik, Z. Olejniczak, Silicon carbide modified carbon materials. Formation of nanocrystalline SiC from thermochemical processes in the system coal tar pitch/poly(carbosilane), J. Clust. Sci. 13 (2002) 487–502. doi:10.1023/A:1021171511204.

[19] a. Alizadeh, E. Taheri-Nassaj, N. Ehsani, Synthesis of boron carbide powder by a carbothermic reduction method, J. Eur. Ceram. Soc. 24 (2004) 3227–3234. doi:10.1016/j.jeurceramsoc.2003.11.012.

[20] M. Narisawa, H. Yasuda, R. Mori, H. Mabuchi, K. Oka, Y.-W. Kim, Silicon

carbide particle formation from carbon black — polymethylsilsesquioxane mixtures with melt pressing, J. Ceram. Soc. Japan. 116 (2008) 121–125.

[21] N.Z. Muradov, T.N. Veziroğlu, From hydrocarbon to hydrogen-carbon to hydrogen economy, Int. J. Hydrogen Energy. 30 (2005) 225–237. doi:10.1016/j.ijhydene.2004.03.033.

[22] T.A. Ruble, Carbon Black from Petroleum Oil, in: Refin. Pet. Chem., ACS Publication, Houston, TX, 1970: pp. 264–270.

[23] U.S. Energy Information Administration, How much oil is consumed in the United States?, (2016). https://www.eia.gov/tools/faqs/faq.cfm?id=33&t=6.

[24] D.E. Nicodem, M.C.Z. Fernandes, C.L.B. Guedes, R.J. Correa, Photochemical processes and the environmental impact of petroleum spills, Biogeochemistry. 39 (1997) 121–138. doi:10.1023/A:1005802027380.

[25] M. Fingas, B. Fieldhouse, Studies on crude oil and petroleum product emulsions: Water resolution and rheology, Colloids Surfaces A Physicochem. Eng. Asp. 333 (2009) 67–81. doi:10.1016/j.colsurfa.2008.09.029.

[26] W. Thompson, J. Whistance, S. Meyer, Effects of US biofuel policies on US and world petroleum product markets with consequences for greenhouse gas emissions, Energy Policy. 39 (2011) 5509–5518. doi:10.1016/j.enpol.2011.05.011.

[27] L.H. Dudte, E. Vouga, T. Tachi, L. Mahadevan, Programming curvature using origami tessellations, Nat. Mater. 15 (2016) 583–588. doi:10.1038/nmat4540.

[28] D. Dureisseix, An Overview of Mechanisms and Patterns with Origami, Int. J. Sp. Struct. 27 (2012) 1–14. doi:10.1260/0266-3511.27.1.1.

[29] A. Lebée, From folds to structures, a review, Int. J. Sp. Struct. 30 (2015) 55–74. doi:10.1260/0266-3511.30.2.55.

[30] Robert J Lang, Origami : Complexity in Creases (Again), Engineering&Science. 1 (2004) 8–19.

[31] M. Schenk, S.D. Guest, Origami 5: Fifth International Meeting of Origami Science, Mathematics, and Education, CRC Press, 2011.

[32] M. Eidini, G.H. Paulino, Unravelling Metamaterial Properties in Zigzag-base Folded, Sci. Adv. 1 (2015) 1–8. doi:10.1126/sciadv.1500224.

[33] E.T. Filipov, T. Tachi, G.H. Paulino, Origami tubes assembled into stiff, yet reconfigurable structures and metamaterials., Proc. Natl. Acad. Sci. U. S. A. 112 (2015) 12321–12326. doi:10.1073/pnas.1509465112.

[34] J.L. Silverberg, A.A. Evans, L. McLeod, R.C. Hayward, T. Hull, C.D. Santangelo, I. Cohen, Applied origami. Using origami design principles to fold reprogrammable mechanical metamaterials., Science. 345 (2014) 647–50. doi:10.1126/science.1252876.

[35] J.T.B. Overvelde, T.A. de Jong, Y. Shevchenko, S.A. Becerra, G.M. Whitesides, J.C. Weaver, C. Hoberman, K. Bertoldi, A three-dimensional actuated origami-inspired transformable metamaterial with multiple degrees of freedom, Nat.

Commun. 7 (2016) 10929. doi:10.1038/ncomms10929.

[36] K.C. Cheung, T. Tachi, S. Calisch, K. Miura, Origami interleaved tube cellular materials, Smart Mater. Struct. 23 (2014) 94012. doi:10.1088/0964-1726/23/9/094012.

[37] J.T.B. Overvelde, J.C. Weaver, C. Hoberman, K. Bertoldi, Rational design of reconfigurable prismatic architected materials, Nature. 541 (2017) 347–352. doi:10.1038/nature20824.

[38] S.J.P. Callens, A.A. Zadpoor, From flat sheets to curved geometries: Origami and kirigami approaches, Mater. Today. xx (2017). doi:10.1016/j.mattod.2017.10.004.

[39] N. Guo, M.C. Leu, Additive manufacturing: Technology, applications and research needs, Front. Mech. Eng. 8 (2013) 215–243. doi:10.1007/s11465-013-0248-8.

[40] K. Naruse, K. Tajima, Method for Manufacturing Material for Silicon Carbide Fired Body and Method for Manufacturing Honeycomb Structure, US 2008/0284067A1, 2008.

[41] K. V. Wong, A. Hernandez, A Review of Additive Manufacturing, ISRN Mech. Eng. 2012 (2012) 1–10. doi:10.5402/2012/208760.

[42] R. Sreenivasan, A. Goel, D.L. Bourell, Sustainability issues in laser-based additive manufacturing, Phys. Procedia. 5 (2010) 81–90. doi:10.1016/j.phpro.2010.08.124.

[43] A.R. Mohamed, M. Mohammadi, G.N. Darzi, Preparation of carbon molecular sieve from lignocellulosic biomass: A review, Renew. Sustain. Energy Rev. 14

(2010) 1591–1599. doi:10.1016/j.rser.2010.01.024.

[44] J.A. Libra, K.S. Ro, C. Kammann, A. Funke, N.D. Berge, Y. Neubauer, M.-M. Titirici, C. Fühner, O. Bens, J. Kern, K.-H. Emmerich, Hydrothermal carbonization of biomass residuals: a comparative review of the chemistry, processes and applications of wet and dry pyrolysis, Biofuels. 2 (2011) 71–106. doi:10.4155/bfs.10.81.

[45] R.D. Perlack, L.L. Wright, A.F. Turhollow, R.L. Graham, B.J. Stokes, D.C. Erbach, Biomass as a feedstock for a bioenergy and bioproducts industry: the technical feasibility of a billion-ton annual supply, 2005.

[46] D. Valderrama, J. Cai, N. Hishamunda, N. Ridler, Social and economic dimensions of carrageenan seaweed farming: a global synthesis, 2013.

[47] Z. Schnepp, S.C. Wimbush, M. Antonietti, C. Giordano, Synthesis of highly magnetic iron carbide nanoparticles via a biopolymer route, Chem. Mater. 22 (2010) 5340–5344. doi:10.1021/cm101746z.

[48] T. Ota, M. Takahashi, T. Hibi, M. Ozawa, S. Suzuki, Y. Hikichi, H. Suzuki, Biomimetic process for producing SiC "wood," J. Am. Ceram. Soc. 78 (1995) 3409–3411.

[49] C. Giordano, C. Erpen, W. Yao, B. Milke, M. Antonietti, Metal nitride and metal carbide nanoparticles by a soft urea pathway, Chem. Mater. 21 (2009) 5136–5144. doi:10.1021/cm9018953.

[50] J.P. Murray, A. Steinfeld, E.A. Fletcher, Metals, nitrides, and carbides via solar carbothermal reduction of metal oxides, Energy. 20 (1995) 695–704. doi:10.1016/0360-5442(95)00032-C.

[51] Y. Shin, X.S. Li, C. Wang, J.R. Coleman, G.J. Exarhos, Synthesis of hierarchical titanium carbide from titania-coated cellulose paper, Adv. Mater. 16 (2004) 1212–1215. doi:10.1002/adma.200306661.

[52] C. Ma, N. Brandon, G. Li, Preparation and formation mechanism of hollow microspherical tungsten carbide with mesoporosity, J. Phys. Chem. C. 111 (2007) 9504–9508. doi:10.1021/jp072378q.

[53] M. Islam, R. Martinez-Duarte, A sustainable approach for tungsten carbide synthesis using renewable biopolymers, Ceram. Int. 43 (2017) 10546–10553. doi:10.1016/j.ceramint.2017.05.118.

[54] D.S. Venables, M.E. Brown, Reduction of tungsten oxides with carbon . Part 2 . Tube furnace experiments, Thermochim. Acta. 283 (1996) 265–276.

[55] D.S. Venables, M.E. Brown, Reduction of tungsten oxides with carbon . Part 1 . Thermal analysis, Thermochim. Acta. 283 (1996) 251–264.

[56] P. Hoier, Effect of Carbon Sources and Carbonaceous Atmospheres on the Effective Synthesis of Nanostructured Tungsten Carbide Powders, Chalmers University of Technology, 2014.

[57] D.S. Venables, M.E. Brown, Reduction of tungsten oxide with carbon monooxide,

Thermochim. Acta. 291 (1997) 131–140.

[58] R. Koc, S.K. Kodambaka, Tungsten carbide (WC) synthesis from novel precursors, J. Eur. Ceram. Soc. 20 (2000) 1859–1869. doi:10.1016/S0955-2219(00)00038-8.

[59] J.H. Eom, Y.W. Kim, S. Raju, Processing and properties of macroporous silicon carbide ceramics: A review, J. Asian Ceram. Soc. 1 (2013) 220–242. doi:10.1016/j.jascer.2013.07.003.

[60] M. Fukushima, P. Colombo, Silicon carbide-based foams from direct blowing of polycarbosilane, J. Eur. Ceram. Soc. 32 (2012) 503–510. doi:10.1016/j.jeurceramsoc.2011.09.009.

[61] K. Wang, Y. Wang, Z. Liang, Y. Liang, D. Wu, S. Song, P. Tsiakaras, Ordered mesoporous tungsten carbide/carbon composites promoted Pt catalyst with high activity and stability for methanol electrooxidation, Appl. Catal. B Environ. 147 (2014) 518–525. doi:10.1016/j.apcatb.2013.09.020.

[62] N. Muhammad, Z. Man, M.I.A. Mutalib, M.A. Bustam, C.D. Wilfred, A.S. Khan, Z. Ullah, G. Gonfa, A. Nasrullah, Dissolution and Separation of Wood Biopolymers Using Ionic Liquids, ChemBioEng Rev. 2 (2015) 257–278. doi:10.1002/cben.201500003.

[63] C.I. Czimczik, C.M. Preston, M.W.I. Schmidt, R.A. Werner, E.D. Schulze, Effects of charring on mass, organic carbon, and stable carbon isotope composition of

wood, Org. Geochem. 33 (2002) 1207–1223. doi:10.1016/S0146-6380(02)00137-7.

[64] T. Ota, M. Takahshi, T. Hibi, M. Ozawa, S. Suzuki, Y. Hikichi, Biomimetic process for producing SiC "wood," J. Am. Ceram. Soc. 78 (1995) 3409–3411.

[65] J. Qian, J. Wang, Z. Jin, Preparation of biomorphic SiC ceramic by carbothermal reduction of oak wood charcoal, Mater. Sci. Eng. A. 371 (2004) 229–235. doi:10.1016/j.msea.2003.11.051.

[66] P. Greil, Biomorphous ceramics from lignocellulosics, J. Eur. Ceram. Soc. 21 (2001) 105–118. doi:10.1016/S0955-2219(00)00179-5.

[67] L.. and K.A. 4. Greil.P, Biomorphic cellular silicon carbide ceramic from wood:I Processing and Microstructure II Mechanical Properties, J.Eur.Ceram.Soc. 18 (1998) 1961–1975. doi:10.1016/S0955-2219(98)00155-1.

[68] F.M. Varela-Feria, J. Martínez-Fernández, a.R de Arellano-López, M. Singh, Low density biomorphic silicon carbide: microstructure and mechanical properties, J. Eur. Ceram. Soc. 22 (2002) 2719–2725. doi:10.1016/S0955-2219(02)00137-1.

[69] T.L.Y. Cheung, D.H.L. Ng, Conversion of Bamboo to biomorphic composites containing silica and silicon carbide nanowires, J. Am. Ceram. Soc. 90 (2007) 559–564. doi:10.1111/j.1551-2916.2006.01390.x.

[70] H. Sieber, C. Zollfrank, N. Popovska, D. Almeida, H. Gerhard, Gas phase processing of porous, biomorphic TiC-Ceramics, Key Eng. Mater. 264 (2004)

2227–2230.

[71] C.R. Rambo, J. Cao, O. Rusina, H. Sieber, Manufacturing of biomorphic (Si,Ti,Zr)-carbide ceramics by sol–gel processing, Carbon N. Y. 43 (2005) 1174–1183. doi:10.1016/j.carbon.2004.12.009.

[72] C. Giordano, C. Erpen, W. Yao, B. Milke, M. Antonietti, Metal nitride and metal carbide nanoparticles by a soft urea pathway, Chem. Mater. 21 (2009) 5136–5144. doi:10.1021/cm9018953.

[73] C. Giordano, C. Erpen, W. Yao, M. Antonietti, Synthesis of Mo and W carbide and nitride nanoparticles via a simple "urea glass" route, Nano Lett. 8 (2008) 4659–4663. doi:10.1021/nl8018593.

[74] M.W.R. Holgate, T. Schoberl, S.R. Hall, A novel route for the synthesis of nanocomposite tungsten carbide-cobalt using a biopolymer as a carbon source, J. Sol-Gel Sci. Technol. 49 (2009) 145–149. doi:10.1007/s10971-008-1869-y.

[75] N. Patra, D.D. Jayaseelan, W.E. Lee, Synthesis of Biopolymer-Derived Zirconium Carbide Powder by Facile One-Pot Reaction, J. Am. Ceram. Soc. 98 (2015) 71–77. doi:10.1111/jace.13321.

[76] M. Singh, J. a. Salem, Mechanical properties and microstructure of biomorphic silicon carbide ceramics fabricated from wood precursors, J. Eur. Ceram. Soc. 22 (2002) 2709–2717. doi:10.1016/S0955-2219(02)00136-X.

[77] K. Tsukada, Porous silicon carbide and its production, 4,777, 152, 1988.

[78] C. Duong-Viet, H. Ba, Z. El-Berrichi, J.-M. Nhut, M.J. Ledoux, Y. Liu, C. Pham-Huu, Silicon carbide foam as a porous support platform for catalytic applications, New J. Chem. 40 (2016) 4285–4299. doi:10.1039/C5NJ02847G.

[79] E. Vogli, J. Mukerji, C. Hoffman, R. Kladny, H. Sieber, P. Greil, Conversion of Oak to Cellular Silicon Carbide Ceramic by Gas-Phase Reaction with Silicon Monoxide, J. Am. Ceram. Soc. 84 (2004) 1236–1240. doi:10.1111/j.1151-2916.2001.tb00822.x.

[80] P. Nguyen, C. Pham, Innovative porous SiC-based materials: From nanoscopic understandings to tunable carriers serving catalytic needs, Appl. Catal. A Gen. 391 (2011) 443–454. doi:10.1016/j.apcata.2010.07.054.

[81] M. Henriksson, L. a. Berglund, Structure and properties of cellulose nanocomposite films containing melamine formaldehyde, J. Appl. Polym. Sci. 106 (2007) 2817–2824. doi:10.1002/app.26946.

[82] I. Siró, D. Plackett, Microfibrillated cellulose and new nanocomposite materials: a review, Cellulose. 17 (2010) 459–494. doi:10.1007/s10570-010-9405-y.

[83] F.X. Collard, J. Blin, A review on pyrolysis of biomass constituents: Mechanisms and composition of the products obtained from the conversion of cellulose, hemicelluloses and lignin, Renew. Sustain. Energy Rev. 38 (2014) 594–608. doi:10.1016/j.rser.2014.06.013.

[84] H.B. Goyal, D. Seal, R.C. Saxena, Bio-fuels from thermochemical conversion of

renewable resources: A review, Renew. Sustain. Energy Rev. 12 (2008) 504–517. doi:10.1016/j.rser.2006.07.014.

[85] S.J. Cameron, F. Hosseinian, Potential of flaxseed in the development of omega-3 rice paper with antioxidant activity, LWT - Food Sci. Technol. 53 (2013) 170–175. doi:10.1016/j.lwt.2012.12.004.

[86] A. Buléon, P. Colonna, V. Planchot, S. Ball, Starch granules: Structure and biosynthesis, Int. J. Biol. Macromol. 23 (1998) 85–112. doi:10.1016/S0141-8130(98)00040-3.

[87] and A.D. De´borah Le Corre, Julien Bras, Starch Nanoparticles : A Review, Biomacromolecules. 11 (2010) 1139–1153.

[88] D.S.C. Caccamisi, Cassava: Global Production and Market Trends, Chron. Horticult. 50 (2010) 15–18.

[89] C. Ververis, K. Georghiou, N. Christodoulakis, P. Santas, R. Santas, Fiber dimensions, lignin and cellulose content of various plant materials and their suitability for paper production, Ind. Crops Prod. 19 (2004) 245–254. doi:10.1016/j.indcrop.2003.10.006.

[90] C. Marulier, P.J.J. Dumont, L. Org??as, S. Rolland du Roscoat, D. Caillerie, 3D analysis of paper microstructures at the scale of fibres and bonds, Cellulose. 22 (2015) 1517–1539. doi:10.1007/s10570-015-0610-6.

[91] M. Iguchi, S. Yamanaka, a. Budhiono, Bacterial cellulose - a masterpiece of

nature's arts, J. Mater. Sci. 35 (2000) 261–270. doi:10.1023/A:1004775229149.

[92] L.F. Chen, Z.H. Huang, H.W. Liang, H.L. Gao, S.H. Yu, Three-dimensional heteroatom-doped carbon nanofiber networks derived from bacterial cellulose for supercapacitors, Adv. Funct. Mater. 24 (2014) 5104–5111. doi:10.1002/adfm.201400590.

[93] S. Park, J.O. Baker, M.E. Himmel, P.A. Parilla, D.K. Johnson, Cellulose crystallinity index: Measurement techniques and their impact on interpreting cellulase performance, Biotechnol. Biofuels. 3 (2010) 1–10. doi:10.1186/1754-6834-3-10.

[94] J.P. Bosco, K. Sasaki, M. Sadakane, W. Ueda, J.G. Chen, Synthesis and characterization of three-dimensionally ordered macroporous (3DOM) tungsten carbide: Application to direct methanol fuel cells, Chem. Mater. 22 (2010) 966–973. doi:10.1021/cm901855y.

[95] H. Chhina, S. Campbell, O. Kesler, High surface area synthesis, electrochemical activity, and stability of tungsten carbide supported Pt during oxygen reduction in proton exchange membrane fuel cells, J. Power Sources. 179 (2008) 50–59. doi:10.1016/j.jpowsour.2007.12.105.

[96] R. Ganesan, J.S. Lee, Tungsten carbide microspheres as a noble-metal-economic electrocatalyst for methanol oxidation, Angew. Chemie - Int. Ed. 44 (2005) 6557–6560. doi:10.1002/anie.200501272.

[97] R. Ganesan, D.J. Ham, J.S. Lee, Platinized mesoporous tungsten carbide for electrochemical methanol oxidation, Electrochem. Commun. 9 (2007) 2576–2579. doi:10.1016/j.elecom.2007.08.002.

[98] L. Alexander, H.P. Klug, Determination of crystallite size with the x-ray spectrometer, J. Appl. Phys. 21 (1950) 137–142. doi:10.1063/1.1699612.

[99] D. Shen, R. Xiao, S. Gu, H. Zhang, The Overview of Thermal Decomposition of Cellulose in Lignocellulosic Biomass, in: Cellul. - Biomass Convers., 2013: pp. 193–226. doi:10.5772/51883.

[100] S. Li, J. Lyons-Hart, J. Banyasz, K. Shafer, Real-time evolved gas analysis by FTIR method: An experimental study of cellulose pyrolysis, Fuel. 80 (2001) 1809–1817. doi:10.1016/S0016-2361(01)00064-3.

[101] M. Ul-Islam, T. Khan, J.K. Park, Water holding and release properties of bacterial cellulose obtained by in situ and ex situ modification, Carbohydr. Polym. 88 (2012) 596–603. doi:10.1016/j.carbpol.2012.01.006.

[102] I.M.G. Martins, S.P. Magina, L. Oliveira, C.S.R. Freire, A.J.D. Silvestre, C.P. Neto, A. Gandini, New biocomposites based on thermoplastic starch and bacterial cellulose, Compos. Sci. Technol. 69 (2009) 2163–2168. doi:10.1016/j.compscitech.2009.05.012.

[103] A. Vazquez, M.L. Foresti, P. Cerrutti, M. Galvagno, Bacterial Cellulose from Simple and Low Cost Production Media by Gluconacetobacter xylinus, J. Polym.

Environ. 21 (2013) 545–554. doi:10.1007/s10924-012-0541-3.

[104] D. Klemm, B. Heublein, H.P. Fink, A. Bohn, Cellulose: Fascinating biopolymer and sustainable raw material, Angew. Chemie - Int. Ed. 44 (2005) 3358–3393. doi:10.1002/anie.200460587.

[105] M. Islam, J. Flach, R. Martinez-Duarte, Carbon Origami: A Method to Fabricate Lightweight Carbon Cellular Materials, Carbon N. Y. 133 (2018) 140–149. doi:10.1016/j.carbon.2018.03.033.

[106] C.F. De Souza, N. Lucyszyn, M.A. Woehl, I.C. Riegel-Vidotti, R. Borsali, M.R. Sierakowski, Property evaluations of dry-cast reconstituted bacterial cellulose/tamarind xyloglucan biocomposites, Carbohydr. Polym. 93 (2013) 144–153. doi:10.1016/j.carbpol.2012.04.062.

[107] T. Ke, X. Sun, Effects of moisture content and heat treatment on the physical properties of starch and poly (lactic acid) blends, J. Appl. Polym. Sci. 81 (2001) 3069–3082. doi:10.1002/app.1758.

[108] M. MB, Y. MJ, K. TJ, K. EG, I. US, Y. MK, W. DJ, Characterization and thermomechanical properties of thermoplastic potato starch, J. Eng. Technol. 2 (2013) 9–16.

[109] X.Y. Liu, M. Huang, H.L. Ma, Z.Q. Zhang, J.M. Gao, Y.L. Zhu, X.J. Han, X.Y. Guo, Preparation of a carbon-based solid acid catalyst by sulfonating activated carbon in a chemical reduction process, Molecules. 15 (2010) 7188–7196.

doi:10.3390/molecules15107188.

[110] V. Palmre, E. Lust, A. Jänes, M. Koel, A.-L. Peikolainen, J. Torop, U. Johanson, A. Aabloo, Electroactive polymer actuators with carbon aerogel electrodes, J. Mater. Chem. 21 (2011) 2577. doi:10.1039/c0jm01729a.

[111] J.G. Li, C.Y. Tsai, S.W. Kuo, Fabrication and characterization of inorganic silver and palladium nanostructures within hexagonal cylindrical channels of mesoporous carbon, Polymers (Basel). 6 (2014) 1794–1809. doi:10.3390/polym6061794.

[112] Z.A.C. Schnepp, S.C. Wimbush, S. Mann, S.R. Hall, Structural evolution of superconductor nanowires in biopolymer gels, Adv. Mater. 20 (2008) 1782–1786. doi:10.1002/adma.200702679.

[113] T. Ishii, K. Yamada, N. Osuga, Y. Imashiro, J.I. Ozaki, Single-Step Synthesis of W2C Nanoparticle-Dispersed Carbon Electrocatalysts for Hydrogen Evolution Reactions Utilizing Phosphate Groups on Carbon Edge Sites, ACS Omega. 1 (2016) 689–695. doi:10.1021/acsomega.6b00179.

[114] M. Sakaki, M.S. Bafghi, J. Vahdati Khaki, Q. Zhang, F. Saito, Conversion of W2C to WC phase during mechano-chemical synthesis of nano-size WC-Al2O3 powder using WO3-2Al-(1 + x)C mixtures, Int. J. Refract. Met. Hard Mater. 36 (2013) 116–121. doi:10.1016/j.ijrmhm.2012.08.002.

[115] D. Klemm, D. Schumann, U. Udhardt, S. Marsch, Bacterial synthesized

cellulose—artificial blood vessels for microsurgery, Prog. Polym. Sci. 26 (2001) 1561–1603. doi:10.1016/S0079-6700(01)00021-1.

[116] X. Chang, D. Chen, X. Jiao, Starch-derived carbon aerogels with high-performance for sorption of cationic dyes, Polymer (Guildf). 51 (2010) 3801–3807. doi:10.1016/j.polymer.2010.06.018.

[117] E.D. Kirby, A PARAMETER DESIGN STUDY IN A TURNING by, Technol. Interface. Fall (2006) 1–14.

[118] Z.Z. Fang, X. Wang, T. Ryu, K.S. Hwang, H.Y. Sohn, Synthesis, sintering, and mechanical properties of nanocrystalline cemented tungsten carbide - A review, Int. J. Refract. Met. Hard Mater. 27 (2009) 288–299. doi:10.1016/j.ijrmhm.2008.07.011.

[119] L.A. Stanciu, V.Y. Kodash, J.R. Groza, Effects of heating rate on densification and grain growth during field-assisted sintering of α-Al2O3 and MoSi2 powders, Metall. Mater. Trans. A. 32 (2001) 2633–2638. doi:10.1007/s11661-001-0053-6.

[120] B.N. Kim, K. Hiraga, K. Morita, H. Yoshida, Effects of heating rate on microstructure and transparency of spark-plasma-sintered alumina, J. Eur. Ceram. Soc. 29 (2009) 323–327. doi:10.1016/j.jeurceramsoc.2008.03.015.

[121] T.E. Kim, K.E. Khishigbayar, K.Y. Cho, Effect of heating rate on the properties of silicon carbide fiber with chemical-vapor-cured polycarbosilane fiber, J. Adv. Ceram. 6 (2017) 59–66. doi:10.1007/s40145-017-0218-4.

[122] M. Nie, P.K. Shen, Z. Wei, Q. Li, H. Bi, C. Liang, Preparation of Pure Tungsten Carbide and Catalytic Activity of Platinum on a Tungsten Carbide Nanocrystalline Support for Oxygen Reduction, ECS Electrochem. Lett. 1 (2012) H11–H13. doi:10.1149/2.004203eel.

[123] N.K. Mathur, C.K. Narang, Chitin and chitosan, versatile polysaccharides from marine animals, J. Chem. Educ. 67 (1990) 938. doi:10.1021/ed067p938.

[124] A. Bartkowiak, D. Hunkeler, Carrageenan-oligochitosan microcapsules: Optimization of the formation process, Colloids Surfaces B Biointerfaces. 21 (2001) 285–298. doi:10.1016/S0927-7765(00)00211-3.

[125] N. Keller, B. Pietruszka, V. Keller, A new one-dimensional tungsten carbide nanostructured material, Mater. Lett. 60 (2006) 1774–1777. doi:10.1016/j.matlet.2005.12.017.

[126] L. Zeng, C. Qin, L. Wang, W. Li, Volatile compounds formed from the pyrolysis of chitosan, Carbohydr. Polym. 83 (2011) 1553–1557. doi:10.1016/j.carbpol.2010.10.007.

[127] J.W. Rhim, L.F. Wang, Preparation and characterization of carrageenan-based nanocomposite films reinforced with clay mineral and silver nanoparticles, Appl. Clay Sci. 97–98 (2014) 174–181. doi:10.1016/j.clay.2014.05.025.

[128] E. Raymundo-Piñero, M. Cadek, F. Béguin, Tuning Carbon Materials for Supercapacitors by Direct Pyrolysis of Seaweeds, Adv. Funct. Mater. 19 (2009)

1032–1039. doi:10.1002/adfm.200801057.

[129] A. Ilnicka, M. Walczyk, J.P. Lukaszewicz, The fungicidal properties of the carbon materials obtained from chitin and chitosan promoted by copper salts, Mater. Sci. Eng. C. 52 (2015) 31–36. doi:10.1016/j.msec.2015.03.037.

[130] Y. Qiao, S. Chen, Y. Liu, H. Sun, S. Jia, J. Shi, C. Marcus, Y. Wang, X. Hou, Pyrolysis of chitin biomass : TG – MS analysis and solid char residue characterization, Carbohydr. Polym. 133 (2015) 163–170. doi:10.1016/j.carbpol.2015.07.005.

[131] Y. Gao, X. Chen, J. Zhang, N. Yan, Chitin-Derived Mesoporous, Nitrogen-Containing Carbon for Heavy-Metal Removal and Styrene Epoxidation, Chempluschem. 80 (2015) 1556–1564. doi:10.1002/cplu.201500293.

[132] S.F. Soares, T. Trindade, A.L. Daniel-Da-Silva, Carrageenan-Silica Hybrid Nanoparticles Prepared by a Non-Emulsion Method, Eur. J. Inorg. Chem. 2015 (2015) 4588–4594. doi:10.1002/ejic.201500450.

[133] J.L. Shamshina, G. Gurau, L.E. Block, L.K. Hansen, C. Dingee, A. Walters, R.D. Rogers, Chitin–calcium alginate composite fibers for wound care dressings spun from ionic liquid solution, J. Mater. Chem. B. 2 (2014) 3924. doi:10.1039/c4tb00329b.

[134] R. Koc, S.K. Kodambaka, Tungsten carbide (WC) synthesis from novel precursors, J. Eur. Ceram. Soc. 20 (2000) 1859–1869.

[135] M.J. Hudson, J.W. Peckett, P.J.F. Harris, Low-Temperature Sol - Gel Preparation of Ordered Nanoparticles of Tungsten Carbide / Oxide, (2005) 5575–5578.

[136] G. Leclercq, M. Kamal, J.M. Giraudon, P. Devassine, L. Feigenbaum, L. Leclercq, A. Frennet, J.M. Bastin, A. Lofberg, S. Decker, M. Dufour, Study of the preparation of bulk powder tungsten carbides by temperature programmed reaction with CH4+H2 mixtures, J. Catal. 158 (1996) 142–169. doi:10.1006/jcat.1996.0015.

[137] V. Richter, M. Ruthendorf, On hardness and toughness of ultra ® ne and nanocrystalline hard materials, Int. J. Refract. Met. Hard Mater. 17 (2000) 141–152.

[138] D.J. McHugh, A Guide to the Seaweed Industry, 2003. doi:ISBN 92-5-104958-0.

[139] K. Gopalan Nair, A. Dufresne, Crab shell chitin whisker reinforced natural rubber nanocomposites. 1. Processing and swelling behavior, Biomacromolecules. 4 (2003) 657–665. doi:10.1021/bm020127b.

[140] D.H. Bartlette, F. Azam, Chitin, Cholera, and Competence, Science (80-.). 310 (2005) 1775–1778.

[141] R. Gillett, Global study of shrimp fisheries, Fish. Bethesda. 475 (2008) 331 pp.

[142] W. Arbia, L. Arbia, L. Adour, A. Amrane, Chitin extraction from crustacean shells using biological methods -A review, Food Technol. Biotechnol. 51 (2013) 12–25.

[143] S.L. Wang, T.J. Chang, T.W. Liang, Conversion and degradation of shellfish

wastes by Serratia sp. TKU016 fermentation for the production of enzymes and bioactive materials, Biodegradation. 21 (2010) 321–333. doi:10.1007/s10532-009-9303-x.

[144] G. Hernandez-Carmona, Conventional and alternative technologies for the extraction of algal polysaccharides, 2013. doi:10.1533/9780857098689.3.475.

[145] G.T. Kjartansson, S. Zivanovic, K. Kristbergsson, J. Weiss, Sonication-Assisted Extraction of Chitin from North Atlantic Shrimps (Pandalus borealis), J. Agric. Food Chem. 54 (2006) 5894–5902. doi:10.1021/jf060646w.

[146] S.F. Uy, A.J. Easteal, M.M. Farid, R.B. Keam, G.T. Conner, Seaweed processing using industrial single-mode cavity microwave heating: A preliminary investigation, Carbohydr. Res. 340 (2005) 1357–1364. doi:10.1016/j.carres.2005.02.008.

[147] M.S. Rao, J. Muñoz, W.F. Stevens, Critical factors in chitin production by fermentation of shrimp biowaste, Appl. Microbiol. Biotechnol. 54 (2000) 808–813. doi:10.1007/s002530000449.

[148] Gmelin, Tungsten, Supplement A 5b, in: Gmelin Handb. Inorg. Organomet. Chem., Springer Verlag, Berlin, 1993: pp. 131–154.

[149] OECD SIDS, Tungsten Carbide, 2005.

[150] Y. Wang, S. Song, P.K. Shen, C. Guo, C.M. Li, Nanochain-structured mesoporous tungsten carbide and its superior electrocatalysis, J. Mater. Chem. 19 (2009) 6149.

doi:10.1039/b902744k.

[151] V. Nikolova, I. Nikolov, P. Andreev, V. Najdenov, T. Vitanov, Tungsten carbide-based electrochemical sensors for hydrogen determination in gas mixtures, J. Appl. Electrochem. 30 (2000) 705–710. doi:10.1023/A:1003813210270.

[152] Z. Wu, Y. Yang, D. Gu, Q. Li, D. Feng, Z. Chen, B. Tu, P.A. Webley, D. Zhao, Silica-templated synthesis of ordered mesoporous tungsten carbide/graphitic carbon composites with nanocrystalline walls and high surface areas via a temperature-programmed carburization route, Small. 5 (2009) 2738–2749. doi:10.1002/smll.200900523.

[153] R.J. Lang, Computational Origami: from Flapping Birds to Space Telescopes, Scg 2009. (2009) 159–162. doi:10.1145/1542362.1542363.

[154] D. Pohl, W.D. Wolpert, Engineered spacecraft deployables influenced by nature, SPIE Opt. Eng. Appl. Int. Soc. Opt. Photonics. 7424 (2009) 742408-742408–9. doi:10.1117/12.823960.

[155] X. Guo, H. Li, B.Y. Ahn, E.B. Duoss, K.J. Hsia, J. a Lewis, R.G. Nuzzo, Two- and three-dimensional folding of thin film single-crystalline silicon for photovoltaic power applications., Proc. Natl. Acad. Sci. U. S. A. 106 (2009) 20149–20154. doi:10.1073/pnas.0907390106.

[156] Z. Song, T. Ma, R. Tang, Q. Cheng, X. Wang, D. Krishnaraju, R. Panat, C.K. Chan, H. Yu, H. Jiang, Origami lithium-ion batteries, Nat. Commun. 5 (2014) 1–6.

doi:10.1038/ncomms4140.

[157] I. Nam, G.-P. Kim, S. Park, J.W. Han, J. Yi, All-solid-state, origami-type foldable supercapacitor chips with integrated series circuit analogues, Energy Environ. Sci. 7 (2014) 1095–1102. doi:10.1039/C3EE43175D.

[158] K. Kuribayashi, K. Tsuchiya, Z. You, D. Tomus, M. Umemoto, T. Ito, M. Sasaki, Self-deployable origami stent grafts as a biomedical application of Ni-rich TiNi shape memory alloy foil, Mater. Sci. Eng. A. 419 (2006) 131–137. doi:10.1016/j.msea.2005.12.016.

[159] C.L. Randall, E. Gultepe, D.H. Gracias, Self-folding devices and materials for biomedical applications, Trends Biotechnol. 30 (2012) 138–146. doi:10.1016/j.tibtech.2011.06.013.

[160] S.S. Tolman, I.L. Delimont, L.L. Howell, D.T. Fullwood, Material selection for elastic energy absorption in origami-inspired compliant corrugations, Smart Mater. Struct. 23 (2014) 94010. doi:10.1088/0964-1726/23/9/094010.

[161] E.A. Peraza-Hernandez, D.J. Hartl, R.J. Malak Jr, D.C. Lagoudas, Origami-inspired active structures: a synthesis and review, Smart Mater. Struct. 23 (2014) 94001. doi:10.1088/0964-1726/23/9/094001.

[162] T.E. Benavidez, R. Martinez-Duarte, C.D. Garcia, Analytical methodologies using carbon substrates developed by pyrolysis, Anal. Methods. (2016). doi:10.1039/c6ay00293e.

[163] G.M. Duran, T.E. Benavidez, J.G. Giuliani, A. Rios, C.D. Garcia, Synthesis of CuNP-modified carbon electrodes obtained by pyrolysis of paper, Sensors Actuators, B Chem. 227 (2016) 626–633. doi:10.1016/j.snb.2015.12.093.

[164] J.G. Giuliani, T.E. Benavidez, G.M. Duran, E. Vinogradova, A. Rios, C.D. Garcia, Development and characterization of carbon based electrodes from pyrolyzed paper for biosensing applications, J. Electroanal. Chem. 765 (2016) 8–15. doi:10.1016/j.jelechem.2015.07.055.

[165] T. Tachi, Geometric Considerations for the Design of Rigid Origami Structures, ￼Proceedings Int. Assoc. Shell Spat. Struct. Symp. 2010. 12 (2010) 458–460. doi:10.1016/j.mpaic.2011.07.005.

[166] C. Lv, D. Krishnaraju, G. Konjevod, H. Yu, H. Jiang, Origami based Mechanical Metamaterials., Sci. Rep. 4 (2014) 5979. doi:10.1038/srep05979.

[167] S. Fischer, K. Drechsler, S. Kilchert, A. Johnson, Mechanical tests for foldcore base material properties, Compos. Part A Appl. Sci. Manuf. 40 (2009) 1941–1952. doi:10.1016/j.compositesa.2009.03.005.

[168] H. Yasuda, C. Chong, E.G. Charalampidis, P.G. Kevrekidis, J. Yang, Formation of rarefaction waves in origami-based metamaterials, Phys. Rev. E - Stat. Nonlinear, Soft Matter Phys. 93 (2016) 1–11. doi:10.1103/PhysRevE.93.043004.

[169] S. Heimbs, J. Cichosz, M. Klaus, S. Kilchert, A.F. Johnson, Sandwich structures with textile-reinforced composite foldcores under impact loads, Compos. Struct.

92 (2010) 1485–1497. doi:10.1016/j.compstruct.2009.11.001.

[170] Z.Y. Wei, Z. V. Guo, L. Dudte, H.Y. Liang, L. Mahadevan, Geometric mechanics of periodic pleated origami, Phys. Rev. Lett. 110 (2013) 1–5. doi:10.1103/PhysRevLett.110.215501.

[171] M. Schenk, S.D. Guest, Geometry of Miura-folded metamaterials, Proc. Natl. Acad. Sci. 110 (2013) 3276–3281. doi:10.1073/pnas.1217998110.

[172] K. Miura, Method of packaging and deployment of large membranes in space, 1985.

[173] T. Street, Deployable membranes designed, Philos. Trans. R. Soc. A. 360 (2002) 227–238. doi:10.1098/rsta.2001.0928.

[174] H. Kobayashi, B. Kresling, J.F. V. Vincent, The geometry of unfolding tree leaves, Proc. R. Soc. B Biol. Sci. 265 (1998) 147–154. doi:10.1098/rspb.1998.0276.

[175] M. Ben Amar, F. Jia, Anisotropic growth shapes intestinal tissues during embryogenesis, Proc. Natl. Acad. Sci. 110 (2013) 10525–10530. doi:10.1073/pnas.1217391110.

[176] F. Haas, R.J. Wootton, Two basic mechanisms in insect wing folding, Proc. R. Soc. London B Biol. Sci. 263 (1996) 1651–1658.

[177] C.E. Byrne, D.C. Nagle, Carbonization of Wood for Advanced Materials Applications, Carbon N. Y. 35 (1991) 259–266. doi:10.1016/S0008-6223(96)00136-4.

[178] Y. Liang, D. Wu, R. Fu, Carbon microfibers with hierarchical porous structure from electrospun fiber-like natural biopolymer, Sci. Rep. 3 (2013) 1–5. doi:10.1038/srep01119.

[179] Y. Wang, L. Pham, G.P.S. De Vasconcellos, M. Madou, Fabrication and characterization of micro PEM fuel cells using pyrolyzed carbon current collector plates, J. Power Sources. 195 (2010) 4796–4803. doi:10.1016/j.jpowsour.2010.02.050.

[180] M. Islam, R. Natu, M.F. Larraga-Martinez, R. Martinez-Duarte, Enrichment of diluted cell populations from large sample volumes using 3D carbon-electrode dielectrophoresis, Biomicrofluidics. 10 (2016). doi:10.1063/1.4954310.

[181] M.A. Worsley, S.O. Kucheyev, J.H. Satcher, A. V. Hamza, T.F. Baumann, Mechanically robust and electrically conductive carbon nanotube foams, Appl. Phys. Lett. 94 (2009) 1–4. doi:10.1063/1.3086293.

[182] S.M. Manocha, K. Patel, L.M. Manocha, Development of carbon foam from phenolic resin via template route, Indian J. Eng. Mater. Sci. 17 (2010) 338–342.

[183] S. Callcut, J.C. Knowles, Correlation between structure and compressive strength in a reticulated glass-reinforced hydroxyapatite foam, J. Mater. Sci. Mater. Med. 13 (2002) 485–489. doi:10.1023/A:1014718722710.

[184] A. Celzard, W. Zhao, A. Pizzi, V. Fierro, Mechanical properties of tannin-based rigid foams undergoing compression, Mater. Sci. Eng. A. 527 (2010) 4438–4446.

doi:10.1016/j.msea.2010.03.091.

[185] O.J.A. Schueller, S.T. Brittain, C. Marzolin, G.M. Whitesides, Fabrication and Characterization of Glassy Carbon MEMS, Chem. Mater. 9 (1997) 1399–1406. http://dx.doi.org/10.1021/cm960639v.

[186] E.E. Hucke, R.A. Fuys, R.G. Craig, Glassy Carbon : A Potential Dental Implant Material, J. Biomed. Mater. Res. Part A. 274 (1973) 263–274.

[187] MatWeb, Vitreous Carbon (Glassy Carbon), (n.d.). http://www.matweb.com/search/datasheet.aspx?matguid=2f4d47d4e39d4091baa8625d4ed46cb1&ckck=1.

[188] M.F. Ashby, D.R.H. Jones, Engineering Materials 2, 4th Editio, Elsevier Butterworth-Heinemann, Waltham, MA, 2013.

[189] M.F. Ashby, The properties of foams and lattices., Philos. Trans. A. Math. Phys. Eng. Sci. 364 (2006) 15–30. doi:10.1098/rsta.2005.1678.

[190] O.M. Istrate, B. Chen, Relative modulus–relative density relationships in low density polymer–clay nanocomposite foams, Soft Matter. 7 (2011) 1840. doi:10.1039/c0sm01052a.

[191] T. a. Schaedler, a. J. Jacobsen, a. Torrents, a. E. Sorensen, J. Lian, J.R. Greer, L. Valdevit, W.B. Carter, Ultralight Metallic Microlattices, Science (80-.). 334 (2011) 962–965. doi:10.1126/science.1211649.

[192] O.J.A. Schueller, S.T. Brittain, G.M. Whitesides, Fabrication of glassy carbon

microstructures by soft lithography, Sensors Actuators A Phys. 72 (1999) 125–139. http://www.sciencedirect.com/science/article/B6THG-3WWKP15-4/2/f3422932275d5954ebd275baad93744c.

[193] A. Szczurek, A. Ortona, L. Ferrari, E. Rezaei, G. Medjahdi, V. Fierro, D. Bychanok, P. Kuzhir, A. Celzard, Carbon periodic cellular architectures, Carbon N. Y. 88 (2015) 70–85. doi:10.1016/j.carbon.2015.02.069.

[194] L.J. Gibson, M.F. Ashby, Cellular solids: Structure and properties, Second Edi, Cambridge University Press, Cambridge, 1997.

[195] X. Zheng, H. Lee, T.H. Weisgraber, M. Shusteff, J. DeOtte, E.B. Duoss, J.D. Kuntz, M.M. Biener, Q. Ge, J. a Jackson, S.O. Kucheyev, N.X. Fang, C.M. Spadaccini, Ultralight, ultrastiff mechanical metamaterials., Science. 344 (2014) 1373–1377. doi:10.1126/science.1252291.

[196] V.S. Deshpande, N.A. Fleck, Collapse of truss core sandwich beams in 3-point bending, Int. J. Solids Struct. 38 (2001) 6275–6305. doi:10.1016/S0020-7683(01)00103-2.

[197] N. Leventis, C. Sotiriou-Leventis, G. Zhang, A.M.M. Rawashdeh, Nanoengineering Strong Silica Aerogels, Nano Lett. 2 (2002) 957–960. doi:10.1021/nl025690e.

[198] R.W. Pekala, C.T. Alviso, J.D. LeMay, Organic aerogels: microstructural dependence of mechanical properties in compression, J. Non. Cryst. Solids. 125

(1990) 67–75. doi:10.1016/0022-3093(90)90324-F.

[199] Z. Qin, G.S. Jung, M.J. Kang, M.J. Buehler, The mechanics and design of a lightweight three-dimensional graphene assembly, Sci. Adv. 3 (2017) 1–8. doi:10.1126/sciadv.160153.

[200] J. Su, A.C. Lua, Effects of carbonisation atmosphere on the structural characteristics and transport properties of carbon membranes prepared from Kapton?? polyimide, J. Memb. Sci. 305 (2007) 263–270.

[201] M.A. Hubbe, R.A. Venditti, O.J. Rojas, What happens to cellulosic fibers during papermaking and recycling? A review, BioResources. 2 (2007) 739–788. doi:10.15376/biores.2.4.739-788.

[202] M. Rasi, Permeability Properties of Paper Materials, University of Jyvaskyla, 2013.

[203] J.H. Gyrres, R. Amiri, D. McDonald, The Specific Pore Volume of Multiplanar Webs: The Role of the Short and Long Fibre Fractions, in: Sci. Papermak. Trans. XIIth Fund. Res. Symp., CF Baker, Oxford, UK, 2001: pp. 1371–1383.

[204] I. Keun Kwon, S. Kidoaki, T. Matsuda, Electrospun nano- to microfiber fabrics made of biodegradable copolyesters: Structural characteristics, mechanical properties and cell adhesion potential, Biomaterials. 26 (2005) 3929–3939. doi:10.1016/j.biomaterials.2004.10.007.

[205] C.L. Pai, M.C. Boyce, G.C. Rutledge, Mechanical properties of individual

electrospun PA 6(3)T fibers and their variation with fiber diameter, Polymer (Guildf). 52 (2011) 2295–2301. doi:10.1016/j.polymer.2011.03.041.

[206] S.S. Munawar, K. Umemura, S. Kawai, Characterization of the morphological, physical, and mechanical properties of seven nonwood plant fiber bundles, J. Wood Sci. 53 (2007) 108–113. doi:10.1007/s10086-006-0836-x.

[207] W.M.A.W. Daud, W.S.W. Ali, M.Z. Sulaiman, Effects of carbonization temperature on pore development in palm-shell-based activated carbon, Carbon N. Y. 38 (2000) 1925–1932. doi:10.1016/S0008-6223(00)00028-2.

[208] J. de D. Lopez-Gonzalez, F. Martinez-Vilchez, F. Rodriguez-Reinoso, J.D.D. Lopez-Gonzalez, Preparation and characterization of active carbons from olive stones., Sect. Title Inorg. Chem. React. 18 (1980) 413–418. doi:10.1016/0008-6223(80)90033-0.

[209] Y. Li, C.T. Lim, M. Kotaki, Study on structural and mechanical properties of porous PLA nanofibers electrospun by channel-based electrospinning system, Polym. (United Kingdom). 56 (2015) 572–580. doi:10.1016/j.polymer.2014.10.073.

[210] W. Li, K. Yang, J. Peng, L. Zhang, S. Guo, H. Xia, Effects of carbonization temperatures on characteristics of porosity in coconut shell chars and activated carbons derived from carbonized coconut shell chars, Ind. Crops Prod. 28 (2008) 190–198. doi:10.1016/j.indcrop.2008.02.012.

[211] Y. Liu, J. Zhou, E. Zhu, J. Tang, X. Liu, W. Tang, Facile synthesis of bacterial cellulose fibres covalently intercalated with graphene oxide by one-step cross-linking for robust supercapacitors, J. Mater. Chem. C. 3 (2015) 1011–1017. doi:10.1039/C4TC01822B.

[212] M. Poletto, V. Pistor, M. Zeni, A.J. Zattera, Crystalline properties and decomposition kinetics of cellulose fibers in wood pulp obtained by two pulping processes, Polym. Degrad. Stab. 96 (2011) 679–685. doi:10.1016/j.polymdegradstab.2010.12.007.

[213] M.S. Mettler, S.H. Mushrif, A.D. Paulsen, A.D. Javadekar, D.G. Vlachos, P.J. Dauenhauer, Revealing pyrolysis chemistry for biofuels production: Conversion of cellulose to furans and small oxygenates, Energy Environ. Sci. 5 (2012) 5414. doi:10.1039/c1ee02743c.

[214] D.K. Shen, S. Gu, The mechanism for thermal decomposition of cellulose and its main products, Bioresour. Technol. 100 (2009) 6496–6504. doi:10.1016/j.biortech.2009.06.095.

[215] M. Iwaki, K. Terashima, Change in atomic density of glassy carbon by Na ion implantation, Surf. Coatings Technol. 128–129 (2000) 429–433.

[216] H. Chen, Biotechnology of lignocellulose: Theory and practice, 2014. doi:10.1007/978-94-007-6898-7.

[217] A. Bejan, Forced convection: Internal flows, in: A. Bejan, A. Kraus (Eds.), Heat

Transf. Handb., John Wiley & Sons, Inc., 2003: pp. 395–438.

[218] B. Dickens, Thermally degrading polyethylene studied by means of factor-jump thermogravimetry, J. Polym. Sci. Polym. Chem. Ed. 20 (1982) 1065–1087.

[219] W.S. Kwon, K.W. Paik, Fundamental understanding of ACF conduction establishment with emphasis on the thermal and mechanical analysis, Int. J. Adhes. Adhes. 24 (2004) 135–142. doi:10.1016/j.ijadhadh.2003.07.003.

[220] A. Gardziella, L.A. Pilato, A. Knop, Phenolic resins- Chemistry, applications, standardization, safety and ecology, Springer Berlin Heidelberg, 2000.

[221] X. Wang, Q. Zhu, S.M. Mahurin, C. Liang, S. Dai, Preparation of free-standing high quality mesoporous carbon membranes, Carbon N. Y. 48 (2010) 557–560. doi:10.1016/j.carbon.2009.09.059.

[222] J. Laine, A. Calafat, M. Labady, Preparation and Characterization of Activated Carbons From Coconut Shell Impregnated With Phosphoric-Acid, Carbon N. Y. 27 (1989) 191–195. doi:10.1016/0008-6223(89)90123-1.

[223] D.H. Page, R.S. Seth, B.D. Jordan, M.C. Barbe, Curl, crimps, kinks and microcompressions in pulp fibres: Their origin, measurement and significance, in: Papermak. Raw Mater. Trans. 8th Fundam. Res. Symp., 1985: pp. 183–227. http://www.ppfrs.org/PageSethJordanBarbe1985.pdf.

[224] A. Namiki, S. Yokosawa, Robotic origami folding with dynamic motion primitives, IEEE Int. Conf. Intell. Robot. Syst. 2015–Decem (2015) 5623–5628.

doi:10.1109/IROS.2015.7354175.

[225] K. Tanaka, Y. Kamotani, Y. Yokokohji, Origami folding by a robotic hand, IEEE Int. Conf. Intell. Robot. Syst. (2007) 2540–2547. doi:10.1109/IROS.2007.4399358.

[226] H. Liu, J. Dai, An approach to carton-folding trajectory planning using dual robotic fingers, Rob. Auton. Syst. 42 (2003) 47–63. doi:10.1016/S0921-8890(02)00312-3.

[227] C. Zhao, Q. Peng, P. Gu, Development of a paper-bag-folding machine using open architecture for adaptability, Proc. Inst. Mech. Eng. Part B J. Eng. Manuf. 229 (2015) 954405414559281. doi:10.1177/0954405414559281.

[228] K.L. Corcoran, CREASE AND EMBOSSING DIE, US 2005/0215405 A1, 2005.

[229] P.W. Jarrett, D.M. Jarrett, ROLLERS FOR CUTTING, CREASING, PERFORATING OR EMBOSSING SHEET MATERIALS, 3,744,384, 1973.

[230] E. Cavagna, DEVICE FOR EMBOSSING AND/OR CREASING SHEET, 0R ROLL MATERIAL, 4,641,575, 1987.

[231] H. Celik, S. Samanli, Ö. Öney, The use of tincal calcination plant waste as an additive in ceramic wall tile production, J. Ceram. Process. Res. 15 (2014) 508–513.

[232] H. Zhuo, Y. Hu, X. Tong, L. Zhong, X. Peng, R. Sun, Sustainable Hierarchical Porous Carbon Aerogel from Cellulose for High-Performance Supercapacitor and

CO_2 Capture, Ind. Crops Prod. 87 (2016) 229–235. doi:10.1016/j.indcrop.2016.04.041.

[233] S. Li, G. Ren, M.N.F. Hoque, Z. Dong, J. Warzywoda, Z. Fan, Carbonized cellulose paper as an effective interlayer in lithium-sulfur batteries, Appl. Surf. Sci. 396 (2017) 637–643. doi:10.1016/j.apsusc.2016.10.208.

[234] J. Cai, H. Niu, Z. Li, Y. Du, P. Cizek, Z. Xie, H. Xiong, T. Lin, High-Performance Supercapacitor Electrode Materials from Cellulose-Derived Carbon Nanofibers, ACS Appl. Mater. Interfaces. 7 (2015) 14946–14953. doi:10.1021/acsami.5b03757.

[235] R. Narasimman, K. Prabhakaran, Preparation of carbon foams with enhanced oxidation resistance by foaming molten sucrose using a boric acid blowing agent, Carbon N. Y. 55 (2013) 305–312. doi:10.1016/j.carbon.2012.12.068.

[236] C. Chen, E.B. Kennel, A.H. Stiller, P.G. Stansberry, J.W. Zondlo, Carbon foam derived from various precursors, Carbon N. Y. 44 (2006) 1535–1543. doi:10.1016/j.carbon.2005.12.021.

[237] T. V Johnson, Diesel Emission Control in Review, SAE Int. 2007-01-0233. 2007 (2007). doi:2007-01-0233.

[238] W.J. Smothers, J.W. Brockmeyer, L.S. Aubrey, Application of Ceramic Foam Filters in Molten Metal Filtration, in: Appl. Refract. Ceram. Eng. Sci. Proc., 1987: pp. 63–74.

[239] H. Ryou, J. Drazin, K. Wahl, S. Qadri, E.P. Gorzkowski, B.N. Feigelson, J.A. Wollmershauser, Below the Hall−Petch Limit in Nanocrystalline, ACS Nano. (2018). doi:10.1021/acsnano.7b07380.

[240] B. Jiang, G.J. Weng, A theory of compressive yield strength of nano-grained ceramics, Int. J. Plast. 20 (2004) 2007–2026. doi:10.1016/j.ijplas.2003.10.010.

[241] A.A. Onoprienko, I.B. Yanchuk, Temperature dependence of the mechanical properties of amorphous carbon films deposited by magnetron sputtering, Powder Metall. Met. Ceram. 45 (2006) 190–195. doi:10.1007/s11106-006-0062-5.

[242] D.A. Czaplewski, J.P. Sullivan, T.A. Friedmann, J.R. Wendt, Temperature dependence of the mechanical properties of tetrahedrally coordinated amorphous carbon thin films, Appl. Phys. Lett. 87 (2005) 1–3. doi:10.1063/1.2108132.

[243] W.-H. Chen, P.K. Nayak, H.-T. Lin, M.-P. Chang, J.-L. Huang, Synthesis of nanostructured tungsten carbide via metal-organic chemical vapor deposition and carburization process, Int. J. Refract. Met. Hard Mater. 47 (2014) 44–48. doi:10.1016/j.ijrmhm.2014.06.015.

[244] AZOMaterials, Tungsten Carbide - An Overview, (2002). https://www.azom.com/properties.aspx?ArticleID=1203.

[245] General Carbide, The designer’s guide to tungsten carbide, (2015) 59. doi:10.1111/j.1365-4632.2011.05422.x.

[246] Z. Deng, T. Fukasawa, Microstructure and mechanical properties of porous

alumina ceramics fabricated by the decomposition of aluminum hydroxide, J. Am. Ceram. Soc. 44 (2001) 2638–2644. doi:10.1111/j.1151-2916.2001.tb01065.x.

[247] L.R. Meza, S. Das, J.R. Greer, Strong, lightweight, and recoverable three-dimensional ceramic nanolattices, Science (80-.). 345 (2014) 1322–1326. doi:10.1126/science.1255908.

[248] J.B. Li, H.C. Lin, J.S.C. Jang, C.N. Kuo, J.C. Huang, Novel open-cell bulk metallic glass foams with promising characteristics, Mater. Lett. 105 (2013) 140–143. doi:10.1016/j.matlet.2013.04.071.

[249] H. Chhina, S. Campbell, O. Kesler, Thermal and electrochemical stability of tungsten carbide catalyst supports, J. Power Sources. 164 (2007) 431–440. doi:10.1016/j.jpowsour.2006.11.003.

[250] Y. Liu, W.E. Mustain, Structural and electrochemical studies of Pt clusters supported on high-surface-area tungsten carbide for oxygen reduction, ACS Catal. 1 (2011) 212–220. doi:10.1021/cs100140s.

[251] S.A. Humphry-Baker, W.E. Lee, Tungsten carbide is more oxidation resistant than tungsten when processed to full density, Scr. Mater. 116 (2016) 67–70. doi:10.1016/j.scriptamat.2016.01.007.

[252] F. Melchels, M. Domingos, T.J. Klein, J. Malda, P.J. Bartolo, D.W. Hutmacher, Additive manufacturing of tissues and organs, Prog. Polym. Sci. 37 (2012) 1079–1104. doi:10.1016/j.progpolymsci.2011.11.007.

[253] R.L. Stewart, M.W. Simpkins, A.M. Kachurin, D. Ph, W.L. Warren, S.K. Williams, Three-Dimensional BioAssembly Tool for Generating Viable Tissue-Engineered Constructs, Tissue Eng. 10 (2004) 1566–1576.

[254] C.X.F. Lam, X.M. Mo, S.H. Teoh, D.W. Hutmacher, Scaffold development using 3D printing with a starch-based polymer, Mater. Sci. Eng. C. 20 (2002) 49–56. doi:10.1016/S0928-4931(02)00012-7.

[255] B. Duan, L.A. Hockaday, K.H. Kang, J.T. Butcher, 3D Bioprinting of heterogeneous aortic valve conduits with alginate/gelatin hydrogels, J. Biomed. Mater. Res. - Part A. 101 A (2013) 1255–1264. doi:10.1002/jbm.a.34420.

[256] A. Lanzotti, M. Grasso, G. Staiano, M. Martorelli, The impact of process parameters on mechanical properties of parts fabricated in PLA with an open-source 3-D printer, Rapid Prototyp. J. 21 (2015) 604–617. doi:10.1108/RPJ-09-2014-0135.

[257] P. Shubham, A. Sikidar, T. Chand, The Influence of Layer Thickness on Mechanical Properties of the 3D Printed ABS Polymer by Fused Deposition Modeling, Key Eng. Mater. 706 (2016) 63–67. doi:10.4028/www.scientific.net/KEM.706.63.

[258] M. Vaezi, C.K. Chua, Effects of layer thickness and binder saturation level parameters on 3D printing process, Int. J. Adv. Manuf. Technol. 53 (2011) 275–284. doi:10.1007/s00170-010-2821-1.

[259] J. Vanek, J.A.G. Galicia, B. Benes, Clever Support: Efficient Support Structure Generation for Digital Fabrication, Comput. Graph. Forum. 33 (2014) 117–125. doi:10.1111/cgf.12437.